

# Evolution from syn-rift carbonates to early post-rift deep-marine intraslope lobes: The role of rift basin physiography on sedimentation patterns

AURÉLIA M-L. J. PRIVAT\* , DAVID M. HODGSON\* ,  
CHRISTOPHER A-L. JACKSON† , ERNESTO SCHWARZ‡  and JEFF PEAKALL\*   
\*Stratigraphy Group, School of Earth and Environment, University of Leeds, Leeds, LS29JT, UK  
(E-mail: aurelia.privat@gmail.com)

†Basins Research Group (BRG), Department of Earth Science & Engineering, Imperial College, Prince Consort Road, London, SW7 2BP, UK

‡Centre of Geological Investigation (CIG)-CONICET, National University of La Plata (UNLP), La Plata, Argentina

Associate Editor – Jim Hendry

## ABSTRACT

The stratigraphic architecture of Early Jurassic strata exposed along a >10 km long transect in the Chachil Graben, an exhumed marine rift depocentre in the Neuquén Basin (Argentina), provides insights into the sedimentological and stratigraphic expression of the syn-rift to post-rift transition. A change from syn-rift intrabasinal carbonate to post-rift extrabasinal siliciclastic sedimentation is recorded, as well as variations in sediment supply and dispersal patterns across rift-related topography. The late syn-rift was marked by a transgression and development of a shallow-marine carbonate system, including carbonate platform deposits perched on fault-block highs and periplatform deposits accumulated in fault-block lows, which overlies continental volcano-sedimentary syn-rift deposits. Differential subsidence and basin deepening induced retrogradation of the carbonate system, which was progressively drowned and overlain by organic-rich calcareous mudstone that draped across rift structures at the onset of the early post-rift. The first extrabasinal siliciclastic influx led to progradation of an early post-rift intraslope lobe complex into the graben, which is associated with kilometre-scale clastic injectites. The depositional architecture, facies distribution and pinch-out style of intraslope lobes record the effects of an inherited compaction hinge, which acted as an oblique counterslope to sediment gravity flows. The occurrence of combined-flow bedforms, widespread erosion, and limited facies segregation across lobes bearing different hybrid event bed types, is in sharp contrast to sedimentological characteristics of existing intraslope lobe models. Documentation of the syn-rift to post-rift transition stratigraphy permitted identification of changes in thickness and facies resulting from the passive infill of inherited topography with early post-rift differential compaction. This architecture contrasts markedly with those developed during syn-rift normal faulting. Furthermore, the influence of local inherited topography on the development of early post-rift lobes is key to improve subsurface prediction of sandstone distribution and quality during assessment of hydrocarbon reservoirs and carbon storage sites.

**Keywords** Early post-rift, intraslope lobe, Los Molles, Neuquén Basin, rift topography, syn-rift to post-rift transition.

## INTRODUCTION

The syn-rift to post-rift transition is associated with a change from active crustal stretching, typically accommodated by normal faulting and rapid subsidence, to slow thermally-induced subsidence associated with cooling of the crust and the cessation of normal faulting (McKenzie, 1978; Ziegler & Cloetingh, 2004). Depending on the magnitude and distribution of inherited rift topography, the location and rate of thermal subsidence, and eustatic and climatic changes, the rift may receive extrabasinal sediment almost immediately in the early post-rift phase, or this may be delayed until later in the post-rift (Ravnås & Steel, 1998; Lien, 2005; Soares *et al.*, 2012; Yu *et al.*, 2013; Jarsve *et al.*, 2014; Henstra *et al.*, 2016; Balázs *et al.*, 2017).

Detailed documentation of strata recording the syn to post-rift transition is needed to evaluate controls such as inherited rift topography, and changes in sediment source area and/or routing pathways, to improve existing conceptual models for rift basin-fills. However, the syn-rift to post-rift transition is difficult to resolve in the subsurface, due to typically low-resolution of seismic reflection data and sparse well coverage (Kyrkjebø *et al.*, 2004; Lien, 2005; Zachariah *et al.*, 2009; López-Gamundí & Barragan, 2012; Jarsve *et al.*, 2014; Lohr & Underhill, 2015). Because of this, little is known about the detailed architecture, facies distribution and development of bed-scale heterogeneity, as well as the termination style of deep-marine early post-rift lobes against inherited rift topography, all of which have been documented in the subsurface (Argent *et al.*, 2000; Martinsen *et al.*, 2005; Milton-Worsell *et al.*, 2006; Moscardelli *et al.*, 2013; Dodd *et al.*, 2019). Outcrop-based studies of ancient deep-water rift basin-fills can provide key information on sub-seismic stratigraphic architecture and facies distributions during the syn-rift to post-rift transition, but often lack detailed descriptions of early post-rift, sand-rich systems (Surlyk & Korstgård, 2013; Yu *et al.*, 2013; D'Elia *et al.*, 2015; Hadlari *et al.*, 2016).

This study investigates a rare example of an exhumed marine rift depocentre, the Chachil Graben, south-western Neuquén Basin, west-central Argentina. The aim is to document the transition from syn-rift carbonate to post-rift siliciclastic sedimentation recorded in the Chachil depocentre during the Early Jurassic. The main objectives are to: (i) analyze the tectono-

stratigraphic architecture of the depocentre-fill; (ii) provide a detailed characterization of early post-rift intraslope lobes; and (iii) discuss the impact of local and regional controls on sedimentation in order to refine the interpretation of the syn-rift to post-rift transition in the Chachil Graben and improve rift basin models. A model is presented showing the organization of sedimentary systems across the evolving rift topography, which incorporates changes in sedimentation regime, and supply and dispersal (i.e. axial, or transverse, to structural strike) during the syn-rift to post-rift transition. The influence of syn-depositional relief on the architecture, facies distribution and pinch-out style of early post-rift intraslope lobes can be used to improve hydrocarbon reservoir characterization, which can be otherwise challenging in the subsurface.

## GEOLOGICAL SETTING AND STRATIGRAPHY

The Neuquén Basin, Argentina (36°S to 40°S) formed along the south-western convergent margin of the Gondwana–South American plate, being bound by the Andean volcanic arc to the west, the Sierra Pintada belt to the north-east, and the North Patagonian Massif to the south-east (Fig. 1A). The Neuquén Basin underwent intracontinental rifting from Late Triassic to Early Jurassic, followed by subduction of the proto-Pacific plate and thermal subsidence from Early Jurassic to Early Cretaceous; foreland basin evolution with compression and inversion characterized the Late Cretaceous – Cenozoic period (Vergani *et al.*, 1995; Legarreta & Uliana, 1996; Franzese & Spalletti, 2001; Howell *et al.*, 2005).

The evolution of the south-western Gondwana margin was associated with gravitational collapse of a Late Palaeozoic orogen and widespread magmatism (Franzese & Spalletti, 2001). This led to thermo-mechanical weakening of the lower crust and lithosphere, which accommodated Late Triassic – Early Jurassic extension by opening of intracontinental volcanic rift basins (Vergani *et al.*, 1995; Legarreta & Uliana, 1996; Franzese & Spalletti, 2001). Extensional faulting with rapid mechanical and volcano-tectonic subsidence (cf. Muravchik *et al.*, 2011) controlled the accumulation of continental volcano-sedimentary successions (Precuyano Cycle; Gulisano *et al.*, 1984). These Late Triassic – Early Jurassic (Norian – Sinemurian) syn-rift continental successions include volcanic effusive, pyroclastic

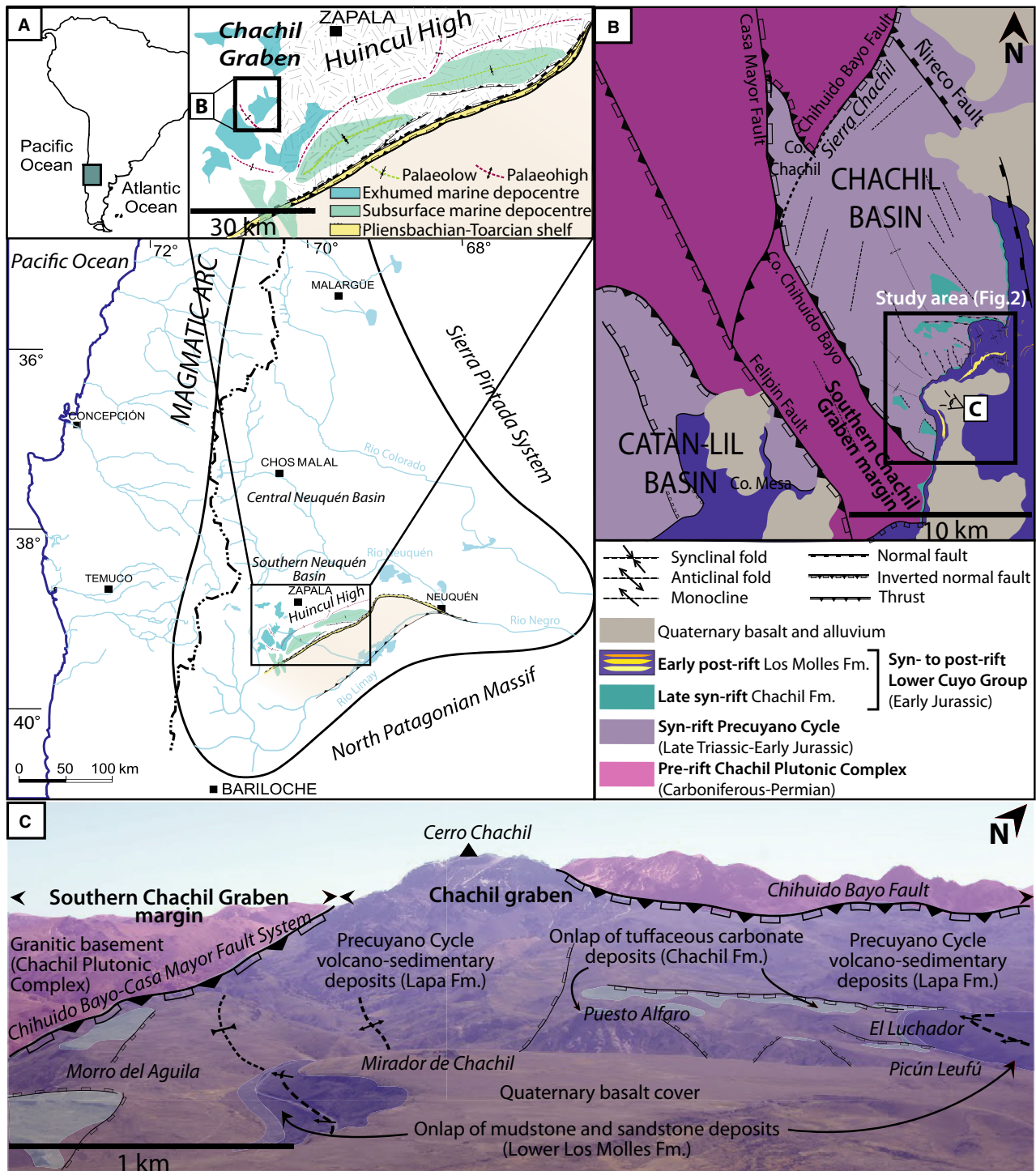


**Fig. 1.** (A) Map of the Neuquén Basin showing the location of the Chachil Graben (detailed in Fig. 1B) and the Pliensbachian–Toarcian palaeogeographic configuration, with the position of the southern shelf–slope margin of the Neuquén Basin and proximal marine depocentres (after Gómez Omil *et al.*, 2002 and García Morabito *et al.*, 2011). (B) Map of the Chachil and Catán–Lil basins (including structures after Leanza, 1990; Franzese *et al.*, 2006; Muravchik *et al.*, 2014) showing the location of Fig. 1C and detailed geological map of the study area corresponding to Fig. 2A. (C) Panorama showing a view of the Southern Chachil Graben margin and the southwest side of the graben, incorporating a number of intra-graben fault-blocks. The spatial distribution of the exposures of the Lapa, Chachil and Los Molles formations are shown (refer to the legend in Fig. 1B for the colour scheme).

and epiclastic material interbedded with alluvial–fluvial and lacustrine carbonate deposits (Franzese *et al.*, 2006; Muravchik *et al.*, 2011, 2014; D’Elia *et al.*, 2015). Isolated syn-rift depocentres are bound by major pre-rift basement fault-blocks including Late Devonian – Early Carboniferous metasedimentary rocks of the Piedra Santa Formation (Franzese, 1995), Late Carboniferous – Early Permian calc-alkaline plutons of the Chachil Plutonic Complex (Leanza, 1990) and Late Permian – Early Triassic volcanic terranes of the Choiyoi Group (Llambías *et al.*, 2003).

Transgression of volcanic rift depocentres occurred during the Early Pliensbachian along the southern margin of the Neuquén Basin, with flooding from the Panthalassic Ocean and formation of an epeiric sea along the south-western Gondwana margin (Damborenea *et al.*, 2013; Leanza *et al.*, 2013). The Early Pliensbachian also recorded the onset of subduction with trench rollback, which controlled extension and back-arc subsidence of the Neuquén Basin bounded to the west by the Early Andean volcanic island arc (Franzese & Spalletti, 2001; Mpodozis & Ramos, 2008). Initial development of Early Jurassic marine depocentres was strongly influenced by the rift topography and diachronous syn-rift to post-rift transition until the Middle Jurassic (Aalenian) (Legarreta & Uliana, 1996; Burgess *et al.*, 2000; Gómez Omil *et al.*, 2002; Veiga *et al.*, 2013). Since Middle Jurassic marine depocentres merged together into a single broad back-arc depocentre controlled by post-rift thermal subsidence (Gulisano & Gutiérrez-Pleimling, 1995; Vergani *et al.*, 1995; Legarreta & Uliana, 1996; Franzese & Spalletti, 2001). The Early to Middle Jurassic evolution of the Neuquén Basin is recorded by the Cuyo Group (Gulisano *et al.*, 1984). It comprises two second-order depositional sequences separated by the Toarcian – Aalenian boundary: the Early Jurassic Lower Cuyo Group and Middle Jurassic Upper Cuyo Group (Gulisano & Gutiérrez Pleimling, 1995; Vergani *et al.*, 1995; Legarreta & Uliana, 1996; Burgess *et al.*, 2000). This paper focuses on the Early Jurassic transgressive deposits of the Lower Cuyo Group, represented in the study area by the Chachil Formation (Weaver, 1942) and the Lower Los Molles Formation (Weaver, 1931). The aim is to document the local syn-rift to post-rift transition record in the Chachil Graben and the effects of inherited early post-rift relief on the characteristics of intraslope lobes.

## STUDY AREA AND DATA

### Chachil Graben

The study area corresponds to the Chachil Graben located in the south-western Neuquén Basin, which forms the exhumed western part of the Huincul High (Fig. 1A). The Huincul High is an ENE–WSW oriented intraplate structure characterized by a series of small NNW–SSE to NW–SE trending half-grabens and grabens inverted during the Andean compression (Vergani *et al.*, 1995; Franzese *et al.*, 2006; García Morabito *et al.*, 2011; Muravchik *et al.*, 2011, 2014). The Huincul High formed the southern shelf–slope margin of the Neuquén Basin during the Early Jurassic, where a series of marine rift depocentres (see Fig. 1A) developed with turbidite fan systems across complicated rift topography (e.g. Gómez Omil *et al.*, 2002; Pángaro *et al.*, 2009).

The Chachil Graben is a NNW–SSE trending depocentre about 10 km wide and at least 15 km long, although post-rift cover and Cenozoic volcanic rocks overlying syn-rift deposits hamper the definition of its eastern margin (Fig. 1B). Its northern margin was controlled by the Chihuido Bayo fault system, which strikes north-east/south-west and dips to the south-east. The Chihuido Bayo fault system extends for 15 km south-east from the Cerro Chachil, where it bounds the 5 km wide horst that forms the Southern Chachil Graben margin (Fig. 1B and C). The Lapa Formation, which represents the syn-rift infill of the Precuyano Cycle in the study area (Fig. 2), is <400 m thick along the Southern Chachil Graben margin and thickens up to 2 km northward in the graben centre (Franzese *et al.*, 2006). Thickness changes in the Lapa Formation were controlled by NNW–SSE and minor NE/NNE–SW/SSW striking faults, respectively parallel and oblique to the Chihuido Bayo fault system along the main Southern Chachil Graben margin (Fig. 1B). North-west/south-east and NNW–SSE striking, north-east or south-west dipping late syn-rift faults subdivide the immediate hangingwall of the Southern Chachil Graben margin into several intra-basin highs (Morro del Aguila, Puesto Alfaro, El Luchador and Paine Milla fault-blocks) and intervening lows (Mirador de Chachil and Picún Leufú fault-blocks) (Fig. 3A and B). The variability in the trend of rift faults results from the interaction of the main north-east/south-west directed extensional stress field with pre-rift Palaeozoic basement fabrics that

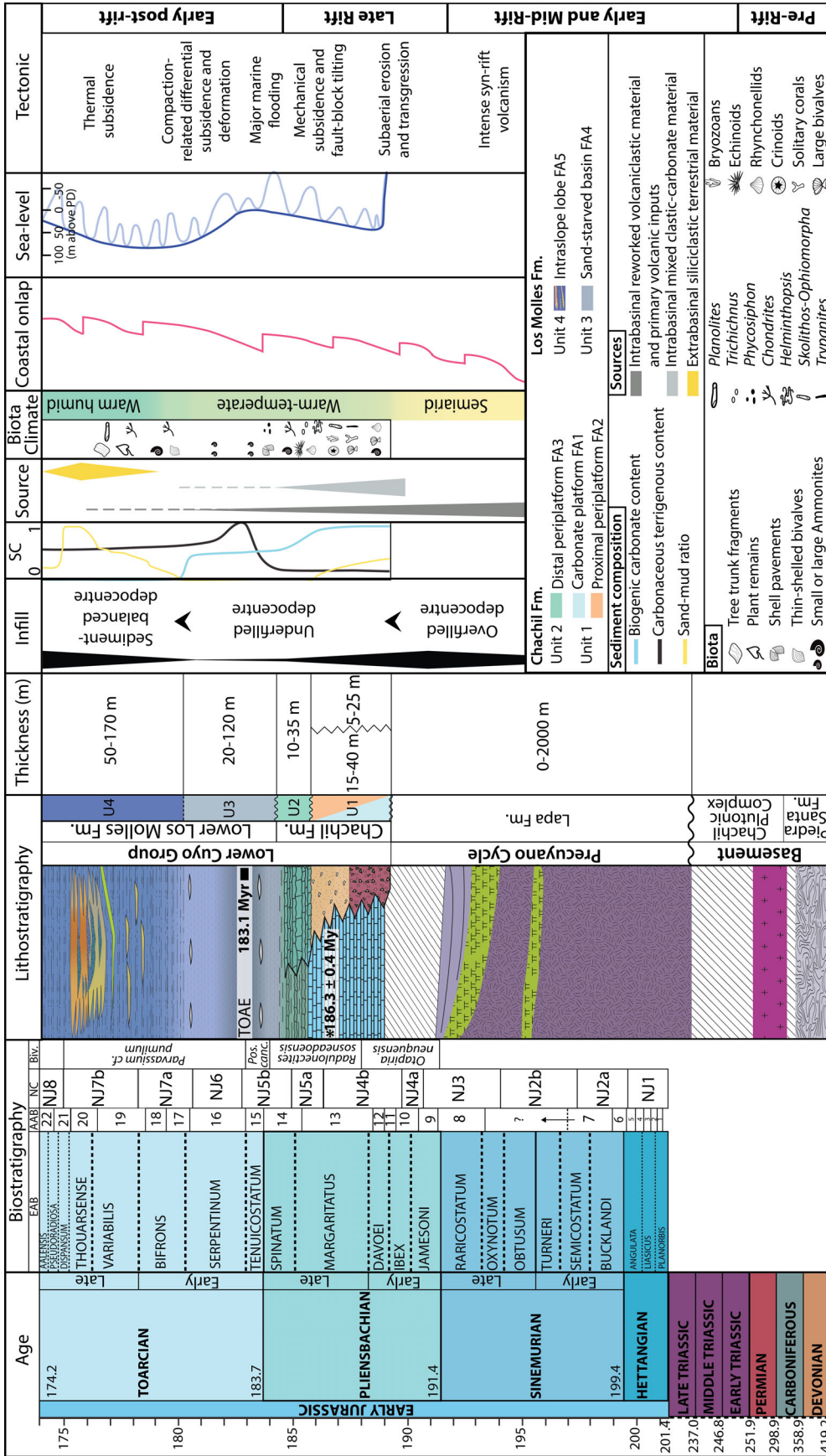
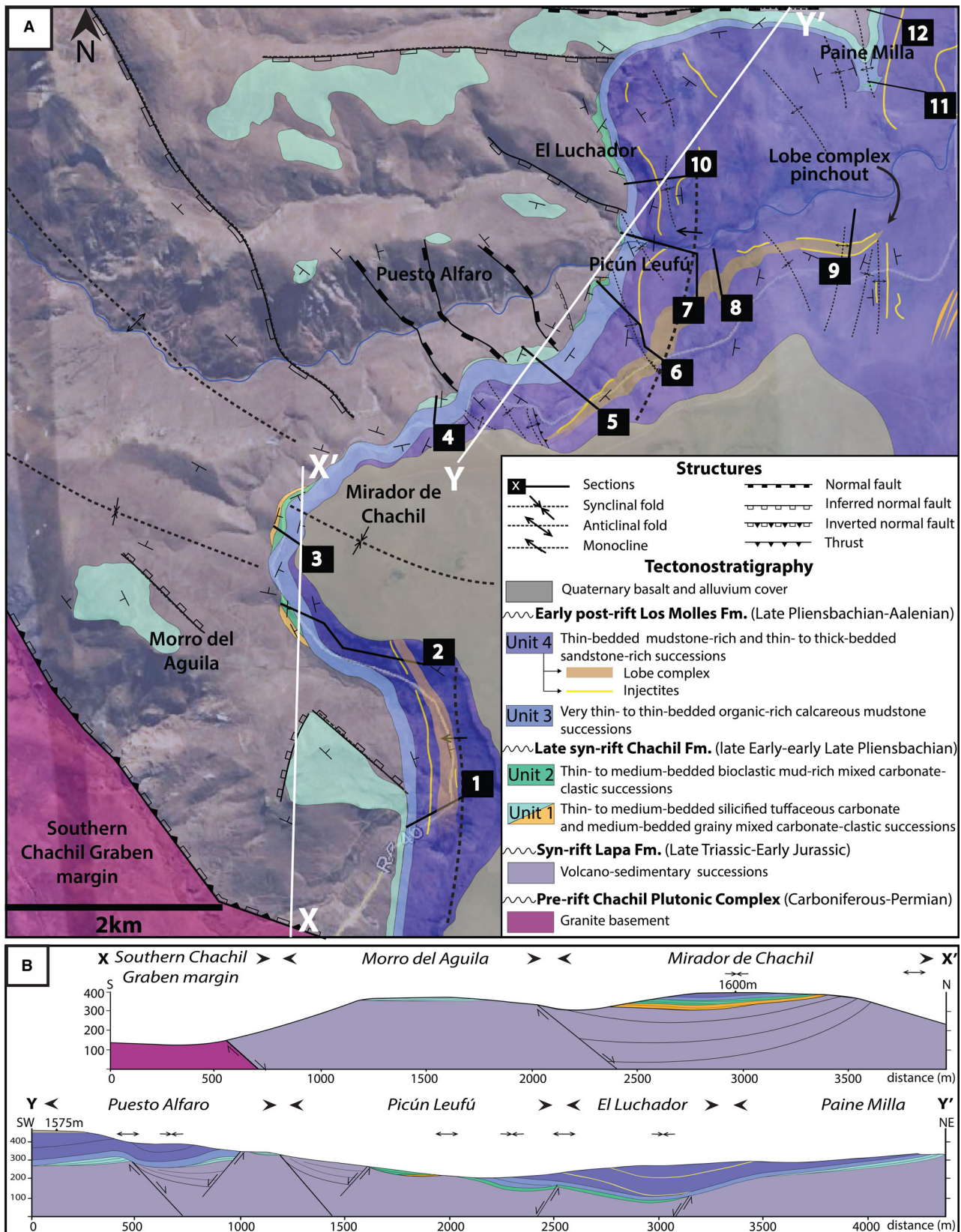


Fig. 2. Synthetic stratigraphic column for the Chachil Graben, representing thickness of lithostratigraphic units, changes in sediment composition (see heading 'SC'; note that '+' indicates an increase and '-' indicates a decrease in non-dimensionalized sediment content) and biota, source contribution and interpretations of tectonic stages. Numerical Early Jurassic ages from Ogg *et al.* (2016); (NC) nanofossil chronozones (Ballent *et al.*, 2011); Standard European Ammonite Biozone (EAB) and Andean Ammonite Biozone (AAB) numbers (Riccardi, 2008); age at base of the Chachil Formation (186.3 ± 0.4 Ma from Leanza *et al.*, 2013, modified after Armella *et al.*, 2016); negative δ<sup>13</sup>C excursion and TOAE (Toarcian Oceanic Anoxic Event) from Al-Suwaidi *et al.* (2016) in the *Tenuicostatum-Dactyloceras hoelderi* zones (AAB 15 and 16) equivalent to the *Tenuicostatum-Spinatum* EAB and constrained in NJ6 nanofossil chronozone from Angelozzi & Pérez Panera (2016); climate after Volkheimer *et al.* (2008); coastal onlap curve for the Neuquén Basin (Legarreta & Uliana, 1996); eustatic sea-level (Haq, 2018).



**Fig. 3.** (A) Detailed map of the Chachil Graben showing the stratal relationship between structures and tectono-sedimentary units of the Chachil and Los Molles formations. Note the lobe complex pinch-out indicated and broad monocline defining the base of the contact of the Lower Los Molles Formation which has been affected by numerous small-scale folds and thrusts. (B) Cross-sections (not restored) indicated on the map with location of structures and locality names. Note that the entire thickness of basement and syn-rift volcanic units is not shown.

promoted oblique rifting (Franzese & Spalletti, 2001; Mpodozis & Ramos, 2008; Cristallini *et al.*, 2009). In the study area, the later east–west Andean compressional stress field was oblique to existing rift fault trends and only resulted in partial inversion of rift structures (Pángaro *et al.*, 2006). Herein it is observed that this is expressed in the Chachil Graben with development of small-scale east/north-east dipping folds and thrusts affecting the Lower Los Molles Formation and large-scale thrusts reactivating pre-rift basement structures.

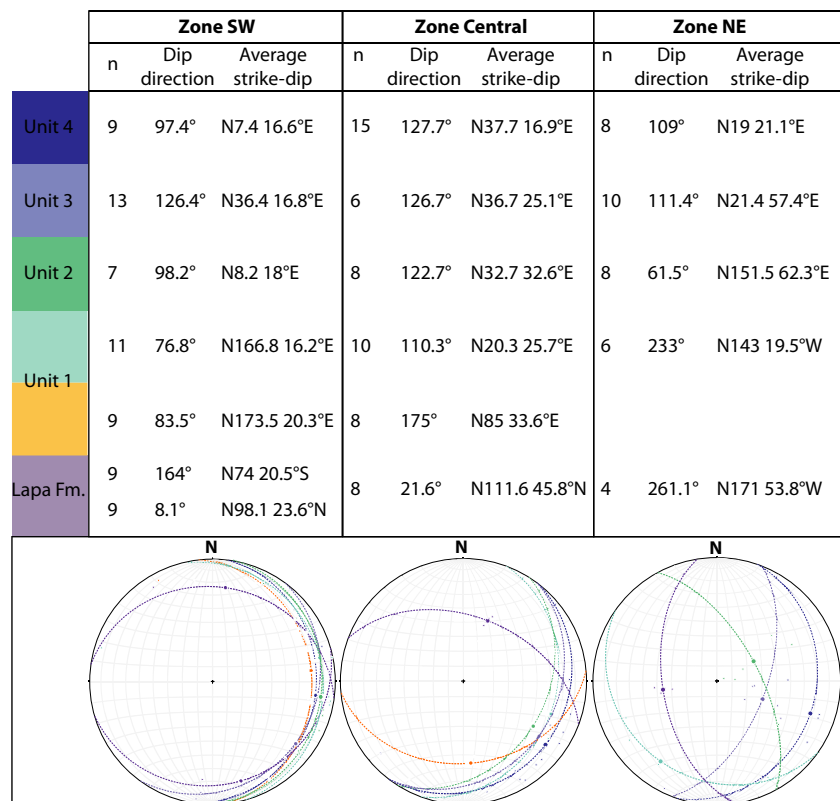
### Data and methodology

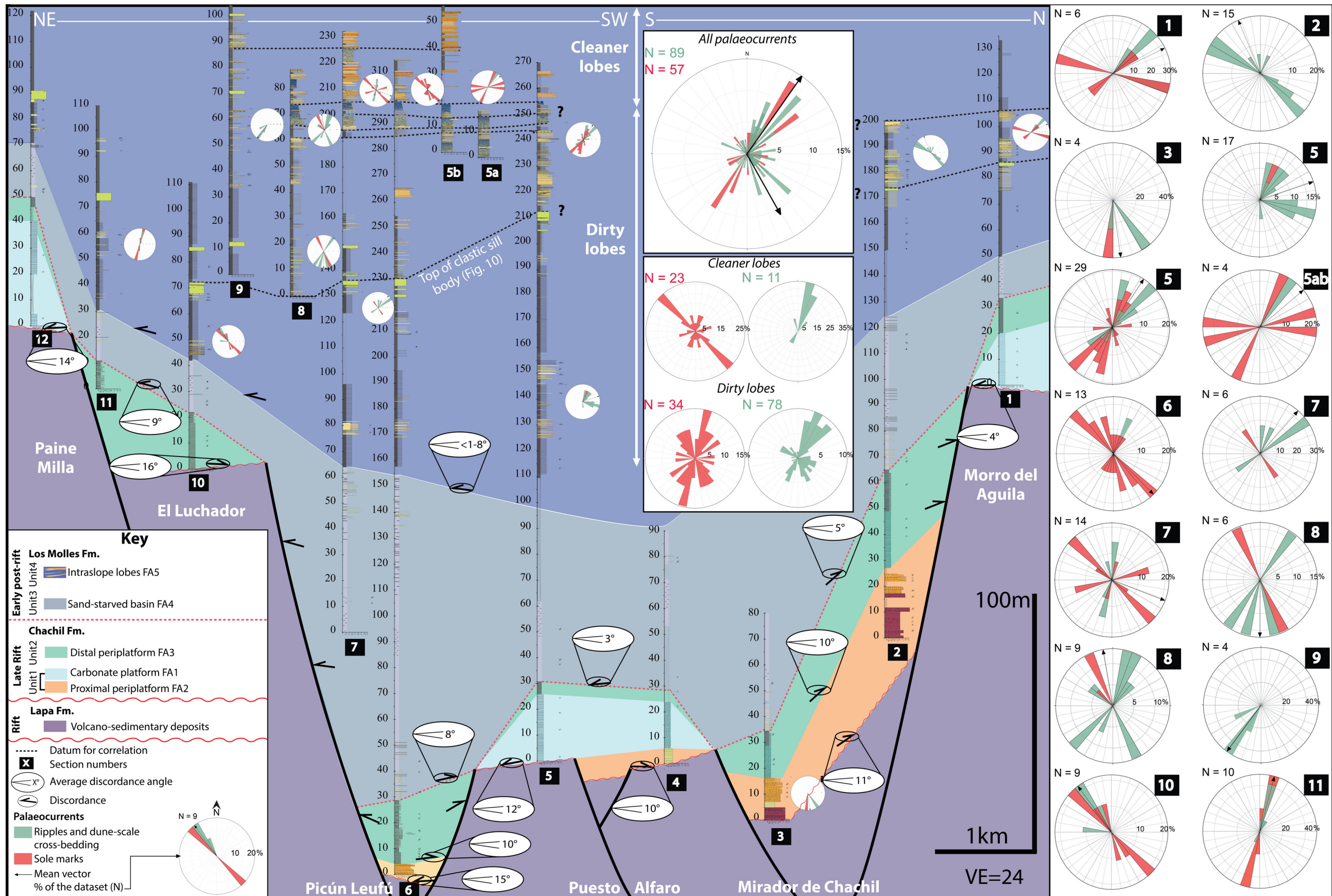
A >10 km long north-east/south-west striking exposure belt into the Chachil Graben permits the detailed analysis of sedimentology and stratigraphic architecture, with a focus on stratal

geometries, facies and thickness changes of both carbonates, and intraslope lobe systems, across rift structures. The dataset comprises detailed geological field mapping (Fig. 3) using Global Positioning System (GPS) referencing, Digital Terrain Model (DTM) and Uncrewed Aerial Vehicle (UAV) surveys, 12 logged vertical sections (1:25 scale) with regular testing of HCl reaction for carbonate rock composition, 114 strike and dip bedding readings, and 165 palaeocurrent measurements.

Bedding measurements were separated into three main geographic zones (Fig. 3A) and by tectono-sedimentary unit (Fig. 4). Present-day mean bedding orientations were calculated for each unit from all measurements taken in a given zone, to constrain an average tectonic dip, and dip direction, for each unit in each zone (Fig. 4) to help identify subtle unconformities. Overall, the overprint by later inversion on the

**Fig. 4.** Table of the average structural dip and dip direction of present-day mean bedding planes for each tectono-sedimentary unit in each zone, calculated with Stereonet software. Zone SW includes sections 1, 2, 3 and 4, Zone Central includes sections 5, 6 and 7 and Zone NE includes sections 8, 9 and 10. Stereonet diagrams show the mean strike-dip bedding values for each unit (colours in stereoplots correspond to colours of units in the table) represented as planes, along with the associated average dip direction vector (bold circle).





rift-related structures and disturbance of the depositional architecture was limited (Fig. 5). Locally, in the Zone NE, the steeper dips measured are related to structures that formed during later inversion tectonics across the El Luchador fault-block (Figs 3 and 4). Note that log sections 11 and 12 were not included in this analysis of structural dip given the paucity of data compared to other sections. Palaeocurrent measures (Fig. 5) were primarily collected from: sole marks including grooves and flute casts, ripples, and dune-scale cross-bedding, and were plotted in rose diagrams to reconstruct the palaeoflow pathways with bedding restored using stereonet software. Maps and cross-sections (Fig. 3) are based on the present-day structural and topographic configuration (i.e. no back-stripping or structural restoration). The lack of precise data including palaeobathymetric or palaeoecological proxies, volumes of eroded sediment, local eustatic curve, and flexural rigidity of the lithosphere, do not allow back-stripping to be undertaken. Furthermore, the nature of the outcrops that limit the collection of three-dimensional data, the absence of a consistent horizontal datum in all vertical sections, and the changing stress field orientation through time (Pángaro *et al.*, 2006), hinders construction of balanced cross-sections and palinspastic restoration (cf. Spikings *et al.*, 2015). Although absolute (original) depositional dips and dip azimuths cannot be determined, the use of the depositional architecture, bedding dip orientation changes, unconformities, thicknesses and palaeocurrents across rift fault-blocks, permitted the interpretation of syn-sedimentary variation in accommodation and sediment dispersal across faults, with healing of rift topography. Marker beds used for stratigraphic correlation were identified in Unit 4 (Fig. 5) and primarily consisted of extensive sandstone packages that could be walked out for several kilometres; these were deposited across a less complicated seabed topography compared to other units. The ca 5 km exhumed belt of sandstone packages

corresponding to the intraslope lobe complex represents the onlap margin of a broader sandy depocentre that continues in the subsurface to the south-east of the Chachil Graben. Physical correlation of sandstone packages and injectites between logs was also constrained with Uncrewed Aerial Vehicle (UAV) photographic panels.

## STRATIGRAPHY AND FACIES ASSOCIATIONS

Detailed sedimentological analyses allowed the identification of 25 sedimentary facies (Table 1) grouped into five different facies associations (FA). The Chachil Formation represents a carbonate system (FA1, FA2 and FA3) and the Lower Los Molles Formation represents a deep-water slope system (FA4 and FA5) including intraslope lobes for which subfacies associations have been detailed (FA5.1, FA5.2 and FA5.3) (Fig. 6).

The Chachil Formation spans the late Early–early Late Pliensbachian based on ammonites of the *Davoei* European Ammonite Biozone (EAB) (*Austromorphites behrendseni* of Andean Ammonite Biozone; AAB number 12) (Riccardi, 2008), bivalve species of the *Radulonectites sosneadoensis* Assemblage Zone (Riccardi *et al.*, 2011) and a U-Pb weighted average age of  $186.3 \pm 0.4$  Ma (Leanza *et al.*, 2013; Armella *et al.*, 2016) (Fig. 2). The presence of *Posidonotis cancellata* (Leanza) in the lower part of Unit 3 (described below) indicates onset of deposition of the Lower Los Molles Formation prior to the latest Pliensbachian, based on the extent of the *Posidonotis cancellata* Assemblage Zone spanning the latest *Spinatum* and *Tenuicostatum* EAB (Fig. 2) (cf. Riccardi *et al.*, 2011).

### Facies Association 1: Carbonate platform

#### Description

Facies Association 1 (FA1) consists of well-stratified, thin to medium-bedded silicified carbonate

---

**Fig. 5.** Correlation panel (ca 10 km long transect indicated in Fig. 3A), showing relationships between units in the Chachil Graben, along with average discordance angles corresponding to the location of the logs (see Fig. 4) and palaeocurrent measurements. Each rose diagram shows the detail of sole marks (in red), and ripples and dune-scale cross-bedding current directions (in green). Marker beds used for correlation are shown with dashed black lines, and correspond to depositional sandstones and debrites (for specifics see the detailed architecture of intraslope lobes in Fig. 9), and the top of the clastic sill body (see Fig. 10). Note that there is uncertainty in lobe correlation between logs 1 and 2, and logs 5 to 9, due to basalt cover (see map Fig. 3A). The detailed architecture of the Lapa Formation is not represented and vertical offsets on faults are approximate. Orientation of sections is shown on the map in Fig. 3A.

**Table 1.** Descriptive facies table providing interpretation for depositional processes. Note abbreviations: Cobble (Co), Pebble (Pb), Granule (Gr), Very coarse (VCs) Coarse (Cs) Medium (Ms) Fine (Fs) very fine (VFs) sandstone, Silt (Si), Mudstone (Mds), Very poorly sorted (VPS), Poorly sorted (PS), Moderately sorted (MS). Volcanics (vg), quartz (qtz), K-feldspar (K-Fd), fairweather-wave base (FWWB) and storm-wave base (SWB).

Facies	Description	Bed thickness/ Boundaries	Processes
F1a Micritic tuffaceous carbonate	Wackestone with wispy undulated tuffaceous laminations (0.5–1.0 cm thick), semi-infaunal and epifaunal articulated large thick-walled bivalve shells in life position or disarticulated, crinoid ossicles and articulated stems, few siliceous sponge spicules alternating with tuffs (1–10 cm).	(10–35 cm) Tabular, crenulated sharp base and top with <i>Trypanites</i> .	<i>In situ</i> biogenic carbonate precipitation and accumulation of biotrital mud at seabed with gentle wave-induced reworking, and frequent ash-falls. Deposited in a low-energy well-oxygenated subtidal environment near the FWWB close to photic depths (<30–50 m)
F1b Fossiliferous carbonate	Packstone massive or with rare sub-parallel undulose laminations (up to 2 cm thick), disarticulated bivalve shells, reworked volcanoclastic Cs grains (quartz, K-Fd) (2 mm) scattered throughout beds and sponge spicules.	(50–70 cm) Tabular, wavy sharp base and top, locally with <i>Helminthopsis</i> .	(Damborenea & Manceño, 1979, 1992; Armella et al., 2016).
F2a Pebbly conglomerate	VPS weakly graded to ungraded VCs-Cs to Ms sandy matrix-supported polygenic conglomerate (lack mud) with angular to subrounded clasts (reworked vg, quartz, Mds) (0.5–25 cm), pieces of wood (15 cm), disarticulated shells (bivalves, rhynchonellids), crinoid ossicles. Locally clast-supported base.	(20–90 cm) Tabular, low erosional relief at base (<10 cm deep) and sharp planar top.	Non-cohesive hyperconcentrated density flows rich in reworked volcanoclastic material (Mulder & Alexander, 2001; Drzewiecki & Simó, 2002; Payros & Pujalte, 2008).
F2b Calciturbidite	MS crudely normally or inversely graded bioclastic Cs-Ms to Fs locally low-angle cross-laminated, bearing subrounded Pb (1.5 cm) clasts (reworked vg, quartz, K-Fd), bioclasts (thick-walled fragmented shells, crinoid ossicles, fragments of solitary coral ( <i>Montivaltia</i> ) and bryozoans).	(50–70 cm) Lenticular to lens-shaped, erosional base (up to 15 cm deep) and sharp planar top or amalgamated.	High-density turbidity currents rich in reworked bioclastic material (Braga et al., 2001; Payros & Pujalte, 2008) accumulated in a moderate-energy well-oxygenated environment near the FWWB.
F2c Calcarenite	Grainstone, massive, dominated by well-rounded Ms to Fs sized allochems and quartz grains and thin shells (bivalves).	(30–50 cm) Tabular, with subplanar sharp planar base and top with <i>Skolithos</i> and <i>Ophiomorpha</i> .	Concentrated bioclastic grain flows (Drzewiecki & Simó, 2002; Halfar et al., 2004) accumulated in a moderate-energy well-oxygenated near the FWWB.

Table 1. (continued)

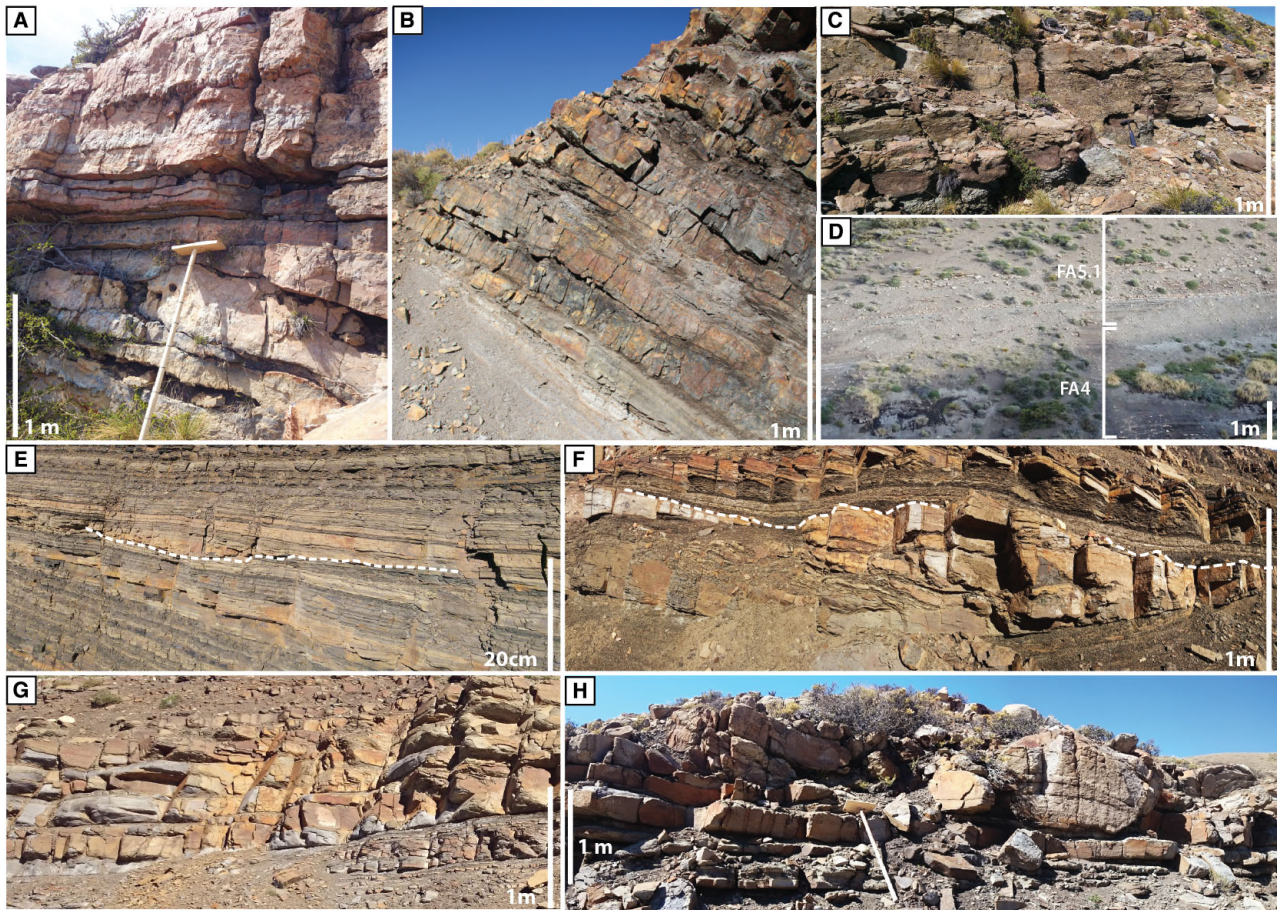
Facies	Description	Bed thickness/ Boundaries	Processes
F3a Bioclastic cb	Packstone with reworked volcanoclastic Ms-Fs grains (K-Fd), disarticulated small shells (bivalve, brachiopod) and undulose, laminated, normally graded grain-rich layers (1–2 cm).	(15–50 cm) Tabular or locally trough-cross bedded, irregular undulated sharp base and top, with <i>Cylindrichnus</i> .	High-energy storm-wave-reworked with transport of allochemical shelly bioclastic and biotrital carbonate material in a well-oxygenated environment near the SWB (i.e. distal tempestite Pérez-López & Pérez-Valera, 2012).
F3b Spiculitic cb	Wackestone with monaxon and tetraaxon siliceous sponge spicules, reworked volcanoclastic Ms-Fs grains (quartz, K-Fd), pumice (1–2 mm), micritic intraclasts (2–5 cm) and alternating with marlstone and tuffs (5–10 cm).	(30–50 cm) Tabular or lens-shape, sharp base and top with <i>Chondrites bollensis</i> and <i>Trichichnus</i> .	Low-energy storm-wave winnowing of parautochthonous mixed spiculitic bioclastic and biotrital carbonate material with frequent ash-fall, in a moderately-oxygenated environment below the SWB (i.e. storm-winnowed beds, Pérez-López & Pérez-Valera, 2012).
F3c Marlstone	Marlstone laminated with sponge spicules, tuffaceous and broken shell-hash layers (<0.5 cm), and few large ammonites (15 cm).	(10–60 cm) Flat base and top.	Post-storm settling of winnowed micritic biotrital carbonate material and shell hash with frequent ash-fall below the SWB (D'Atri <i>et al.</i> , 1999; Halfar <i>et al.</i> , 2004).
F4a Calcareous mudstone	Organic-rich calcareous Mds (pelagic and allochemical biotrital carbonate silt and clay), massive to faintly laminated, alternating with tuffs (1–5 cm), bearing large carbonate strata-bound concretions (15 cm) and pyrite concretions (5–8 cm), juvenile bivalve shell pavements including <i>Posidonotis cancellata</i> (Leanza), small ammonites (2–5 cm).	(5–20 cm) Diffuse or sharp base and top.	Pelagic settling with frequent clastic dilution by storm-derived low-density biotrital carbonate mud plumes and ash-fall, in a low-energy and poorly-oxygenated environment (Schieber, 2016; Birgenheier & Moore, 2018) below the SWB (50–100 m up to 200–400 m depth).
F4b Calcareous mud-rich siltstone	Si massive to normally graded.	(5–40 cm) Sharp bases and tops with <i>Phycosiphon</i> and <i>Chondrites intricatus</i> .	Storm-induced bioclastic-rich low-density turbidity currents waning with traction-plus-fallout (Bouma, 1962; Lowe, 1982).
F4c Calcareous bioclastic sandstone	MS normally graded Ms to Fs with low angle planar and current-ripple laminations and with abundant broken skeletal material.	(15–40 cm) Sharp planar or erosional bases and sharp tops.	Storm-induced bioclastic-rich intermediate high to low-density turbidity currents waning with traction-plus-fallout (Bouma, 1962; Lowe, 1982).
F5.1a Massive to subtly graded mudstone	Fissile Mds massive to subtly graded bearing plant nodules (10 cm), tiny bivalve moulds and ammonites (5–10 cm).	(1–20 cm) Sharp bases and subtle gradational tops with <i>Chondrites</i> .	Suspension fallout from fine-grained waning dilute turbidity currents (Stow & Bowen, 1980) in a poorly to moderately-oxygenated environment.

Table 1. (continued)

Facies	Description	Bed thickness/ Boundaries	Processes
F5.1b Pin-striped laminated mudstone	Mds with parallel to low-angle planar discontinuous laminations of Fs and Si bearing Mds (<0.2–2.0 cm).	(1–20 cm) Sharp bases and tops.	Clay-laden, turbulence-enhanced flows to lower transitional plug flows ( <i>sensu</i> Baas et al., 2009) rapidly decelerating (cf. 'streaky bedding' of Baas et al., 2016).
F5.1c Graded sandy siltstone	Normally graded sandy Si with sandy low-angle laminations and starved current-ripples.	(5–20 cm) Sharp bases and gradational tops.	Traction-plus-fallout from low-density turbidity currents (Lowe, 1982; Best & Bridge, 1992).
F5.1d Structured fine- grained sandstone	MS crudely to normally graded Ms to VFs with planar or undulose laminations and current-ripples, locally carbonaceous-rich.	(5–20 cm) Sharp or erosional bases (scour-like features) and sharp or gradational tops with <i>Chondrites</i> and <i>Planolites</i> .	Traction-plus-fallout from low-density turbidity currents (Lowe, 1982; Best & Bridge, 1992) in a poorly to moderately-oxygenated environment.
F5.1e Injected sandstone	Massive Ms or Fs well-cemented, bearing angular Mds clasts (2–5 cm) and angular heterolithic rafts (10–50 cm) parallel to bedding, with zones of calcite-filled sub-spherical vugs (0.2–1.0 cm) near bed top.	(0.3 m – >3.8 m) Stepped sharp bases and sharp tops with linear wave-crest structures (up to >1 m long) that cross-cut mudstone.	Clastic injection of small dykes and large sills (Hurst et al., 2011).
F5.2a Massive mud- poor sandstone	PS Cs-Ms with clay-poor matrix, massive or with subtle normal grading and bearing few deformed subrounded to subangular Mds clasts (0.5–8.0 cm) near base or throughout. Mud-rich bed-waves (decimetre-scale) with low-angle laminae (5–10 cm high and wavelength few dm) can be present near top.	(5–80 cm) Planar or irregular erosional bases (grooves) and pinch and swell bed with wavy tops locally scoured.	Lower to upper transitional plug flows ( <i>sensu</i> Baas et al., 2009) slowly decelerated with local propagation of low-amplitude bed-waves (Baas et al., 2016; Baker & Baas, 2020). Grooves indicate a phase with significant cohesive strength (Peakall et al., 2020).
F5.2b Banded muddy sandstone	PS Fs with clayey banding (1–5 mm to 2 cm) alternating planar sub-parallel to undulose light mud-poor and dark mud-rich bands bearing platy mudchips or Mds clasts (2–5 cm) at base. Banded bedforms can develop as mud-rich low-angle draping laminations associated with symmetrical hummocks (15–30 cm high and wavelength ca 0.5 m) and mud-rich asymmetrical ripples (10–20 cm high and wavelength few decimetres) with high-angle foresets (>15°).	(0.05–0.4 m) Planar or undulated loaded bases (flames) and sharp to gradational tops.	Lower to upper transitional plug flows rapidly decelerated when development of bands ( <i>sensu</i> Baas et al., 2009) or turbulence-enhanced to lower transitional plug flows moderately decelerated when development of heterolithic tractional bedforms (Baas et al., 2016; Stevenson et al., 2020).
F5.2c Clast-rich muddy sandstone	PS Ms with patchy mud-rich matrix bearing outsized Cs grains and sheared/deformed Pb Mds clasts (2–25 cm) with mudchip rims throughout bed.	(20–60 cm) Sharp or erosional and/or sheared bases, and irregular or pinch and swell bed with wavy tops.	Transient low to intermediate yield strength sandy debris-flows (Talling et al., 2012).

Table 1. (continued)

Facies	Description	Bed thickness/ Boundaries	Processes
F5.2d Massive silty mudstone	Homogeneous massive to slightly graded silty Mds.	(10–60 cm) Gradational contact or sharp bases, tops locally draping scour bedform troughs.	Collapse of depletive fluid mud flows (Baas <i>et al.</i> , 2011).
F5.2e Chaotic muddy sandstone	VPS patchy muddy Ms-Fs matrix with outsized subangular Gr/Cs lithics, abundant mudchips, deformed sand-streaks, Pb to Co clasts (Mds, Ms) (5–30 cm), heterolithic rafts (80 cm) in the lower sandier part of bed and clast-poor and mud-rich top.	(4–6 m) Erosional bases scouring into underlying substrate and irregular mounded tops.	Intermediate yield strength sandy debris-flows (Talling, 2013).
F5.2f Chaotic sandy mudstone	VPS well-mixed sand-rich mudstone matrix with outsized Cs grains (starry-night like), plant material and subrounded Pb clasts (Mds, Si, Ms with pectens and ostreid shells) (5–50 cm) floating in the muddier upper part of beds.	(0.8–5.0 m) Erosional or sharp bases and sharp flat tops.	High yield strength cohesive muddy debris flows (Talling, 2013).
F5.3a Massive to crudely stratified sandstone	PS crudely graded Cs-Ms locally with diffuse planar parallel laminations (1–3 cm) and subrounded elongated Gr-Pb clasts (Mds) (1–6 cm).	(0.5–1.2 m) Erosional (grooves) or sharp or loaded bases, and sharp tops or amalgamated. <i>Planolites</i> and <i>Chondrites</i> .	High-density flows with high sediment fallout and suppressed traction (Kneller & Branney, 1995) in a moderately to well-oxygenated environment. Grooves indicate a phase with significant cohesive strength (Peakall <i>et al.</i> , 2020).
F5.3b Granular sandstone	VPS massive crudely graded VCs-Cs to Ms bearing subangular Gr to Pb clasts (0.2–8.0 cm) (Mds, Si) with local coarse-tail normal or inverse grading, armoured clasts with bioclasts (bivalve shells, belemnites, foraminifera).	(5–90 cm) Erosional bases and sharp tops or amalgamated. Local cross-bedding.	High-density to hyperconcentrated density flows (Lowe, 1982; Mulder & Alexander, 2001).
F5.3c Graded structured medium sandstone	MS normally graded Cs to Ms structured with asymmetrical swaley and hummock-like low-angle and trough-cross-laminations associated with hummock-like bedforms (10–25 cm high and wavelengths of few decimetres) or decimetre-scale asymmetrical rounded ripples with low-angle foresets (<5°) draped by sinusoidal parallel laminae.	(5–30 cm) Sharp planar bases and wavy tops.	Traction-plus-fallout from high-density flows and bedform aggradation in the upper-stage plane bed field with dominant unidirectional or oscillatory combined flow component (Tinterri, 2011).



**Fig. 6.** Representative photographs of facies associations. (A) Facies Association 1 (FA1): Thin to medium-bedded silicified carbonate platform successions. (B) Facies Association 3 (FA3): Thin to medium-bedded mud-rich mixed carbonate-clastic successions of distal periplatform. (C) Facies Association 2 (FA2): Medium-bedded mixed carbonate-clastic successions of proximal periplatform. (D) Transition from FA4 to FA5.1. Facies Association 4 (FA4): Very thin to thin-bedded calcareous mudstone-dominated successions of sand-starved basin. Note the transition in colour from dark grey mudstone (FA4) to brownish silty mudstone and sandstone (FA5.1). (E) Facies Association 5.1 (FA5.1): Thin-bedded muddy heterolithic successions of distal lobe fringe, with thin sandstone beds (F5.1d) that can locally have scoured bases (dotted line). (F) Facies Association 5.2 (FA5.2): Thin to medium-bedded sandy heterolithic successions of lobe fringe which also comprise thicker and coarser-grained sandstone and debrite beds that form HEBs. Note mud-filled pinch and swell topography (dotted line) at top of massive clast-rich muddy sandstone (F5.2c). (G) Facies Association 5.2 (FA5.3): Medium to thick-bedded sandstone-dominated successions of dirty lobe axis (F5.3a and F5.2b at top). (H) Facies Association 5.3 (FA5.3): Medium to thick-bedded sandstone-dominated successions of cleaner lobe axis (F5.3b and F5.3c at top).

successions (thickness range of individual successions 10 to 40 m) (Fig. 6A) including laterally extensive thin tuff layers (1 to 10 cm thick). FA1 onlaps onto volcano-sedimentary syn-rift deposits (Lapa Formation) of fault-block highs and passes laterally into FA2 in fault-block lows (Figs 5 and 7). Thin to medium beds (10 to 35 cm thick) of micritic tuffaceous carbonate (F1a) have a wackestone texture and wispy, undulose tuffaceous laminations (0.5 to 1.0 cm thick). The faunal content in FA1 is dominated

by semi-infaunal and epifaunal bivalves (*Kolymonectes weaveri* (Damborenea), *Radulonectites sosneadoensis* (Weaver), *Agerchlamys wunschae* (Marwick), *Weyla bodenbenderi* (Behrendsen), *Weyla alata angustecostata* (R. Philippi), *Chlamys textoria* (Schlotheim), *Antiquilima*, *Plicatula rapa* (Bayle and Coquand), *Entolium* and *Pinna* sp.) (see Leanza, 1990). Large bivalve shells (5 to 10 cm diameter) are either articulated and in life position or slightly disarticulated. Shells are associated with well-preserved

circular crinoid ossicles (3 to 5 mm diameter) or articulated stems (2 cm long) often found in tuffaceous-rich levels, whereas rare siliceous sponge spicules are concentrated in micritic-rich levels. Strata are tabular with irregular, crenulated sharp bases and tops with some vertical borings (*Trypanites*). Stylolites, which can be bed-parallel or sub-parallel are also present, outlined by dark greyish insoluble material. Medium beds (50 to 70 cm thick) of fossiliferous carbonate (F1b) have a packstone texture that is massive or with rare undulose sub-parallel laminations (0.4 to 2.0 cm thick). Disarticulated bivalve shells in broken fragments (5 cm long) and very coarse sand-sized reworked volcanoclastic grains (quartz and K-feldspar) are scattered throughout beds; the bulk of the bed is composed of a fine-grained sand-sized fraction of this bioclastic and volcanoclastic material (Fig. 8A). Beds are tabular with wavy sharp bases and tops, locally showing Pascichnia grazing traces (*Helminthopsis*) at the contact with the overlying marlstone (F3c) of FA3.

#### Interpretation

In the micritic tuffaceous carbonate facies (F1a), the preservation of bivalves in life position or weakly disarticulated indicates no or very little post-mortem transport. This indicates *in situ* deposition under stable low hydraulic conditions consistent with the small diameter of articulated crinoid stems. The abundance and species of large-sized bivalves indicate deposition in a well-oxygenated and low-energy shallow environment (cf. Damborenea & Manceñido, 1979, 1992). The *in situ* suspension-feeder organisms and carbonate-secreting benthos, including encrusters and shelly biocalcifiers (see also FA2), point to a warm-temperate carbonate factory (cf. Betzler *et al.*, 1997; Flügel, 2004). The lack of early cementation and binding of these deposits favoured their reworking and resedimentation as allochemical biodepositional carbonate material (e.g. Halfar *et al.*, 2004). Resedimented volcanoclastic grains together with parautochthonous broken or disarticulated shells in fossiliferous carbonate (F1b) suggest intermittent wave-induced physical reworking with limited transport, in an otherwise calm environment. This facies association is interpreted to represent warm-temperate carbonate platform deposits in a low-energy and well-oxygenated shallow environment below or near the fairweather-wave base, influenced by episodic ash-falls

(e.g. Armella *et al.*, 2016). Biodepositional carbonate mud accumulated *in situ* with skeletal accretion, bioerosion and weak mechanical reworking of organisms that formed a micritic substrate on fault-block highs, which remained near photic depths (<30 to 50 m) in normal marine waters. Primary volcanic material mixed with carbonate deposits indicates simultaneous explosive volcanic eruptions from the western magmatic arc which is postulated to have intermittently restricted the photic zone and depleted the biota (Armella *et al.*, 2016).

#### Facies Association 2: Proximal periplatform

##### Description

Facies Association 2 (FA2) forms weakly stratified, medium-bedded mixed carbonate-clastic successions (5 to 28 m thick) (Fig. 6C) restricted to fault-block lows that onlap onto volcano-sedimentary syn-rift deposits (Lapa Formation). FA2 in fault-block lows is the lateral equivalent to FA1 on fault-block highs (Figs 5 and 7). FA2 includes: (i) polygenic pebbly conglomerate (F2a); (ii) normally graded coarse to fine-grained calcareous sandstone (F2b); and (iii) massive calcarenite (F2c). Pebbly conglomerate (F2a) forms medium to thick beds (20 to 90 cm thick), with a very poorly sorted, very coarse to medium-grained, weakly to non-graded, sandy matrix. They (F2a) bear abundant polymict granule to gravel-sized (0.5 to 25 cm long) and angular to subrounded clasts (reworked pyroclastic and effusive volcanics, quartz and mudstone). Pebbly conglomerate deposits (F2a) also bear a few pieces of wood (up to 15 cm), disarticulated small bivalve and rhynchonellid shells (2 to 5 cm long), and pentagonal or circular crinoid ossicles (5 mm diameter). Individual beds are massive and tabular with low erosional relief at their bases (<10 cm deep), are locally clast-supported, and have sharp planar tops. Medium to thick beds (50 to 70 cm thick) of moderately sorted, planar or cross-laminated, crudely normally or inversely graded calcareous sandstone (F2b) are formed of bioclasts, reworked coarse sand-sized volcanoclastic grains (quartz, K-feldspar) and subrounded clasts (1.5 cm long) from a volcanoclastic protolith. Bioclasts include thick-walled fragmented mollusc shells (2 to 5 cm long), crinoid ossicles (5 mm diameter), fragments of discoidal robust solitary coral (<5 cm diameter) (*Montlivaltia*, see Gulisano & Gutiérrez Pleimling, 1995) and bryozoans (3 cm diameter) (Fig. 8B). Beds can show low-angle

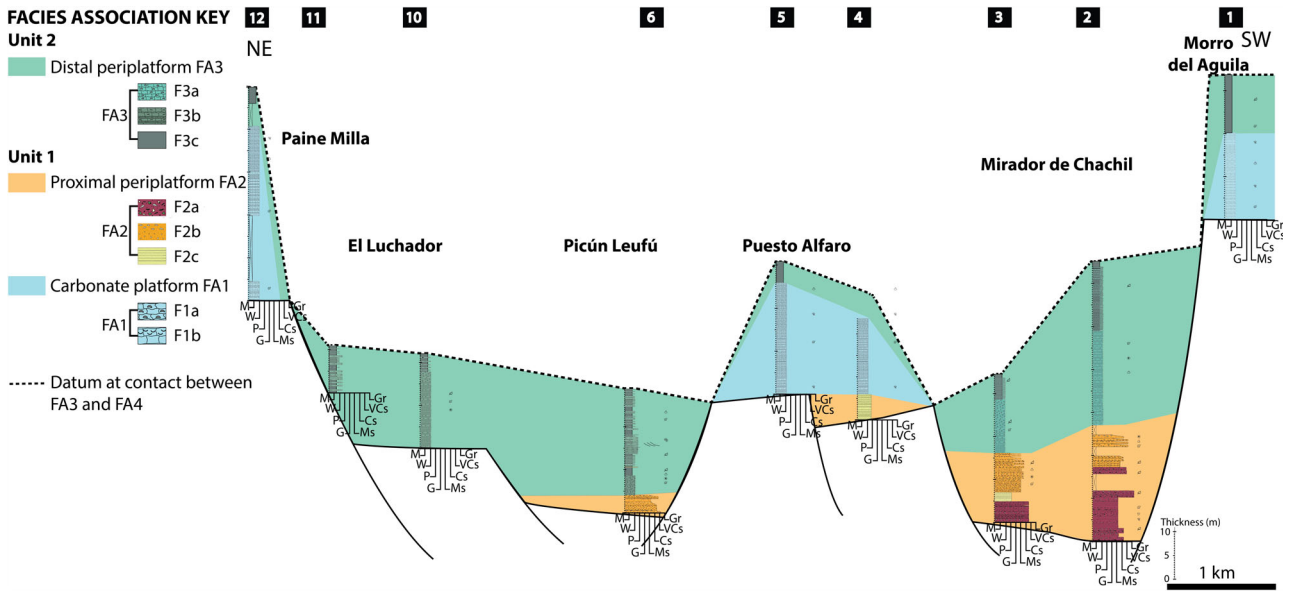


**Fig. 7.** Detailed correlation panel showing the relationships between Unit 1 and Unit 2 (Chachil Formation) and the large-scale distribution of facies (section numbers are shown at top, see Figs 3 and 5 for the location of sections). Note that the datum is defined by the contact between Unit 2 and Unit 3 which corresponds to a facies change from F3b light grey laminated spiculitic marlstone (FA3) to F4a dark grey organic-rich calcareous mudstone with concretions and bivalve shell pavements (FA4). Facies are detailed in Table 1.

cross-laminations and may form isolated lenses, have a broad lenticular to lens-shape (<8 m wide) with erosional bases (up to 15 cm deep) and sharp planar tops, or are locally amalgamated. Medium beds (30 to 50 cm thick) of well-sorted, massive, calcarenite (F2c) have a grainstone texture, with well-rounded, medium to fine-grained skeletal and quartz grains and thin-shelled bivalves (1 to 2 cm long). Beds have sharp planar bases and tops, which locally are penetrated by vertical burrows (*Skolithos* and *Ophiomorpha*).

#### Interpretation

The pebbly conglomerate deposits (F2a) are characterized by a very poor sorting of immature reworked volcanoclastic clasts admixed with bioclasts, which indicate a weak gravitational sorting and reworking across a short transport distance prior to deposition. The dearth of mud matrix, local segregation of clasts at the base of beds, little to no grading and lack of stratification in these deposits suggest emplacement by subaqueous non-cohesive hyperconcentrated density flows (Mulder & Alexander, 2001; Drzewiecki & Simó, 2002; Payros & Pujalte, 2008). Calciturbidites (F2b) contain a high proportion of fragmented bioclasts relative to reworked

volcanoclastic material, with local normal or inverse grading and traction structures that indicate transport and deposition by high-density turbidity currents (Braga *et al.*, 2001; Payros & Pujalte, 2008). Calcarenites (F2c) lack mud matrix, grading or structures and reflect intense bioclastic grain reworking and rounding prior to deposition by concentrated bioclastic grain flows (Drzewiecki & Simó, 2002; Halfar *et al.*, 2004). Given the composition and diversity of the bioclastic material in this facies association, it may have been sourced from erosion and reworking of sediment accumulated in the carbonate platform (FA1). Collectively, the grainy facies of FA2, which results from mechanical reworking of bioclastic and volcanoclastic material, formed platform-derived calciclastic aprons detached from the carbonate platform (FA1) across rift topography. Therefore, FA2 is interpreted to represent proximal periplatform deposits accumulated below the fairweather-wave base, in a deeper environment than FA1. The dearth of carbonate mud within FA2 suggests resuspension and elutriation of the biodeutral carbonate mud fraction of FA1, prior to deposition of the coarser-grained components. FA2 and the finer-grained mud-rich FA3 do not interdigitate, rather FA3 overlies FA2, suggesting that during

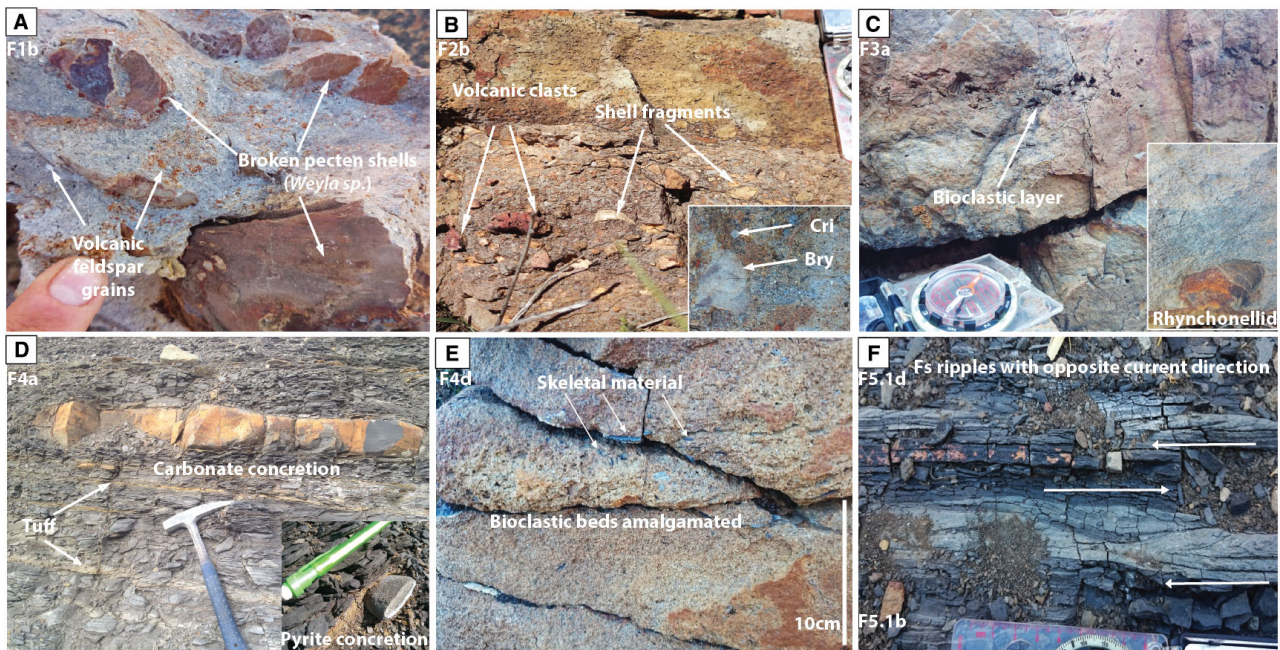


**Fig. 8.** Representative photographs of facies. (A) Fossiliferous packstone (F1b) bearing reworked volcanoclastic coarse sand-sized grains (K-feldspar) and abundant large broken bivalve shell fragments scattered throughout beds. (B) Calciturbidites (F2b) characterized by their crude normal grading and a high proportion of bioclasts (crinoids (Cri), bryozoans (Bry), thick-walled disarticulated shells, with a few reworked volcanoclastic subrounded pebbles. (C) Bioclastic packstone (F3a) with reworked volcanoclastic fine to medium sand-sized grains (quartz and K-feldspar) and small disarticulated to broken shells of bivalve and brachiopod concentrated in wavy normally graded grain-rich layers. (D) Massive calcareous mudstone (F4a) bearing thin tuff layers, early diagenetic carbonate and pyrite concretions. (E) Calcareous bioclastic sandstone (F4c) normally graded with bioclastic base. (F) Silty mudstone (F5.1a) and pin-striped laminated mudstone (F5.1b) interbedded with sandy siltstone current-ripples (F5.1c) locally presenting opposing palaeocurrent directions.

deposition of FA2 there was efficient bypass of the resuspended mud fraction to deeper parts of the carbonate system (cf. Pérez-López & Pérez-Valera, 2012) represented by FA3.

### Facies Association 3: Distal periplatform

#### Description

Facies Association 3 (FA3) corresponds to poorly stratified, medium to thin-bedded mud-rich mixed carbonate–clastic successions (thickness range of individual successions 10 to 35 m thick) (Fig. 6B) including laterally extensive tuff layers (5 to 10 cm). FA3 unconformably overlies FA2, thickening towards fault-block lows and thinning on fault-block highs where it overlies FA1 (Fig. 7). Thin to medium beds (15 to 50 cm thick) of bioclastic carbonate (F3a) have packstone texture, with fine to medium sand-sized reworked volcanoclastic grains (quartz and K-feldspar) from a volcanoclastic protolith, and small disarticulated shells of bivalves and

brachiopods. Broken shells can be concentrated in undulose laminated normally graded grain-rich layers (1 to 2 cm thick) (Fig. 8C). Individual beds have a tabular geometry with wavy sharp bases and tops that can show vertical burrows (*Cylindrichnus*) and can be rarely trough cross-bedded. The medium beds (30 to 50 cm thick) of spiculitic carbonate (F3b) have a wackestone texture containing well-preserved monaxon and tetraxon siliceous sponge spicules (1 to 4 mm long) and a few silt to fine sand-sized reworked volcanoclastic grains (quartz and K-feldspar) from a volcanoclastic protolith. Pumice lapilli (1 to 2 mm diameter) and subrounded micritic intraclasts (2 to 5 cm long) are also found locally. Beds have an irregular tabular or lens-shaped geometry with sharp bases and tops, and are locally bioturbated (*Chondrites bollensis* and *Trichichnus*). Locally, spiculitic carbonate beds are interbedded with medium beds (10 to 60 cm thick) of thinly laminated (0.5 to 5.0 cm thick) marlstone (F3c), including sponge spicules,

tuffaceous and finely comminuted shell hash layers (0.5 cm thick) and rare large ammonites (15 cm diameter).

#### Interpretation

The normally graded and laminated grainy bioclastic carbonate beds (F3a), locally with rare trough-cross-bedding, record episodic high-energy storm-wave reworking (i.e. distal tempestite, Pérez-López & Pérez-Valera, 2012). The presence of *Cylindrichnus* in bioclastic carbonate beds indicates well-oxygenated sea-bottom conditions (Ekdale & Harding, 2015). In contrast, *Chondrites* and *Trichichnus* traces in spiculitic carbonate (F3b) and marlstone (F3c) record a decrease of oxygen levels at the sediment–water interface compared with the carbonate platform deposits (FA1 and FA2). The spiculitic carbonate beds bearing intraclasts, intercalated within marlstones, indicate reworking by low-energy storm-wave events alternating with periods of post-storm settling (i.e. storm-winnowed beds, Pérez-López & Pérez-Valera, 2012). In these fine-grained facies, the well-preserved siliceous sponge megascleres support limited transport and a parautochthonous origin, from a harder carbonate substrate below the storm-wave base. Allochemical bioclastic material and biodetrital carbonate mud in FA3 might have initiated with storm-wave reworking of unconsolidated carbonate platform substrates on the highs (FA1) and efficient exportation of the resuspended mud fraction towards more distal parts of the carbonate system (cf. Pérez-López & Pérez-Valera, 2012). Frequent dilution by volcanic influxes is indicated by pumice and tuffaceous material (D'Atri *et al.*, 1999; Halfar *et al.*, 2004). The lower biota diversity in FA3 (compared to FA1 and FA2) dominated by allochthonous to parautochthonous disarticulated bivalves, brachiopods and siliceous sponges supports deposition at greater water depths than FA1 and FA2. This facies association represents distal periplatform deposits emplaced under moderate to low-energy conditions, near or below the storm-wave base in an offshore-transition environment, with the progressive deepening and reduction from well-oxygenated to moderately-oxygenated sea-bottom conditions. The stacking of distal periplatform deposits (FA3) on proximal periplatform deposits (FA2) in fault-block lows, and carbonate platform deposits (FA1) on fault-block highs, might record the retrogradation of the carbonate system.

#### Facies Association 4: Sand-starved basin

##### Description

Facies Association 4 (FA4) forms poorly stratified, very thin to thin-bedded calcareous mudstone-dominated successions (thickness range of individual successions 20 to 120 m thick), which unconformably overlie FA3 and are overlain by FA5 (Fig. 6D). FA4 is locally affected by significant thickness changes across rift structures (up to 100 m across a few kilometres, see Fig. 5). Calcareous mudstone (F4a) is massive to faintly laminated, with well-preserved dispersed carbonaceous matter, and is mainly composed of silt-size and clay-size carbonate material. Very thin to thin-bedding is monotonous (1 to 10 cm and up to 20 cm thick), commonly deflected by oblate calcareous strata-bound concretions (<15 cm long) and intercalated with thin tuffs (1 to 5 cm thick). Pyrite is present disseminated within discontinuous layers (<0.5 cm thick) parallel to bedding or within elliptical oblong concretions (5 to 8 cm long) (Fig. 8D). Faunal content is represented by small ammonites (2 to 5 cm diameter) and articulated or disarticulated shells of juvenile bivalves (0.5 to 2.0 cm long) distributed along bedding planes, as shell pavements [*Posidonotis cancellata* (Leanza)]. Some thin to medium-beds (5 to 40 cm thick) of massive to graded calcareous mud-rich siltstone (F4b), and rare graded medium to fine-grained bioclastic calcareous sandstone (F4c) with low-angle planar and current-ripple lamination, can be intercalated within mudstone. Bioclastic sandstone beds contain abundant broken skeletal material and have sharp planar or erosional bases with tool marks, and sharp tops (Fig. 8E). Bioturbation in calcareous mud-rich siltstone (F4b) includes small forms of *Chondrites intricatus* and *Phycosiphon* traces.

##### Interpretation

The thin-bedding, massive character and well-preserved carbonaceous matter in calcareous mudstone (F4a) suggest *in situ* pelagic biogenic production by calcareous organisms, which is well-established in the study area during the Early Jurassic (mainly coccolithophorids, Angelozzi & Pérez Panera, 2016). Allochthonous biodetrital carbonate mud plumes exported from platform environments by storm-wave-induced offshore transport (Schieber, 2016; Birgenheier & Moore, 2018) might also have contributed to accumulation of calcareous mudstone. Bioclastic calcareous sandstone (F4c) and siltstone (F4b)

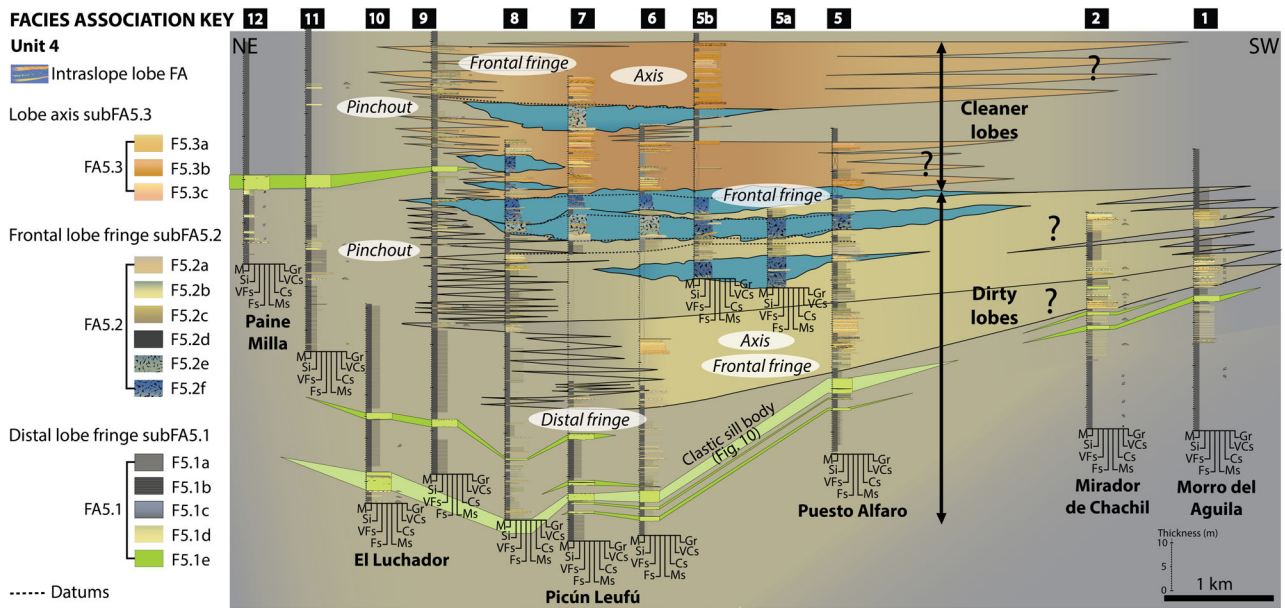


**Fig. 9.** Detailed correlation panel showing the internal architecture and spatial facies distribution within Unit 4 (Lower Los Molles Formation) with dirty and cleaner lobes (sections numbers are shown at top, see Figs 3 and 5 for the location of sections). The stratigraphic increase in bed thickness and grain-size, amalgamation rate and increasing sand content upward in Unit 4 suggest progradation of the lobe complex. Note that lobes pass systematically down-dip and laterally (from section 5 to 9 see Fig. 10) into thinner-bedded (tens of centimetres thick) HEB-rich sandy heterolithic margins (HEB types 2 and 3), which pinch-out farther than the abrupt pinch-out of metres thick debrites (HEB type 1). Note that sections 1 and 2 show a lateral facies change in the dirty lobes whereas sections 5 to 9 show a downdip facies change, according to their dominant north-east palaeocurrent direction (see current directions in Fig. 5). In the cleaner lobes, sections 5 to 9 show a more oblique to downdip facies change, supported by the dominant north-west orientation of sole marks, and a consistent north-east direction recorded by current ripples and cross-bedding (see current directions in Fig. 5).

with normal grading, current ripples and low angle-lamination, in the lower part of FA4, suggest clastic dilution by storm-wave enhanced, bioclastic-rich, low-density turbidity currents (Table 1; Bouma, 1962; Lowe, 1982). The high organic matter content of type II recorded elsewhere in the Lower Los Molles Formation (determined with measurements of organic carbon isotopes and hydrogen index) and with TOC between 2% and 11%, supports a mixture of marine and terrestrial components (cf. Al-Suwaidi *et al.*, 2016). This is consistent with a mixed *in situ* and allochthonous source for mud and organic matter. Preservation of organic matter was favoured by the very limited bioturbation and clastic dilution in this low-energy and low-oxygen environment with low sedimentation rates (cf. Birgenheier & Moore, 2018). Reducing conditions below the seabed promoted pyrite mineralization and pre-compaction seabed diagenetic processes that formed the calcareous concretions, which record very low

sedimentation rates or breaks in sedimentation (Taylor *et al.*, 1995). The pavement-type concentration of juvenile, low-oxygen tolerant bivalve specimens [*Posidonotis cancellata* (Leanza), cf. Damborenea *et al.*, 2013] (see Fig. 2) records episodes of high mortality events and/or condensed surfaces with very low sedimentation rates. Little to no post-mortem bottom current reworking of bivalves, and scarcity of silty and sandy beds, support deposition well below the storm-wave base, consistent with estimations of palaeobathymetry at the base of the Los Molles Formation ranging between 50 to 100 m and 200 to 400 m (cf. Gómez Omil *et al.*, 2002; Gómez-Pérez, 2003).

In summary, this facies association records deposition of pelagic material and allochthonous fine-grained carbonate sediments exported by storms from the coeval drowned carbonate platforms. These sediments deposited in a sand-starved basinal environment with prevailing poorly oxygenated sea-bottom conditions.

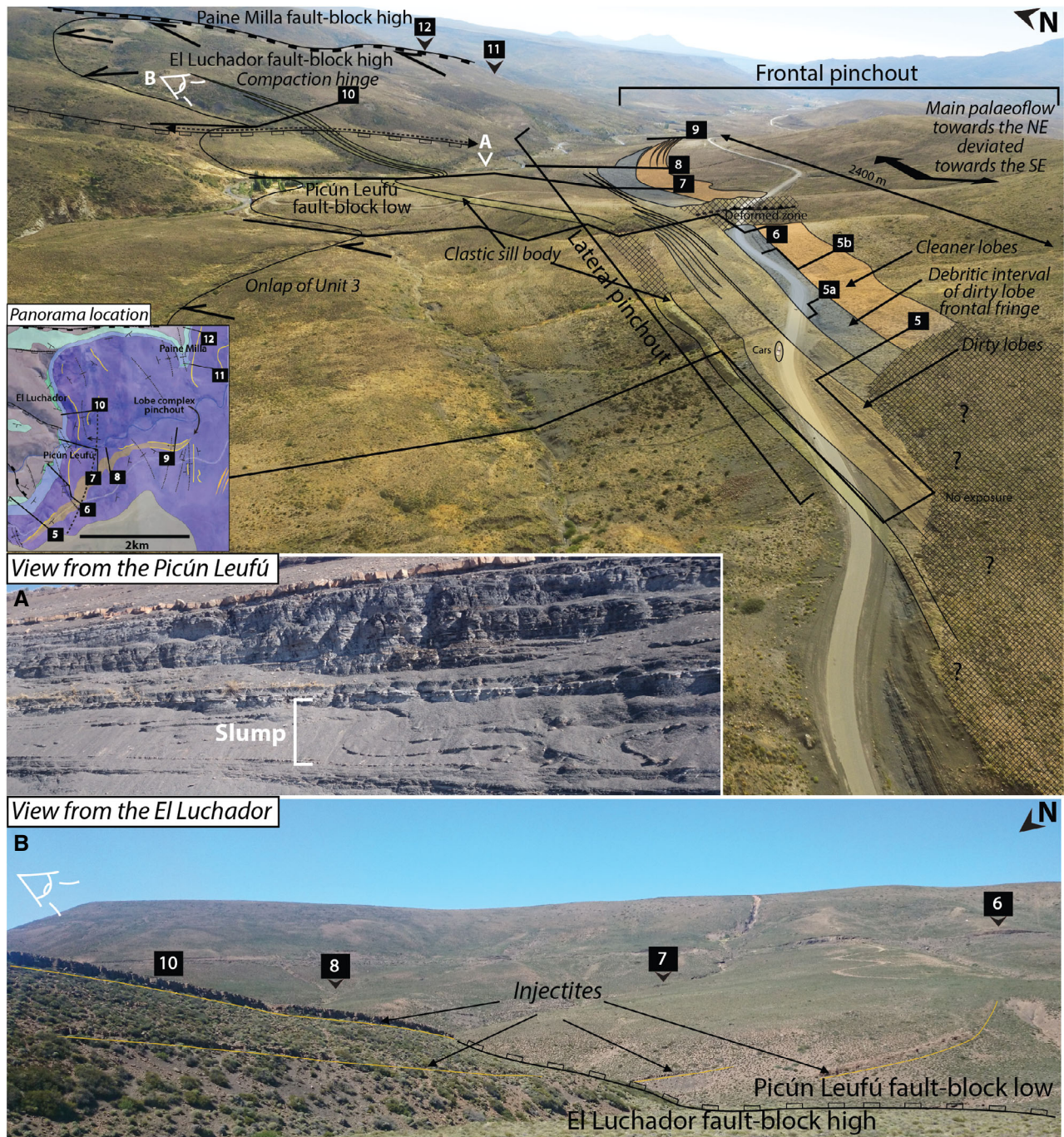


**Fig. 10.** Panoramic view from uncrewed aerial vehicle (UAV) photograph (cars on the road for scale) showing the onlap limit of the Lower Los Molles Formation (Unit 3) onto the Chachil Formation (Units 1 and 2), the location of the compaction hinge and location of dirty and cleaner lobes, which form the intraslope lobe complex (*ca* 5 km minimum wide  $\times$  6 to 8 km long  $\times$  50 to 70 m thick) within Unit 4 (colours for lobes are specified in Fig. 9.). Respective lateral and frontal pinch-outs are indicated. The clastic sill body (1.5 to 3.8 m thick, 5 to 8 km across) (see Figs 5 and 9) steps 1 to 2 km outward from the onlap margins of the lobe complex. (A) View of slumped mudstone and siltstone interval (1.6 m thick and kilometre-scale). (B) View of the clastic sill injectite that splits into smaller sills with abrupt pinch-out terminations across  $<2$  km on the El Luchador fault-block high. Note that the deformed zone is an area affected by inverse faults.

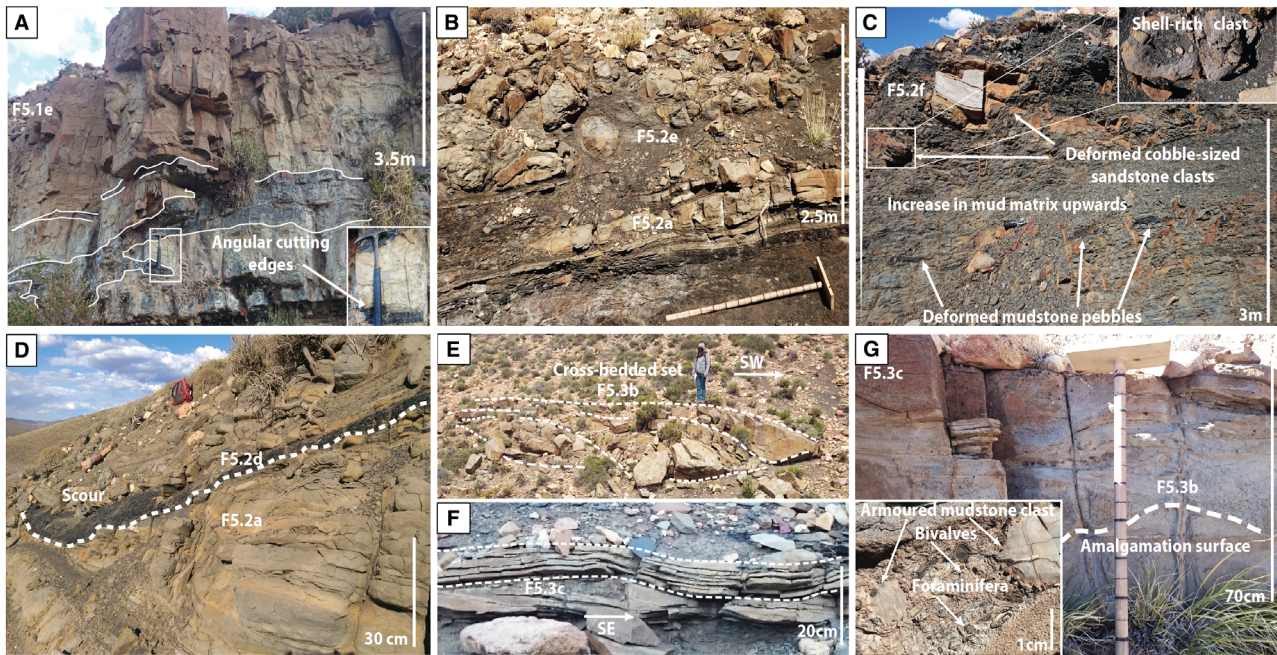


**Fig. 11.** Representative photographs of facies associations. (A) Injected sandstone (F5.1e) showing a single clastic sill body cutting through mudstone (see this same sill section 7 in Figs 5 and 10). (B) Chaotic muddy sandstone (F5.2e) bearing deformed mudstone and sandstone clasts and heterolithic rafts distributed in a patchy medium to fine-grained matrix enriched in mud and clast-depleted at top (in contrast to F5.2f facies). Locally, the bed scours a massive, mud-poor sandstone which, when not eroded can show low amplitude (decimetre-scale) mud-rich bed-waves with low-angle laminae developed at top (F5.2a) (see also HEB type 1 Fig. 12). (C) Chaotic sandy mudstone (F5.2f) characterized by a starry night-like matrix (Haughton *et al.*, 2003) with plant material, floating large mudstone, siltstone and sandstone clasts, which can include ostreid shells (see also HEB type 1 Fig. 12). (D) Massive mud-poor and clast-poor sandstone (F5.2a) with pinch and swell geometry associated with scour (0.4 m deep and 3.0 m wide) filled by homogeneous massive silty mudstone (F5.2d). (E) Massive crudely graded sandstone (F5.3b) stacked into cross-bedded set of scour fill (up to 5 m long and 1.5 to 2.0 m thick). Person for scale is *ca* 1.8 m tall. (F) Medium-grained sandstone showing asymmetrical rounded ripple with low-angle foresets ( $<5^\circ$ ) draped by sinusoidal parallel laminae (F5.3c) (cf. combined-flow bedform). (G) Amalgamated granular sandstone (F5.3b) grading upward into medium-grained sandstone with undulose laminations (F5.3c). Inset to the left shows example of armoured mudstone clast with quartz pebbles and surrounding broken bioclasts (belemnites, bivalve shells and trochospiral globigerinid? foraminifera) locally found in granular sandstone (F5.3b).

### Facies Association 5.1: Intraslope lobes – Distal lobe fringe

#### Description

Facies Association 5.1 (FA5.1) forms well-stratified, thin-bedded muddy heterolithic successions (5 to 30 m thick) (Fig. 6E) that gradationally overlie FA4 (Fig. 6D). Laterally, FA5.1 can transition and interfinger with packages of FA5.2 and FA5.3. FA5.1 (Fig. 9) is dominated by interbedded massive to subtly graded silty mudstone (F5.1a) and pin-striped laminated mudstone (F5.1b) (1 to 20 cm thick) including moulds of both ammonites and small indeterminate bivalves, concentrated in layers parallel to bedding planes. Pin-striped laminated mudstone (F5.1b) contains parallel to low-angle

planar discontinuous laminations of fine sand-bearing and silt-bearing mudstone (0.2 to 2.0 cm thick), providing a streaky bedding pattern (cf. Baas *et al.*, 2016). Thin to medium beds (5 to 20 cm thick) of normally graded sandy siltstone (F5.1c) and fine-grained to very fine-grained sandstone (F5.1d) intercalated in mudstone (F5.1a and F5.1b) form heterolithic packages (up to 5 m thick). Graded sandy siltstone (F5.1c) shows low-angle planar laminations and starved current-ripples, which locally record opposing palaeoflow directions (Fig. 8F). The sandstone beds (F5.1d) are normally graded, with planar parallel or undulose laminations and current-ripples that can show foresets enriched in carbonaceous material. Beds have sharp planar or

irregular erosional bases with scours (10 to 15 cm deep and 0.3 m wide) (Fig. 6E), and sharp or gradational tops, which can show *Chondrites* traces. FA5.1 also contains distinctively greenish-yellowish weathered, well-cemented massive medium or fine-grained sandstone (F5.1e) (Figs 9 and 10). These mainly form laterally extensive (5 to 8 km) subhorizontal bodies (<0.5 to 1.5 m and up to 3.8 m thick) that intersect the surrounding mudstone stratigraphy at low angle (<15°) (Figs 10 and 11A), which are locally associated with rare thin subvertical bodies of similar lithology (up to 30 cm thick and <1 m wide). Discordant sandstone beds can contain planar layers of subspheroidal vugs (0.2 to 1.0 cm diameter) that are typically calcite-filled and restricted to the upper part of beds. These sandbodies have sharp planar or stepped bases and tops and often convex-down pinch-out terminations. Subangular mudstone clasts (2 to 5 cm long) and linear ridges (up to 1 to 2 m long, 20 to 40 cm wide, 10 to 15 cm relief and 0.5 to 1.0 m spacing) oriented north-east/south-west are locally present on their surfaces. Subhorizontal bodies contain large angular rafts of heterolithic strata (10 to 50 cm and up to >1 m across) found '*in situ*' with their long axis parallel to and concordant with bedding of the host stratigraphy.

### Interpretation

Massive to subtly graded mudstone (F5.1a) suggests deposition from waning fine-grained dilute muddy turbidity currents (Stow & Bowen, 1980). The pin-stripped laminated mudstone (F5.1b) was deposited by clay-laden, turbulence-enhanced transitional flows, to lower transitional plug flows (*sensu* Baas *et al.*, 2009), rapidly decelerating with possible shear sorting and mixing that formed thin clay-bearing and silt to sand-bearing stripes (cf. 'streaky bedding' of Baas *et al.*, 2016). Graded structured siltstone and crudely to normally graded sandstone beds (F5.1c and F5.1d) were deposited with tractional reworking by high to low-density turbidity currents allowing differential particle settling (Lowe, 1982; Best & Bridge, 1992). Sparse bioturbation and dissolution of calcitic shells preserved as moulds indicates deposition under more oxygenated sea-bottom conditions than the mudstone deposits of FA4. This can be explained as in the oxic zone, decomposition and remineralization of organic matter produces carbon dioxide, which in turn forms carbonic acid that can lead to dissolution of calcium

carbonate shells (Aller, 1982; Morse *et al.*, 2007). The discordant massive sandstone bodies (F5.1e) lacking any grading or sedimentary structure, with conspicuous cementation and planar layers of sub-spheroidal vugs, are interpreted as clastic injectites including minor, thin dykes associated with laterally extensive thick sills (Hurst *et al.*, 2011). Lack of clay matrix, the presence of subangular clasts, and '*in situ*' rafts, indicate the incorporation of lithified host strata during injection of slow moving laminar flows, and the distribution of large mudstone clasts mantling surfaces of sills might result from entrainment and abrasion by erosive injecting flows (Cobain *et al.*, 2015). Muddy heterolithic successions (FA5.1) with narrow grain-size range, beds with gradational tops and tabular extensive geometry for hundreds of metres, lack of amalgamation, local erosion with few decimetre-scale sandstone-prone scours and sparse bioturbation suggest deposition in a poorly to moderately-oxygenated distal lobe fringe setting (Mutti, 1977; Pr lat & Hodgson, 2013).

### Facies Association 5.2: Intraslope lobes – Lobe fringe

#### Description

Facies Association 5.2 (FA5.2) comprises thin to medium-bedded sandy heterolithic successions (<5 to 25 m thick) (Fig. 6F), including some thick beds, extends for up to 5 km and is transitional to FA5.1, vertically and laterally (Fig. 9). Beds are rarely amalgamated, and include very poorly sorted sandy mudstone and muddy sandstone facies with variable mud matrix and clast content. Bed geometry is irregular, with common pinch and swell and lateral facies changes with abrupt thinning and pinch-out across less than tens of metres (Figs 9 and 10). The distinct facies divisions recognized in individual beds of FA5.2 suggest that they are mainly hybrid event beds (HEBs; *sensu* Haughton *et al.*, 2009) and three main bed types are identified (Fig. 12).

Type 1 HEBs (F5.2a–F5.2e or F5.2f–F5.2c or F5.1d) (1 to 7 m thick) comprise a thick (decimetres to metres thick) chaotic muddy sandstone division (F5.2e or F5.2f) locally either encased between two thinner (tens of centimetres thick) sandier divisions (F5.2a at base and F5.2c or F5.1d at top), or with only the top division present (Fig. 12). Typically, the basal sandstone (F5.2a) (30 to 80 cm thick) is mud-poor, coarse to medium-grained, and massive with

subrounded to subangular mudstone clasts (0.5 to 8.0 cm long). The upper part of the sandstone division can show mud-rich bedforms with low-angle cross-laminae (5 to 10 cm high and wavelength a few decimetres) (cf. bed-waves Baas *et al.*, 2016), and is overlain by a chaotic muddy sandstone (F5.2e) or chaotic sandy mudstone (F5.2f) division (Fig. 12), which can be transitional downdip in a single bed (Fig. 9). The basal sandy division has an irregular pinch and swell geometry and in cases can be found separately (not overlain by the chaotic division; F5.2e or F5.2f), with the top surface scoured and filled by homogeneous massive silty mudstone (F5.2d) (10 to 60 cm thick and 1.5 to 3.0 m wide) (Fig. 11D). Basal sandy divisions (F5.2a) typically pinch-out downdip across less than tens of metres, before pinch-out of the overlying chaotic muddy sandstone (Figs 11B and 12).

The chaotic muddy sandstone (F5.2e) (4 to 6 m thick) is characterized by a very poorly sorted, patchy medium to fine-grained sand-rich matrix bearing oversized granules, coarse sand grains and abundant mud chips. Beds have erosional bases and mounded tops (Fig. 11B). The matrix supports pebble to cobble-sized mudstone and sandstone clasts (5 to 30 cm diameter), deformed sand-streaks (30 cm long) and heterolithic rafts (up to 80 cm long), with mud-rich and clast-poor tops. The chaotic sandy mudstone division (F5.2f) (0.8 to 5.0 m thick) has a very poorly sorted sandy mudstone matrix containing oversized coarse sand grains, plant material and pebble-sized subangular to subrounded mudstone, siltstone and sandstone clasts (5 to 50 cm long), locally including well-preserved shallow-marine ostreid shells (Fig. 11C). The matrix content in these beds increases upward where the largest clasts are segregated, floating in the matrix (Fig. 11C). Locally, the chaotic division (F5.2e or F5.2f) is overlain by a normally graded sandstone with planar to undulose laminations and/or ripples (F5.1d) (<0.2 m thick), or by a clast-rich muddy sandstone (F5.2c) (20 to 60 cm thick) with irregular pinch and swell bed geometry, often mud-filled, and a sheared erosive basal contact (shown in Fig. 6F).

In contrast to type 1 HEBs, type 2 and 3 HEBs have similar facies division thickness <1 m (Fig. 12) and thin and pinch-out across short distances (tens of metres). Type 2 HEBs (F5.2a, F5.2b, F5.2c and F5.2d) (0.6 to 1.0 m thick) comprise a lower, clast-poor and mud-poor massive sandstone division (F5.2a) (5 to 50 cm), and locally a banded sandstone division (F5.2b) (5 to

15 cm thick) that is often eroded by an upper poorly sorted argillaceous division of clast-rich muddy sandstone (F5.2c) (20 to 60 cm thick) (Fig. 12). The clast-rich muddy sandstone (F5.2c) consists of poorly sorted chaotic medium-grained sandstone bearing abundant deformed mudstone clasts (2 to 25 cm long) and mudchips throughout the bed, and is capped by massive silty mudstone (F5.2d) (5 to 10 cm thick). The thin fine-grained banded sandstone (F5.2b) is characterized by alternating planar, sub-parallel to undulose, discontinuous, light mud-poor and dark mud-rich bands (1 to 5 mm up to 2 cm thick) with mudchips (Fig. 12).

Type 3 HEBs (F5.2a, F5.2b and F5.2d) (15 to 60 cm thick) comprise a clast-poor and mud-poor massive sandstone division (F5.2a) (5 to 30 cm thick) passing upward into a thick finer-grained banded sandstone division (F5.2b) (up to 40 cm thick) overlain by massive silty mudstone (F5.2d) (few centimetres thick) (Fig. 12). The banded sandstone (F5.2d), rarely with small elongated mudstone clasts (2 to 5 cm long) at the base, is characterized by planar, sub-parallel to undulose, light mud-poor and dark mud-rich bands (1 to 5 mm thick) and heterolithic bedforms with sandstone–mudstone laminae (cf. Baas *et al.*, 2016; Baker & Baas, 2020). These include low-angle draping laminations associated with symmetrical hummock-like bedforms (15 to 30 cm high and long wavelength *ca* 0.5 m) and asymmetrical large current ripple bedforms, with steeply dipping foresets (>15°) (15 to 20 cm high and a few decimetres long) (Fig. 12).

### Interpretation

Type 1 HEBs (Fig. 12) are interpreted to reflect deposition from a thick forerunning debris-flow associated with development of a basal concentrated density flow as a result of shear mixing at flow-interfaces (with surrounding seawater) during a single flow event (Amy *et al.*, 2005). In these HEBs, the chaotic muddy sandstone (F5.2e) and sandy mudstone (F5.2f) were likely deposited by intermediate to high yield strength debris-flows (*sensu* Talling *et al.*, 2012), with significant entrainment of compacted substrate (Dakin *et al.*, 2013; Talling, 2013). Entrainment of ambient water might have diluted the basal part of the flow enabling substrate erosion and/or hydroplaning (Marr *et al.*, 2001). Fluid mixing at the base of the debris-flow likely played a significant role in decreasing the debris-flow strength below the point at which it could form a rigid plug flow. This resulted in a basal layer (F5.2a) that

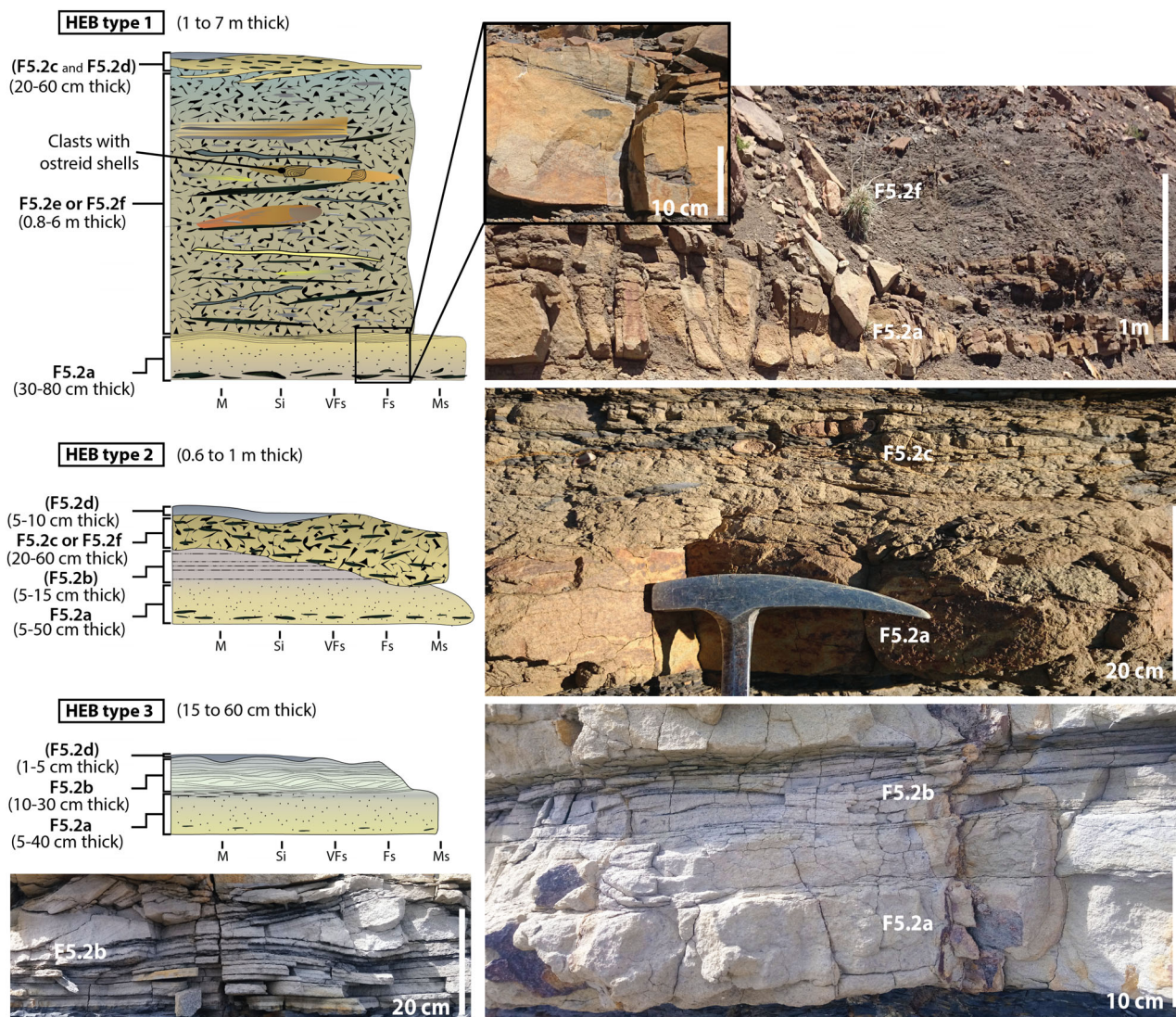


**Fig. 12.** Different Hybrid Event Bed types identified in the intraslope lobes, with some examples in photographs. The facies in brackets are only locally present. HEB type 1 comprises a basal massive mud-poor sandstone with mud-rich bed-waves with low-angle laminae at top (F5.2a) (see inset picture) and pinch and swell geometry, sharply overlain and locally scoured by a chaotic muddy sandstone (F5.2e) or sandy mudstone (F5.2f). This is in turn overlain by a clast-rich muddy sandstone (F5.2c) with pinch and swell geometry and erosive basal contact, and capped by massive silty mudstone (F5.2d) filling topography at top. HEB type 2 comprises a basal massive to laminated mud-poor sandstone (F5.2a) that grades into planar sub-parallel to undulose banded muddy sandstone with mud-chips (F5.2b) that can be absent and eroded by a clast-rich muddy sandstone (F5.2c) capped by massive silty mudstone (F5.2d). HEB type 3 comprises a massive mud-poor sandstone (F5.2a) that grades into a well-developed banded muddy sandstone (F5.2b) locally with mudstone clasts (centimetre-scale) at base and heterolithic bedforms, capped by massive silty mudstone (F5.2d). The banded sandstone can have elongated mudstone clasts (2 to 5 cm long) at the base, and includes planar sub-parallel to undulose and low-angle draping sandy and muddy laminae associated with symmetrical hummock-like heterolithic bedforms and/or asymmetrical large current ripples with high-angle foresets. Note the difference in clast lithology and size between thick HEB (type 1) and thin HEBs (types 2 and 3).

behaved as a transitional flow (Baas *et al.*, 2011), where shearing and breaking of clay particles were likely sufficiently high, and cohesive bed yield strength sufficiently low, to enable the

progressive deposition of sand. Locally, low-amplitude bed-waves (cf. Baas *et al.*, 2016; Baker & Baas, 2020) developed at the top of the basal sand layer beneath slowly decelerated lower to

upper transitional plug flow (*sensu* Baas *et al.*, 2009). In places, this basal sand was eroded to give the pinch and swell geometries that were later infilled with mud trapped by the topography. The development of the basal sandy layer and thus the occurrence of mud-rich bed-waves (F5.2a), as well as variations in the nature of the overlying bed, might be strongly related to lateral changes in debris-flow strength and the irregular erosional behaviour of the debris-flow itself (Talling, 2013). The upper sandy divisions (F5.1d or F5.2c) overlying the debrite might have formed through dilution and shear mixing at the top and front of the debris-flows (Talling *et al.*, 2002; Mohrig & Marr, 2003; Felix *et al.*, 2009). This led either to formation of a turbulent cloud that evolved into a low-density turbidity current (F5.1d), or to increased concentration as a result of mixing with the underlying debris-flow muddy material and evolution into a transient low to intermediate yield strength sandy debris-flow (F5.2c) (Talling *et al.*, 2012).

In type 2 HEBs, the locally developed sub-parallel to undulose banded division (F5.2b) was emplaced beneath rapidly decelerating lower to upper transitional plug flows (Baas *et al.*, 2016; Stevenson *et al.*, 2020). Where present the banded division is frequently cut by a debritic division emplaced by a more cohesive, intermediate (F5.2c) to high (F5.2f) yield strength debris-flow (Talling *et al.*, 2012). In type 3 HEBs, the banded division is well-developed, also including heterolithic tractional bedforms emplaced beneath moderately decelerated turbulence-enhanced transitional flows, to lower transitional plug flows (Baas *et al.*, 2016; Baker & Baas, 2020; Stevenson *et al.*, 2020). The overlying massive silty mudstone cap (F5.2d) records consolidation after deposition of cohesive silty fluid mud flows (Baas *et al.*, 2011). The deposition of HEBs 2 and 3 is linked to thinner decimetre-scale facies divisions in comparison to HEB 1 (Fig. 12). Their development might result from flow bulking through entrainment of clayey substrate (Talling *et al.*, 2004), deceleration and flow transformation of an initial high-density turbidity current into, lower or upper transitional plug flow (HEB 3), and quasi-laminar plug flow or laminar plug flow (type 2 HEBs) (Baas *et al.*, 2011, 2016; Peakall *et al.*, 2020). Note that a forerunning turbidity current (i.e. Houghton *et al.*, 2009) can be excluded in the formation of these type 1 and 2 HEBs as the basal sand layers pinch out prior to the overlying debritic divisions.

Sandy heterolithic successions (FA5.2) show complicated spatial facies relationships and bed thickness changes associated with pinch and swell geometry, common metre-scale mud-filled scours and hybrid event bed development. These characteristics support a lobe fringe sub-environment interpretation (Hodgson, 2009) but with more variable bed thickness pattern, including thick beds, with more erosion, flow transformation and HEBs present in both frontal and lateral lobe fringes (*sensu* Spychala *et al.*, 2017), and associated with the development of heterolithic bedforms (Baker & Baas, 2020; Stevenson *et al.*, 2020).

### **Facies Association 5.3: Intraslope lobes – Lobe axis**

#### *Description*

Facies Association 5.3 (FA5.3) forms crudely to well-stratified, medium to thick-bedded sandstone-dominated successions (5 to 12 m thick) (Fig. 6G and H), which can include some HEBs and transitionally overlie or pass downdip into FA5.2 (Fig. 9). Tabular extensive sandstone packages (1.5 to 5.0 m thick) are characterized by amalgamated bed contacts with up to 20 cm relief marked by abrupt grain-size breaks and mudstone clasts, or comprise thin mudstone interbeds (5 to 15 cm thick). The upper parts of sandstone beds are locally intensely burrowed by *Planolites* and *Chondrites*.

Massive to crudely stratified sandstones (F5.3a) form medium to thick beds (0.5 to 1.2 m thick), which are poorly sorted, mud-poor (i.e. low argillaceous matrix compared to FA5.1 and FA5.2 facies), coarse to medium-grained and locally structured with diffuse planar parallel laminations (1 to 3 cm thick). Beds are often amalgamated, with sharp planar or erosional bases displaying groove casts and bearing elongated discrete subrounded lithic granule to pebble-sized mudstone clasts (1 to 6 cm long). When not amalgamated, the upper part of beds can grade crudely into banded muddy sandstone (F5.2b) and/or laminated fine-grained sandstone (F5.1d).

Granular sandstone (F5.3b) forms thin to medium beds (5 to 90 cm thick), which are very poorly sorted, very coarse-grained or coarse to medium-grained, structureless and weakly normally graded into structured medium-grained sandstone (F5.3c). Locally, it can contain abundant subangular granule-sized grains (0.2 to 0.4 cm diameter) and pebble-size mudstone and siltstone clasts (5 to 8 cm long), forming either

an inverse grading pattern near the bed base or a coarse-tail grading pattern throughout beds. Some mudstone clasts armoured with a mix of quartz pebbles and bioclasts, including fragments of belemnites, bivalve shells and planktonic foraminifera (possibly *Globigerinids*), can be found in these beds (Fig. 11G). Beds can be isolated with erosional bases and sharp tops, or amalgamated. Locally, they can stack into cross-bedded sets (1.5 to 2.0 m thick, up to 5 m wide) dipping up to 10° (Fig. 11E).

Structured medium-grained sandstone (F5.3c) forms moderately sorted and normally graded, thin to medium beds (5 to 30 cm thick). They comprise swale-like and hummock-like low-angle draping cross-laminations and trough-cross-laminations associated with hummocky bedforms (10 to 25 cm high and wavelength of few decimetres). They also comprise decimetre-scale asymmetrical rounded ripples with low-angle foresets (<5°), convex-up lee and stoss sides, draped by sinusoidal parallel laminae (Fig. 11F). F5.3c beds have sharp bases and wavy tops overlain by graded structured sandy siltstones (F5.1c) or structured fine-grained sandstone (F5.1d).

### Interpretation

Massive to crudely stratified coarse to medium-grained sandstones (F5.3a) were deposited with high sediment fallout rates that could suppress traction (Kneller & Branney, 1995). Lower fallout rates and collapse of high concentration near-bed laminar sheared layers enabled the formation of diffuse laminae (Sumner *et al.*, 2008). Massive granular sandstone with crude normal or inverse to normal coarse-tail grading (F5.3b) suggests near-bed transport of highly concentrated coarse particles with bedload traction and deposition by high-density to hyperconcentrated density flows (Lowe, 1982; Mulder & Alexander, 2001). Structured medium-grained sandstone (F5.3c) was deposited by traction-plus-fallout beneath stratified high-density combined flows, with high sediment fallout rates, but enabling bedform aggradation in the upper-stage plane bed stability field and bedform migration with bedload traction (Tinterri, 2011). Asymmetrical rounded ripples formed with a dominant unidirectional flow component, whereas symmetrical hummocky bedforms might have developed with a dominant oscillatory combined flow component (Tinterri, 2011). The oscillatory flow component could not originate with surface waves given the absence of wave-induced or

storm-induced structures and the low diversity of bioturbation traces in FA5, which point to deposition from sediment gravity flows below the storm-wave base. Alternatively, these bedforms are interpreted to form from flow deflection against a confining slope, and resulting interactions of reflected internal wave trains with the near-bed unidirectional flow component (cf. Tinterri, 2011). The effects of confinement and basin configuration are discussed in the section about Unit 4.

Medium to thick-bedded sandstone-dominated successions (FA5.3) comprise amalgamated sandy packages (1.5 to 5.0 m thick, *ca* 1 to 2 km across) of continuous tabular beds with basal erosion (<0.6 m deep) and locally narrow and shallow incisional features interpreted as sandstone-prone scour-fills (1.5 to 2.0 m deep, *ca* 5 m long), suggesting a lobe axis sub-environment (Etienne *et al.*, 2012; Prélat & Hodgson, 2013). The increase in bioturbation intensity compared with FA5.1 indicates deposition in a moderately to well-oxygenated environment, consistent with frequent extrabasinal siliciclastic influxes.

## SYNTHESIS OF DEPOSITIONAL SYSTEMS AND ARCHITECTURE OF TECTONO-SEDIMENTARY UNITS

Genetic facies relationships described in the previous section and stratal relationships across structures described in this section allowed four tectono-sedimentary units to be defined (Figs 3 and 5). Analysis of the spatial facies distribution, palaeocurrents, thickness changes, stratal bounding surfaces and associated angular relationships between units are used to decipher the late syn-rift to early post-rift evolution of sedimentary systems during the Early Jurassic (Figs 2 and 13). Units 1 and 2 belong to the Chachil Formation, and Units 3 and 4 correspond to the Lower Los Molles Formation. Present-day mean bedding dip-directions have been calculated for each unit in the three different geographic zones (Fig. 4) in order to show the differences in bed orientation and dip, and unconformities, between the different units and structural domains. In each zone, there is a stratigraphic decrease in stratal dip angle and from a multidirectional dip-direction pattern to a dominant east/south-east dip azimuth trend (Fig. 4). The terms 'proximal' and 'distal' refer to the position relative to the Southern Chachil Graben margin (Fig. 3A).

## Unit 1

Unit 1 includes carbonate platform deposits (FA1) that onlap onto fault-block highs with an angular discordance between *ca* 4° and 14° and proximal periplatform deposits (FA2) that onlap onto fault-block lows with an angular discordance between *ca* 11° and 15° (Fig. 5). Carbonate platform deposits (FA1) have moderate stratal dip angles (*ca* 16 to 25°) with an east/south-east dip direction on the Morro del Aguila (Zone SW) and Puesto Alfaro (Zone Central) fault-block highs, and a south-west dip direction on the El Luchador fault-block (Zone NE) (Fig. 4). Proximal periplatform deposits (FA2) show moderate stratal dip angles (*ca* 20°) with an east dip direction in the Mirador de Chachil fault-block low (Zone SW) and higher dip angles (*ca* 33°) with a south dip direction in the Picún Leufú fault-block low (Zone Central) (Fig. 4).

The fault-block carbonate platforms (FA1) are detached from the basin margin (*sensu* Bosence, 2005) (Figs 7 and 13A), and exhibit subtle internal growth stratal patterns with pinch-out towards the crest of rotated fault-block highs in the immediate hangingwall, downdip of the Southern Chachil Graben margin (Figs 5 and 7). The Morro del Aguila and the Paine Milla fault-blocks host extensive carbonate platforms (2 to 5 km length and width, up to 40 m thick) dominated by micritic tuffaceous carbonate (F1a). The platform, nucleated on the Puesto Alfaro fault-block highs, is dominated by fossiliferous laminated carbonate (F1b) (Fig. 7). The fauna of Unit 1 records the flourishing of a suspension feeder-dominated carbonate-secreting benthos including subtidal encrusters (scleractinian corals, bryozoans and crinoids) and shelly biocalcifiers (bivalves and brachiopods), which ensured productivity of the warm-temperate carbonate system (cf. Flügel, 2004). Although Unit 1 might record the downdip reworking of higher-energy inner ramp deposits, the limited exposure does not enable the reconstruction of the 3D geometry and complex facies distribution of the carbonate system. On the Southern Chachil Graben margin, a tide-influenced inner carbonate platform with tidal flats and subtidal ponds developed, and recorded shallowing-upward cycles with progradation of intertidal and supratidal deposits onto subtidal deposits (Armella *et al.*, 2016). Carbonate sedimentation on the horst which formed the Southern Chachil Graben margin (Fig. 3) was strongly affected by ash-fall and episodic subaerial exposure associated with

firmground development in peritidal conditions, oxide coated surfaces and *Glossifungites* ichnofacies (Armella *et al.*, 2016). Nonetheless, these surfaces associated with subaerial exposure have not been observed on the smaller fault-block highs within the Chachil Graben, suggesting that they remained submerged (Fig. 3). Therefore, a combination of subaerial degradation on the Southern Chachil Graben margin and enhanced current erosion of fault-block highs might have controlled extensive reworking of the poorly consolidated carbonate platform deposits (FA1) and volcano-sedimentary substrate into proximal periplatform deposits (FA2).

Mixed carbonate-clastic proximal periplatform deposits (FA2) accumulated in the Mirador de Chachil and Picún Leufú fault-block lows with onlap onto volcano-sedimentary syn-rift deposits (Lapa Formation) and pinch-out towards intervening fault-block highs (Figs 7 and 13A). The polymict composition of pebbly conglomerates (F2a), dominated by brecciated reworked volcaniclastic material, were deposited by hyperconcentrated density flows that originated from small-scale failures (cf. Drzewiecki & Simó, 2002) triggered by fault-block tilting and destabilization of primary volcanic deposits (Lapa Formation) (Fig. 13A). Similar deposits identified as basal conglomerates of the Chachil Formation have been recognized in the subsurface in the south-east of the Neuquén Basin, and are interpreted as evidence for subaerial exposure and degradation of the Precuyano Cycle deposits (Schiuma & Llambías, 2008). Calciturbidite deposits (F2b) can be compared to carbonate platform-derived calciclastic aprons lacking internal organization and with local development of basal lags in small channel-fills (cf. Braga *et al.*, 2001; Payros & Pujalte, 2008). The stratigraphic increase in proportion and sorting of grainy allochemical carbonate material, sourced from carbonate platforms on fault-block highs, recorded throughout FA2 might reflect the decreased availability of the volcano-sedimentary syn-rift substrate for reworking due to progressive onlap into fault-block lows, together with a decrease of destabilization events with fault-block tilting.

South-south-east oriented palaeocurrents (Fig. 5), stratal fanning of proximal periplatform deposits (FA2) in the Mirador de Chachil fault-block low (5 to 25 m thick across 3 to 4 km) towards the Morro del Aguila fault-block high, and relative sea-level fall and subaerial exposure of the Southern Chachil

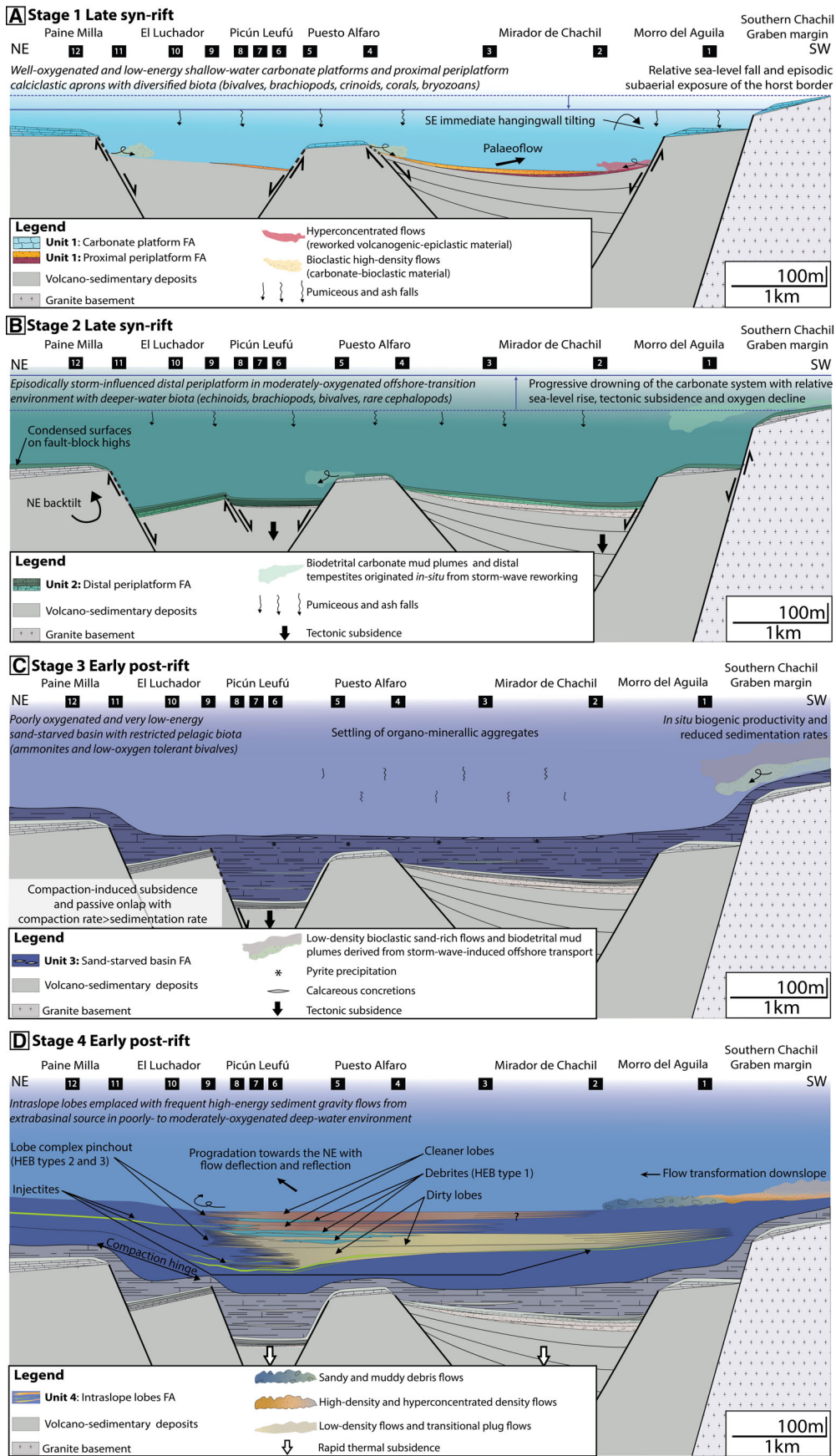


**Fig. 13.** Palaeogeographic evolution of the Chachil Graben illustrated in schematic cross-sections (not restored) showing changes of depositional setting, facies distribution and inferred fault-block motion during deposition of the units (see the precise timing, Fig. 2). Note that the syn-rift to post-rift transition is marked by a change from intrabasinal carbonate to extrabasinal siliciclastic sediment supply, and a change of sediment dispersal, from axial to transverse to the strike of rift structures, as the inherited topography becomes healed. Section numbers are shown at top (see Figs 3 and 5 for the location of sections).

Graben margin, suggest active faulting and south-eastward tilt of the Mirador de Chachil fault-block low. Facies distribution, depositional geometries and variability of stratal dip azimuths across structures (Figs 3 and 4) reflect active fault-block rotation during deposition of Unit 1 and support its late syn-rift development (Cross & Bosence, 2008; Dorobek, 2008).

## Unit 2

Unit 2 corresponds to mud-rich mixed carbonate-clastic distal periplatform deposits (FA3) that form wedge-shaped packages in fault-block lows, thin drapes on fault-block highs, and onlap onto Unit 1 to form a *ca* 3° to 10° angular discordance (Fig. 5). In the Mirador de Chachil proximal fault-block low (Zone SW) and Picún Leufú distal fault-block low (Zone Central), Unit 2 presents moderate stratal dip angles (*ca* 18 to 32°) and consistent east/south-east dip direction. This contrasts with the higher dip angles (*ca* 62°) and the north-east dip direction of Unit 2 across the El Luchador fault-block (Zone NE), which record the overprint of later inversion tectonics (Fig. 4).

Bioclastic carbonate (F3a) deposited in the Mirador de Chachil proximal fault-block low shows thinning (20 to 12 m thick across 3 to 4 km) and onlap onto calciturbidite (F2b) towards the Puesto Alfaro fault-block high (Figs 5 and 7). These deposits are overlain by interbedded spiculitic carbonate and marlstone (F3b–F3c) that thin (15 to 5 m thick) towards the Puesto Alfaro fault-block high. Bioclastic carbonate (F3a) also thins (18 to 8 m thick across <2 km) from the El Luchador fault-block high towards the Picún Leufú fault-block low (Figs 7 and 13B). Overlying interbedded spiculitic carbonate and marlstone (F3b and F3c) thin (from 10 to 5 m thick) from the Picún Leufú fault-block low towards the El Luchador fault-block high (Figs 7 and 13B). On the Morro del Aguila, Puesto Alfaro and Paine Milla fault-block highs, bioclastic and spiculitic carbonate (F3a and F3b) are absent and carbonate platform

deposits (F1a and F1b) are draped by marlstone (F3c) (5 to 10 m thick) (Figs 7 and 13B). This contact is marked by *Pascichnia* grazing traces at the top of carbonate platform deposits representing a condensed surface on the fault-block highs due to sedimentation under poorly oxygenated and relatively deep bottom water conditions (Ekdale & Mason, 1988). A similar situation is observed on the Southern Chachil Graben margin where the carbonate platform deposits are overlain by marlstone (e.g. Armella *et al.*, 2016).

The stratigraphic deepening recorded by Unit 2 provides strong evidence for fault-controlled subsidence, given that tectonically induced relative sea-level changes could outpace the low-amplitude and rates of eustatic rise during Early Jurassic greenhouse time (cf. Ravnås & Steel, 1998). Deepening and reworking of unconsolidated carbonate platforms (FA1) on the most elevated fault-block highs bounding the graben, promoted redeposition of allochemical fine biotrital carbonate material (FA3) in fault-block lows (e.g. Halfar *et al.*, 2004). The thinning-upward and fining-upward trend of Unit 2 deposits in the Mirador de Chachil and Picún Leufú fault-block lows, and thickening towards the Morro del Aguila and Puesto Alfaro fault-block highs dominated by condensed sedimentation, support syn-depositional relative sea-level rise and differential subsidence (Fig. 13B). The stratal pattern suggests an increased displacement along the Chihuido Bayo fault system bounding the Chachil Graben and localized normal faulting in the main hangingwall with formation of the El Luchador fault-block high (Fig. 13B).

Tectonic subsidence and relative sea-level rise outpaced carbonate sedimentation rates and controlled retrogradation of the carbonate system. Drowning of the carbonate system culminated with establishment of a deep-marine environment and reduction of oxygen recorded near the top of Unit 2 from the Southern Chachil Graben margin to the interior of the Chachil Graben. The deterioration of chemical and physical

conditions with tectonically-induced relative sea-level rise contributed to drowning of the carbonate factory across the entire Chachil Graben (e.g. Santantonio, 1994; Ruiz-Ortiz *et al.*, 2004; Navarro *et al.*, 2012).

### Unit 3

Unit 3 forms a calcareous mudstone-dominated succession (FA4), which overlies Unit 2 locally with an unconformable relationship, with a *ca* 3° to 9° bedding difference between Unit 2 and Unit 3 at the graben margins. Dip angles are moderate (*ca* 16° to 25°) with general south-east dip direction in the Mirador de Chachil proximal fault-block low (Zone SW) and Picún Leufú distal fault-block low (Zone Central). This contrasts with higher dip angles (*ca* 57°) with some east/south-east dip direction measured in the deformed strata affected by later inversion tectonics across the El Luchador fault-block (Zone NE) (Fig. 4).

The base of Unit 3 infills the intrabasinal topography inherited at the top of Unit 2 burying the Puesto Alfaro fault-block highs, and therefore records a change of basin geometry with infilling of the inherited rift topography. This is supported by the thinning of Unit 3 (<20 m thick) to the north-east across the El Luchador and Paine Milla fault-block highs and to the south-west across the Morro del Aguila, and by the thickening (70 to 120 m thick) from the Mirador de Chachil to Picún Leufú fault-block low (Fig. 5). The deformed steeply dipping strata of Unit 3 near the El Luchador fault-block (Zone NE) is associated with abrupt mudstone thickening (up to 100 m offset of compacted strata) across less than 2 km from the Paine Milla platform towards the adjacent Picún Leufú fault-block low (Figs 5 and 13C). This thickness change occurred across north-west/south-east striking and south-west dipping rift faults involved in the formation of the El Luchador fault-block (Fig. 13B). The potential process that caused small-scale deformation recorded in Unit 3 is detailed in the *Discussion*.

The occurrence of *Posidonotis cancellata* (Leanza) shell pavements in the lower part of Los Molles Formation has been reported in TOC-rich mudstone of another marine rift depocentre, located 20 km south-east of the Chachil Graben (Al-Suwaidi *et al.*, 2016). Al-Suwaidi *et al.* (2016) report negative carbon isotope excursions associated with the Toarcian Oceanic Anoxic Event (TOAE) during the late

*Tenuicostatum*–early *Dactylioceras Hoelderi* Andean Ammonite Biozone (AAB 15 to 16) (Fig. 2). The TOAE might be recorded in Unit 3, which spans the latest Pliensbachian–Early Toarcian in the Chachil Graben, marked by a reduction of benthic fauna diversity recorded from Unit 2 to Unit 3 (Fig. 2) and variable sedimentation rates related to important storm activity under a warm temperate climate (cf. Volkheimer *et al.*, 2008). These conditions prevailed over south-western Gondwana, and were not favourable for the deposition of organic black shales, which characterize the TOAE in the Northern Hemisphere, where a warm and humid climate favoured the development of anoxia (Dera & Donnadieu, 2012; Fantasia *et al.*, 2018). The stratigraphic evolution from carbonate to terrigenous mudstone recorded at the top of Unit 3 (Fig. 6D) marks the transition to Unit 4 and indicates an increase of fluvio-deltaic runoff, which could be related to climatic change towards more humid conditions from the early Late Toarcian (cf. Volkheimer *et al.*, 2008).

### Unit 4

Unit 4 represents a submarine lobe complex (*sensu* Prélat *et al.*, 2009) whose base is transitional with, or sub-concordant to Unit 3, except around the El Luchador fault-block (Zone NE) where it shows an angular discordance between *ca* <1 to 8° onto Unit 3. Steeper dips in Zone NE, with bedding differences of up to 36° between Unit 3 and 4 (Fig. 4), are related to structures that formed during later inversion tectonics, but these are highly localized and overall the depositional architecture remains well-preserved. Dip angles of Unit 4 are moderate (*ca* 16° to 21°) with consistent east/south-east dip direction (Fig. 4). Unit 4 heals across structures and shows general thickness changes with thickening (150 to 170 m thick) from the Mirador de Chachil to the Picún Leufú fault-block low and thinning (50 to 100 m) across the Morro del Aguila, El Luchador and Paine Milla fault-block highs (Figs 5 and 9).

The lower part of Unit 4, dominated by muddy heterolithic strata, corresponds to distal lobe fringes (FA5.1) with a low sandstone proportion (Figs 9 and 10). The upper part of Unit 4 is characterized by a higher proportion of sandstone and includes stacked sandy heterolithic strata in lobe fringes (FA5.2), sandstone-dominated strata in lobe axes (FA5.3) and

minor muddy heterolithic strata in distal lobe fringes (FA5.1) (Fig. 9). Individual lobes have a low aspect ratio (1.5 to 5.0 m thick, few kilometres across) and collectively these deposits form a 50 to 70 m thick, *ca* 5 km minimum wide and 6 to 8 km long intraslope lobe complex (Figs 9 and 10). The intraslope lobe complex comprises basal dirty lobes (Figs 9 and 12) mainly represented by lobe fringe deposits with a high proportion of HEBs (types 1, 2 and 3) and locally by lobe axis deposits (Fig. 6G). The dirty lobe deposits are characterized by a finer grain-size, argillaceous matrix and high clast content. The overlying cleaner lobes include lobe axis deposits (Fig. 6H), locally with thick HEBs (type 1), and lobe fringe deposits with thin HEBs (mainly types 2 and 3) (Figs 9 and 12). The cleaner lobe deposits are characterized by thicker beds, coarser grain-size and lower argillaceous matrix and clast content (Figs 9 and 14).

The intraslope lobe complex within Unit 4 records a rapid increase of extrabasinal siliciclastic supply, favouring oxygenation and increase of bioturbation intensity and diversity (Figs 2 and 13D), consistent with the warming humid climate (cf. Volkheimer *et al.*, 2008). The increase in volume and frequency of sand-rich sediment gravity flows over time, associated with the stratigraphic increase in bed thickness and grain-size, amalgamation rate, and increasing sand content upward in the lobes of Unit 4 suggest progradation of the lobe complex (Craigh & Steel, 2004; Macdonald *et al.*, 2011). The slightly shingled pattern of lobe sub-environments, high thickness and facies variability across short distances (100 m) (Fig. 9), palaeocurrent evidence for flow reflection and deflection (Fig. 5), and widespread erosion and scouring in proximal and distal lobe fringe settings (Figs 6E, 6F and 11D) may result from the development of lobes in a partially confined setting (Figs 10 and 13D).

Partial confinement could have been controlled by inherited topography across the El Luchador fault-block high, which formed a south/south-west-facing oblique counterslope that could have influenced sediment gravity flow behaviour and led to deviation of the general north-east flow direction mainly towards the south-east and rarely south-west (Fig. 5). This could explain the opposing directions recorded in current-ripple laminations (Fig. 8F) and combined-flow bedforms (Figs 11F and 12), showing azimuth dispersion up to 180° and sole

marks (mainly grooves) with average azimuth dispersion of 45° (see palaeocurrents, Fig. 5). Interaction of flows with relief is suggested by the development of a range of combined-flow bedforms (Fig. 11F) (cf. Tinterri, 2011) and heterolithic bedforms (Fig. 12), which could indicate seabed topography (cf. Hofstra *et al.*, 2018). Therefore, these bedforms with multiple palaeoflow directions might have developed with oblique flow reflection and deflection (i.e. Kneller *et al.*, 1991; Amy *et al.*, 2004) against the counterslope flanking the El Luchador fault-block high (Figs 13D and 14).

Partial confinement is further supported by the abrupt thinning of thick-bedded amalgamated sandstone bedsets (1.5 to 5.0 m thick) across a few kilometres, without marked grain-size or sorting change and by the frontal pinch-out pattern of the lobe complex. The lobes pass systematically down-dip into thinner-bedded (tens of centimetres thick) HEB-rich sandy heterolithic succession (HEB types 2 and 3), which pinch-out farther than the abrupt pinch-out of metres thick debrites (HEB type 1) (Figs 9 and 12) (see *Discussion*).

The presence of the sill-dominated injectite network stratigraphically above, below and lateral to the lobe complex, and their pinch-out towards the Paine Milla fault-block high, supports the influence of inherited topography. The relief that induced substantial confinement of lobes would also have later promoted overpressure and clastic injection (e.g. Cobain *et al.*, 2017). Laterally extensive sills (1.5 to 3.8 m thick, 5 to 8 km across) step 1 to 2 km outward from the onlap margins of the lobe complex and split with abrupt pinch-out terminations across the El Luchador fault-block high (Fig. 10). The linear ridges present on the surface of some sills show a general north-east/south-west orientation which supports a north-west/south-east direction of crack propagation, approximately parallel to the south/south-west-facing counterslope (e.g. Kane, 2010). This together with the offset pinch-out between lobes and sills at this location might reflect the influence of the buried El Luchador fault-block high on the morphology of the injectite complex (e.g. Cobain *et al.*, 2017).

The overpressure prior to injection may have been a combination of: (i) deep-seated hot basinal fluid and gas expulsion through rift faults related to a mature hydrocarbon plumbing system in the syn-rift deposits and/or sourced from crustal magmatic activity; and (ii)

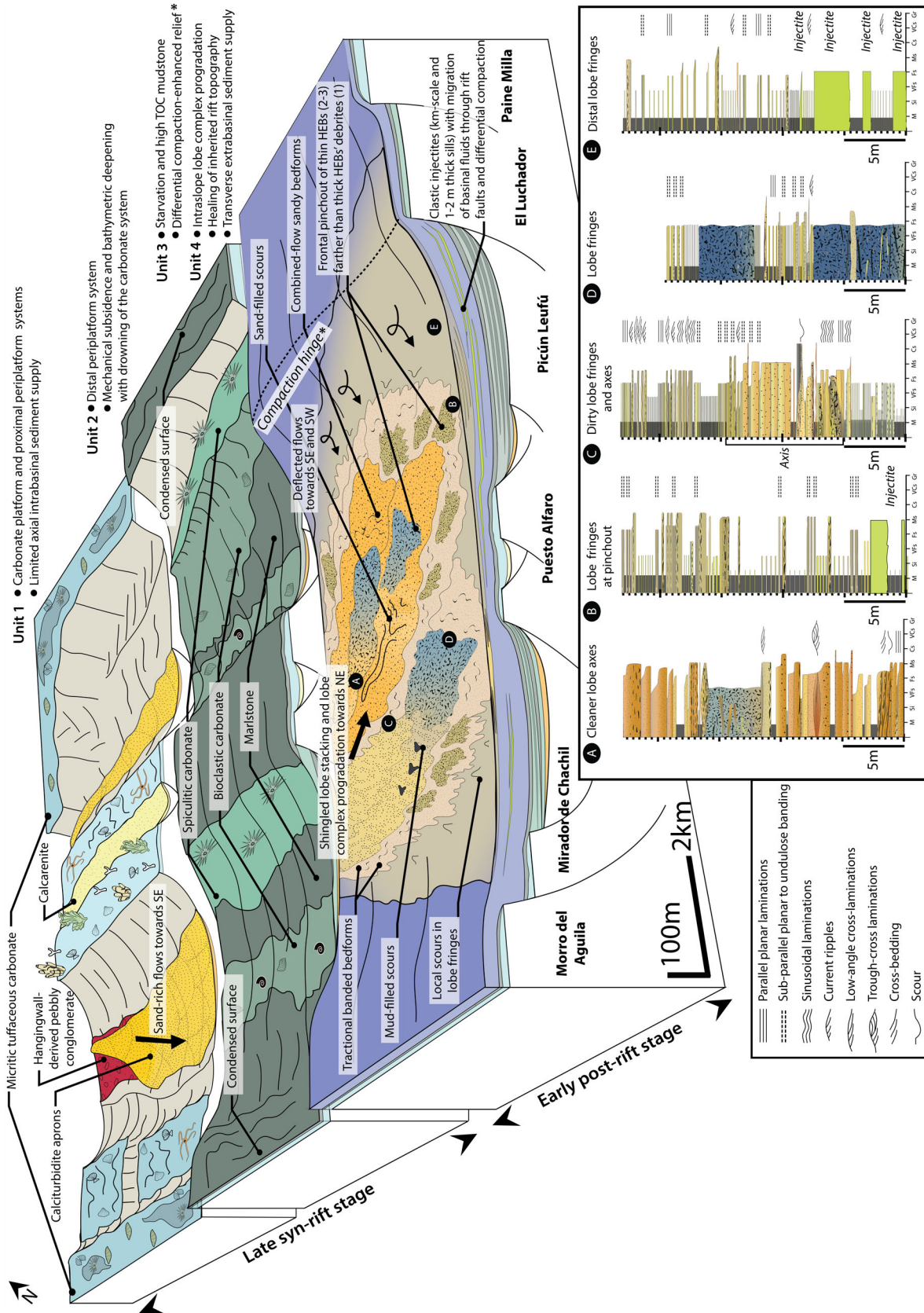


**Fig. 14.** Block diagram showing the evolution of sedimentation patterns and interactions with topography in the Chachil Graben from an underfilled to a sediment-balanced depocentre during the syn-rift to post-rift transition, detailing relationships between facies distribution and structures. Detailed logs in lobes show typical facies association of different lobe sub-environments in both dirty and cleaner lobes. Lobe axis includes medium to thick-bedded sandstone-dominated successions with amalgamated packages (1.5 to 5.0 m thick) and can comprise HEBs, which form intralobe fluid flow baffles. Lobe fringe includes thin to medium-bedded sandy heterolithic successions dominated by HEBs. Distal fringe includes thin-bedded muddy heterolithic successions dominated by pin-striped mudstone and sandstone with common streaky bedding (i.e. banding). Intraslope lobes are characterized by significant erosion in axis and fringe, and well-developed tractional banded/heterolithic bedforms and combined flow bedforms and thin across a few kilometres, without marked grain-size or sorting change. Note the frontal pinch-out of the lobe complex into thinner-bedded (tens of centimetres thick) HEB-rich sandy heterolithic succession dominated by HEB types 2 and 3, which pinch-out farther than the abrupt pinch-out of metres thick debrites of HEBs type 1.

differential loading and compaction of buried strata (e.g. Boehm & Moore, 2002; Kane, 2010). Widespread expulsion of basal fluids has been reported locally with the formation of methane seepages associated with development of bioherms at the seabed during deposition of the Lower Los Molles Formation (Gómez-Pérez, 2003), which is equivalent to Unit 3 of this study. This would be consistent with a primary mechanism of overpressure build-up. Migration of basal fluids into the shallowly buried but tilted sandstone bodies of Unit 4 may have triggered injection (e.g. Cobain *et al.*, 2017), although a seismic trigger for injection cannot be ruled out.

## DISCUSSION

### Early post-rift inherited topography

The analysis of the syn-rift to post-rift transition in the Chachil Graben has revealed major thickness changes within the organic-rich mudstone (Unit 3) across the Paine Milla–El Luchador fault-block high, and the role of topography recorded by intraslope lobe architecture (Unit 4). The local and small-scale character of deformation in early post-rift strata of the Lower Los Molles Formation, which has not been observed elsewhere in other adjacent depocentres at a regional-scale, is consistent with the end of rift-related extension at that time in the study area. Here, the processes and significance of this deformation are discussed.

#### Unit 3

Local thickness change (>100 m of compacted strata) at the transition between the Paine Milla–El Luchador fault-blocks and the adjacent Picún

Leufú fault-block low must have been accommodated across a major buried/blind rift structure during deposition of Unit 3 (Figs 3A and 5). The limited facies and thickness changes in Unit 2 across this fault do not support a large bathymetric difference between the El Luchador fault-block high and the adjacent Picún Leufú fault-block low at this time (Figs 7 and 13B). Therefore, additional differential subsidence across this fault occurred after deposition of Unit 2 to create accommodation in the Picún Leufú fault-block low associated with thickening of the mudstone-dominated succession of Unit 3 (Figs 5 and 13C). The presence of syn-depositional topography across the fault during deposition of Unit 3 is further supported by the facies change from calcareous mudstone with interbedded siltstone and bioclastic sandstone beds in the Picún Leufú fault-block low, to condensed homogeneous mudstone on the El Luchador and Paine Milla fault-block highs. The presence of multiple tuff beds, which act as markers, in Unit 3 (and more rarely in Unit 4) on fault-block highs and lows support that these facies changes in mudstones were stratigraphically equivalent. The sedimentation rates from compacted strata (cf. McArthur *et al.*, 2013) are estimated at 4.3 m/Myr in Unit 3 considering the maximum sediment thickness on the structurally elevated fault-block highs, and 27.6 m/Myr considering the maximum sediment thickness in the axis of the Picún Leufú fault-block low. These rates are based on measured thicknesses of compacted strata (Fig. 5), taking into account the minimum thickness (*ca* 20 m thick) on fault-block highs and maximum thickness (*ca* 127 m thick) in the deepest fault-block low (Picún Leufú). The duration of deposition of Unit 3 of *ca* 4.6 Myr is based on the biostratigraphy (using the *Posidonotis cancellata* biozone at the base of Unit

3), and U-Pb ages at the base ( $184.4 \pm 2$  Ma) and top ( $179.8 \pm 1.4$  Ma) of Unit 3 (Privat, 2019) (see Fig. 2). Whilst sedimentation rates are estimates, they are in the range of pelagic sedimentation rates similarly calculated from compacted mudstone strata in the Kimmeridge Clay Formation (20 to 45 m/Myr, cf. McArthur *et al.*, 2013), which comparably formed an extensive, organic-rich mudstone blanket across rift topography in the North Sea. Moreover, stratigraphic geometries of Unit 3 and Unit 4 record the long-lived influence of this fault-block relief, which is postulated to have formed a compaction hinge above the inferred blind fault tip that controlled deep-water sediment dispersal during deposition of Unit 4 (Figs 13D and 14). If syn-depositional relief was formed with rift-related extensional tectonics, one might expect near-fault damage (for example, fracturing and folding) and widespread normal faulting in other parts of the Chachil Graben and in adjacent depocentres, which is not the case.

This study examines whether this syn-depositional relief which developed during deposition of Unit 3 could result from differential compaction of the buried early syn-rift strata of the Lapa Formation across the pre-existing rift fault bounding the Picún Leufú fault-block low. At this location, the Lapa Formation comprises a thick volcano-sedimentary succession, based on the thickness change recorded towards the north-east from the Puesto Alfaro (up to 200 m thick) to the Piletas section (up to 500 to 600 m thick) (cf. Franzese *et al.*, 2006). The compaction of a thicker syn-rift succession in the Picún Leufú fault-block low would result in a larger compaction-induced accommodation in this location (cf. Carminati & Santantonio, 2005). This difference in accommodation explains the accumulation of a thicker mudstone succession (120 m thick) than the stratigraphically equivalent and thinner succession (20 m thick) in the Puesto Alfaro and El Luchador fault-block highs. Changes in both lithology and thickness of the syn-rift succession (Lapa Formation), recorded from the Puesto Alfaro fault-block high to the Piletas fault-block low (see fig. 5 in Franzese *et al.*, 2006), might have enhanced the differential compaction and subsidence in the Picún Leufú fault-block low.

Although detailed backstripping of the entire syn-rift to post-rift succession is not possible in this study, based on the lack of constraints on a number of parameters and limitations of 3D exposure (see the *Data and methodology*

section), it is possible to provide an estimate of compaction. This in turn supports the postulated role of differential compaction in explaining early post-rift subsidence patterns. In the Picún Leufú fault-block low, it is difficult to quantify the exact thickness of the Lapa Formation because whilst the upper part is exposed, the lower part is lying in the subsurface as it dips and thickens towards the north-east, and is better exposed 2 km northward in the Piletas section (up to 500 to 600 m thick; Franzese *et al.*, 2006). The Piletas section is used as an analogue for the Picún Leufú section, and therefore a thickness of 500 m is assumed, including an estimate of the most deeply buried lower half of the Lapa Formation (250 m thick) lying in the subsurface. The Lapa Formation comprises interbedded compactable clastic rocks and less compactable volcanic rocks (mostly matrix-supported breccias and minor conglomerates, sandstone and mudstone; Franzese *et al.*, 2006), which can comprise up to 40% of the total thickness of the syn-rift succession (cf. Franzese *et al.*, 2006). Considering the sandy matrix of breccias and conglomerates, it is assumed that their porosity is commensurate with sandstone which is typically deposited with 40 to 50% porosity that is reduced up to 15 to 25% at *ca* 1 to 2 km of burial depth (cf. Sclater & Christie, 1980; Skuce, 1996). Therefore, lithostatic loading of the upper half of the Lapa Formation and the Chachil Formation (as a total of 280 m thick) could compact up to 20% of the original thickness of the lower half of the Lapa Formation. The original thickness of the lower Lapa Formation at time of deposition (*ca* 313 m thick) means that mechanical compaction would have provided *ca* 63 m of accommodation space in the Picún Leufú fault-block low.

Similarly, the mudstone succession at the base of the Lower Los Molles Formation (Unit 3), could compact up to 40% of its original thickness, as mudstone is deposited with 70 to 80% porosity and undergoes a *ca* 40% porosity loss at *ca* 200 m of burial depth (cf. Shinn & Robbin, 1983; Skuce, 1996). The decompacted thickness of mudstone would have been *ca* 200 m in the Picún Leufú fault-block low and *ca* 100 m on the Puesto Alfaro fault-block high. Therefore, the *ca* 100 m thickening of Unit 3 recorded in the Picún Leufú fault-block low could have filled the accommodation space (*ca* 63 m) generated with mechanical compaction of the lower Lapa and Chachil Formation and healed the inherited fault-scarp relief. This would be

consistent with the thickness (*ca* 20 m) of compacted mudstone of Unit 3 found on the El Luchador and Paine Milla fault-block highs.

The amount of compaction-induced accommodation proposed here is likely underestimated by using conservative compaction rates, as the sandstone compaction rate applied to the Lapa Formation does not account for the higher compaction rate of interlayered mudstone in this mixed succession. The extra accommodation which would have been generated with mechanical compaction of deposits of the Chachil Formation is also neglected. However, these approximations highlight that the thickness changes recorded in the mudstone succession of Unit 3 in the Picún Leufú fault-block low, are in the range of the amount of accommodation that could be created with differential compaction of buried strata across this fault-scarp relief.

Surface deformation, including small-scale faulting and large-scale folding, can result from differential compaction across irregular rigid basement topography and/or arise due to lithological heterogeneity (e.g. Barr, 1991; Skuce, 1996; Cristallini *et al.*, 2006, 2009; Lohr & Underhill, 2015). Compaction-driven surface deformation proceeds over a relatively short timescale (i.e. a few millions of years) and might have outpaced the low sedimentation rate during deposition of Unit 3. This increased the fault scarp relief and the gradient of the hangingwall in the Picún Leufú fault-block low, which exceeded the critical sediment stability threshold (5°) for carbonate muds (cf. Kenter, 1990). Gravitational remobilization and downslope redistribution of fine-grained sediment with slumping occurred, sometimes as metres-scale contorted beds (Fig. 10). Therefore, the presence of this relief is supported by the occurrence of syn-sedimentary destabilization events during deposition of Unit 3, which progressively healed the fault-scarp relief (i.e. 'parallel onlap fill', Cartwright, 1991). As the compaction and surface deformation rate outpaced the very low sediment accumulation rate, the fault-scarp relief increased 'passively', enhanced by differential compaction and subsidence, without the need to invoke active extension and fault slip (e.g. Carminati & Santantonio, 2005).

These observations have implications for the interpretation of the syn-rift to post-rift transition and indicate that the timing of active (i.e. syn-rift) normal faulting in the Lower Los Molles Formation could be erroneously inferred

based on relatively subtle changes in thickness and facies, which instead could be controlled by post-rift differential compaction. Additionally, these results support findings in other locations of the Neuquén Basin (north-east and south-east of the Huincul High), where small-scale normal faulting, stratal wedging and graben-scale folding of Early Jurassic strata around rift structures are similarly related to differential compaction of the buried syn-rift succession (Cristallini *et al.*, 2006, 2009).

#### Unit 4

Unit 4 is characterized by thinning with onlap updip towards the NNW–SSE trending Southern Chachil Graben margin, thickening and dipping towards the east/north-east into the graben. This configuration defines a broad (*ca* 6 km across), NNE-trending, long-wavelength and low-amplitude monocline slightly oblique to the Southern Chachil Graben margin (Figs 1C and 3A). The gentle dip and lack of uplifted hangingwall strata with major thrust deformation in Unit 4 near the Southern Chachil Graben margin suggest that the monocline did not grow in response to compression during basin inversion. Instead, monocline folding could have developed during the early post-rift in response to differential compaction across the Southern Chachil Graben margin and enhanced accommodation in the centre of the graben, as documented in other rift basins (e.g. Barr, 1991; Cartwright, 1991; Skuce, 1996; Monaldi *et al.*, 2008; López-Gamundí & Barragan, 2012; Lohr & Underhill, 2015). Therefore, early post-rift strata record the effects of differential compaction at: (i) a local scale in Unit 3 with the formation of a compaction hinge above a buried rift structure in the graben; and (ii) a larger scale in Unit 4 with the development of a long-wavelength and low-amplitude monocline fold along the Southern Chachil Graben margin (Figs 3A and 10). Constraining the effects of compaction-induced deformation across rift structures is key to estimating the timing of the syn-rift to post-rift transition at depocentre-scale, as well as for predicting early post-rift reservoir distribution with combined stratigraphic and structural traps.

#### Controls on sedimentation during the syn-rift to post-rift transition

The transition from the late syn-rift to early post-rift is marked by a change in stratigraphic architecture, sediment dispersal (i.e. from axial

to transverse to structural strike) and from intrabasinal carbonate to extrabasinal siliciclastic sediment supply. Stratal stacking patterns in the Chachil Graben record a change from general retrogradation to progradation, and from underfilled to sediment-balanced conditions (Figs 2, 13 and 14). The relative importance of rift basin topography, tectonics and climate as key controls on these changes are discussed herein.

#### *Late syn-rift*

Linkage of the Chachil Graben bounding fault system during the rift climax (Franzese *et al.*, 2006), and the presence of acidic volcanic and granitic rocks resistant to weathering along the Southern Chachil Graben margin might have limited the development of local drainage catchments bounding the depocentre during the late syn-rift (Leeder *et al.*, 1998). The relatively low relief inherited from the overfilled depocentre configuration (*sensu* Muravchik *et al.*, 2011) also limited intrabasinal clastic sediment supply and reworking of volcano-sedimentary syn-rift deposits (Lapa Formation). In contrast, steeper gradients preserved in the adjacent Catán-Lil Graben promoted intense fault-block degradation and accumulation of late syn-rift fan deltas (Muravchik *et al.*, 2014).

Growth of normal faults during the late syn-rift segmented the immediate hangingwall of the Southern Chachil Graben margin and induced a structural pattern that differed from the rift climax structural configuration (cf. Franzese *et al.*, 2006). These conditions, together with the temperate climate (cf. Volkheimer *et al.*, 2008) that was characterized by reduced precipitation, erosion, and both intrabasinal and extrabasinal sediment delivery, permitted the late syn-rift development of the carbonate system in the Chachil Graben (Fig. 14). Fault linkage physically disconnected footwall-derived sediment sources from their sink and subsequent marine transgression associated with rapid subsidence suppressed sediment input by reducing the size of the intrabasinal drainage catchments that were flooded. Thus, instead of acting as an efficient clastic intrabasinal source during the late syn-rift and early post-rift, the horst structure which formed the Southern Chachil Graben margin underwent rapid marine flooding and acted as a submerged barrier that limited clastic supply. Fault-block highs controlled the dimensions and morphology of shallow-marine isolated carbonate platforms (Fig. 14). Syn-rift deformation prevented the development of fault-block carbonate

platforms in down-faulted depressions or their coalescence into a larger composite platform, which would have required tectonic quiescence and subdued fault-related relief (Dorobek, 2008). Instead, fault-block lows received proximal periplatform mixed carbonate-clastic deposits reworked from the carbonate platforms on fault-block highs, which were funnelled across the complicated structural rift pattern, mainly axially to the structural strike towards the south-east (Fig. 14). With tectonic subsidence and rising relative sea-level, the carbonate platform supplied greater flux of fine-grained reworked carbonate sediment basinward (e.g. Dorobek, 2008). This resulted in retrogradation of the system and accumulation of distal periplatform mixed carbonate-clastic mud-rich deposits into fault-block lows, whereas condensed sedimentation occurred over carbonate platform deposits on fault-block highs (Fig. 14). The warm-temperate nature of the carbonate system (cf. climate Volkheimer *et al.*, 2008) played a key role in its organization and evolution across rift structures. The low energy setting and lack of early cementation and binding (no framebuilding biota) of these carbonate deposits favoured their reworking into allochemical biodegradable carbonate material towards fault-block lows. Furthermore, their low production rates were insufficient to keep pace with tectonically-driven deepening of water depths, which led to rapid drowning. This might explain why these warm-temperate systems remain poorly documented in rift settings (Gulf of California, Halfar *et al.*, 2004) compared to their tropical counterparts (Gulf of Aden and Suez Rift, Cross & Bosence, 2008). The late syn-rift carbonate sedimentation, and drowning of the system in response to increased rates of fault-controlled subsidence, meant that the Chachil Graben evolved into an underfilled depocentre, which had implications for the subsequent development of the early post-rift system (Fig. 14).

#### *Early post-rift*

During the early post-rift, potential local intrabasinal fault-block sources were rapidly submerged with the back-arc evolution of marine rift depocentres involving high regional subsidence rates related to rapid thermal subsidence effects (cf. Cristallini *et al.*, 2009). Regional marine flooding and mud-draping of inherited rift topography resulted in a very limited to absent intrabasinal sediment supply from degradation of local fault-block highs. Sand starvation

prevailed in marine rift depocentres until the onset of sediment supply from extrabasinal sources along basin margins (Fig. 1A). In contrast to rapid thermal subsidence and regional drowning of fault-blocks, rift basins associated with passive margins often result in an early post-rift configuration where local subaqueous or subaerial degradation of fault-block highs lasts longer due to slow thermal subsidence and provides intrabasinal clastic supply (e.g. Zachariah *et al.*, 2009; Jarsve *et al.*, 2014; Henstra *et al.*, 2016).

In the Chachil Graben, the development of early post-rift lobes with an extrabasinal sediment source is suggested by mud-draping of intrabasinal rift topography, palaeocurrents with respect to rift structures and sandstone composition, which does not match local granitic bedrock on footwall blocks. The early post-rift lobe sandstones are characterized by a high amount of terrestrial organic material (wood, leaves and carbonaceous fragments), the presence of ostreid-bearing clasts found in some of the mud-rich debrites (Fig. 11C) and armoured mudstone clasts (Fig. 11G). These elements support a main provenance from hinterland sources, and shelf to slope sediments (Hodgson, 2009; Migeon *et al.*, 2010; Talling *et al.*, 2010) for the lobe deposits in the Lower Los Molles Formation. An extrabasinal source with high sediment yield would have been required to develop the coarsening-upward intraslope lobe succession that prograded north-eastward into the Chachil Graben. Palaeoflows recorded by early post-rift lobes were mainly transverse to the structural strike of rift fault-blocks, suggesting that most of the former complicated rift topography in the graben was healed with mudstone-dominated and heterolithic-dominated successions (Fig. 5). Therefore, clastic sediment supply, which caused the Chachil Graben to evolve into a sediment-balanced depocentre during the early post-rift, played a major role in infilling the inherited rift topography (Figs 2 and 14). This is consistent with the warm humid climate that prevailed from the early Late Toarcian (cf. Volkheimer *et al.*, 2008) and promoted conditions suitable for high amounts of erosion and riverine runoff, delivering high volumes of sediment towards the basin despite rising sea-level and overall highstand (e.g. Leeder *et al.*, 1998; Yu *et al.*, 2013; Balázs *et al.*, 2017).

During the early post-rift, extrabasinal sediment supply can be trapped by inherited rift topography in proximal depocentres, which are

progressively filled allowing coarse sediment to bypass downslope to more distal depocentres (e.g. Lien, 2005; Soares *et al.*, 2012). At a regional scale, during the early post-rift, the inherited rift topography preserved in the south-western Neuquén Basin (Legarreta & Uliana, 1996; Burgess *et al.*, 2000; Gómez Omil *et al.*, 2002) would have promoted trapping of clastic material along the nascent shelf-slope system located >20 to 25 km south-east of the Chachil Graben, close to the hinterland source (see Fig. 1A). This basin configuration and semi-arid to temperate conditions at the onset of the early post-rift (cf. Fig. 2) might have inhibited the coeval supply of extrabasinal siliciclastic sediment reaching distal depocentres of the southern shelf-slope system. Consequently, deposition of thick organic-rich calcareous mud occurred across the deeply [up to 400 m, cf. Gómez Omil *et al.* (2002), Gómez-Pérez (2003)] submerged inherited rift topography of distal depocentres, such as the Chachil Graben, which remained sand-starved. This promoted the long-lived preservation of major rift basin topography, such as the horst structure which formed the Southern Chachil Graben margin and enhanced local accommodation, with differential compaction and subsidence across buried rift faults into the graben (Fig. 14).

### Implications for the characteristics of intraslope lobes in early post-rift settings

The depositional architecture, facies distribution, termination style and related HEBs of the early post-rift intraslope lobes in the Lower Los Molles Formation (Figs 9, 12 and 14) provide rare insights into the characteristics of these particular deep-water lobes enabling comparison with other basin-floor or base-of-slope lobes (e.g. Houghton *et al.*, 2003; Southern *et al.*, 2017; Dodd *et al.*, 2019).

#### *Relationship between inherited relief and intraslope lobe characteristics*

The architecture of the documented intraslope lobe complex records a stratigraphic change from dirty to cleaner lobe facies, with an increase in grain-size, bed thickness and amalgamation, and sand matrix and clast content, associated with progradation of the intraslope lobe system (Figs 9 and 10). A potential mechanism explaining the stratigraphic change from dirty to cleaner lobes could be the progressive healing of relief obstructing the flow pathway, which would reduce flow interactions with the seabed

topography and limit flow transformation. However, evidence of palaeoflow deflection and reflection, combined-flow and heterolithic bedforms (hummock-like bedforms, and asymmetrical rounded ripples) in both dirty and cleaner lobes support sustained interactions of flows with intrabasinal topography. This relief was likely generated by the compaction hinge, which acted as an oblique counterslope (Fig. 14) for flows and promoted the north-eastward progradation of the intraslope lobe complex.

Hybrid event beds (HEBs) are developed throughout the lobe complex stratigraphy, with lobe complex pinch-outs being dominated by the thin type 2 and 3 HEBs that pinch-out farther basinward than the thicker, type 1 HEBs. Therefore, the presence of frontal topography is interpreted to have prevented systematic segregation of thick HEBs (type 1) towards the fringe of the lobe complex. This pattern of HEB distribution contrasts with documented onlaps in other basins, where the HEBs are only present close to the pinch-out of lobe complex, suggesting that flow transformation occurs near the topography (e.g. Pyles & Jennette, 2009; Patacci *et al.*, 2014).

The sedimentological characteristics and architecture of early post-rift intraslope lobes (Figs 9 and 12) differ from unconfined to weakly confined base-of-slope and basin-floor lobe models. Typically, the latter are larger (>10 km width and length), with more gradual thinning rates and transitions between lobe sub-environments, well-defined lobe off-axes, erosion and scouring restricted to lobe axes, and thinner HEBs (centimetre to decimetre-scale) (Prélat *et al.*, 2009; Prélat & Hodgson, 2013; Spychala *et al.*, 2017). The early post-rift intraslope lobe complex in the Chachil Graben has a low aspect ratio (*ca* 5 km minimum wide  $\times$  6–8 km long  $\times$  50–70 m thick) and well-defined pinch-out terminations similar to previously documented intraslope lobes (6–10 km wide  $\times$  15–25 km long  $\times$  10–15 m thick, Spychala *et al.*, 2015; 8 km wide  $\times$  8 km long  $\times$  120 m thick, Jobe *et al.*, 2017). The documented lobes show scouring and lobe-scale compensation patterns, which are also reported in confined intraslope lobes characterized by sub-seismic-scale heterogeneity (cf. Jobe *et al.*, 2017). However, they are significantly coarser-grained and more argillaceous, with HEB-rich lobe fringes that contrast with sandier fringes of other intraslope lobes, which are HEB-poor (Spychala

*et al.*, 2015; Jobe *et al.*, 2017). The characteristics of the documented lobes in the Los Molles Formation which could be representative of early post-rift intraslope lobes that developed on mud-draped seabed topography are: abrupt transitions between lobe sub-environments (<100 m), widespread erosion including in the lobe fringe, HEBs in axial and fringe sub-environments of dirty and cleaner lobes, and combined-flow and heterolithic bedforms (Figs 9 and 12).

#### *Hybrid event bed type origin*

The poorly sorted, relatively coarse-grained and matrix-rich beds in the intraslope lobes implies deposition from flows that transported coarse-grained material with a high clay and silt component, which reduced the settling velocity of large grains (cf. Al-Ja'aidi *et al.*, 2004). The heterogeneity recorded in the dirty lobes, which mark the first stage of development of the intraslope lobe complex, is characterized by an abundance of relatively thin HEBs (types 2 and 3) with similar thicknesses of facies divisions (Fig. 12). Their deposition may result from autogenic processes (Spychala *et al.*, 2017) with flow transformation through entrainment of the widespread muddy substrate after an extended period of sand-starvation, which increased flow cohesion, and enhanced flow stratification and collapse (Baas *et al.*, 2011; Kane *et al.*, 2017). In contrast, thicker HEBs (type 1) containing a well-developed debritic division encased by sandy divisions (Fig. 12) are common both in the dirty and cleaner lobes, and comprise large clasts of various lithologies that record substrate erosion. The sporadic distribution of these HEBs, which results from flow transformation with shear mixing at top and base of voluminous, long run-out debris-flows transporting shallow-marine bioclasts, seems to be the product of larger flows sourced from mass-wasting processes in a proximal shelf-slope setting (e.g. Hodgson, 2009; Migeon *et al.*, 2010; Talling *et al.*, 2010).

Despite both allogenic and autogenic controls on the type of HEBs, the stratigraphic decrease of intraslope-scale heterogeneity could reflect common HEB development during periods of initiation and growth of out-of-grade systems (Haughton *et al.*, 2003; Hodgson, 2009). Therefore, the reduction of thin HEBs (types 2 and 3) in the thicker-bedded and coarser-grained cleaner lobes (Figs 9 and 14) could be associated with progradation of the intraslope lobe system

and maturation of sediment routing pathways, which together reduced the entrainment of muddy substrate across topography.

The distinctive characteristics of intraslope lobes developed in the Lower Los Molles Formation shows that more investigations of outcrop and subsurface analogues are required to develop models for the architecture and evolution of intraslope lobes encountered in early post-rift settings.

## CONCLUSIONS

This study advances understanding of the organization of sedimentary systems with physiographic transformation of rift topography, change in sedimentation regime, and sediment routing and supply during the syn-rift to post-rift transition in the Chachil Graben. The late syn-rift evolution of the Chachil Graben as an underfilled depocentre, with intrabasinal carbonate sedimentation and mainly axial sediment routing, was controlled by differential tectonic subsidence and rapid deepening, which led to subsequent retrogradation and drowning of the carbonate system. Later draping of the inherited rift topography by organic-rich calcareous mud inhibited intrabasinal sediment supply sources and recorded onset of the early post-rift with local and small-scale deformation associated with differential compaction and subsidence. Abrupt increases in extrabasinal clastic supply enabled the healing of the former rift topography and evolution of the Chachil Graben into a sediment-balanced depocentre, with the progradation of an intraslope lobe complex mainly transverse to buried rift structures. This study highlights the influence of an early post-rift compaction hinge formed across a rift fault in the graben, on local thickness changes within organic-rich mudstone at the base of the Lower Los Molles Formation and on sedimentological characteristics and architecture of intraslope lobes. The intraslope lobe complex (*ca* 5 km minimum wide  $\times$  6–8 km long  $\times$  50–70 m thick) is associated with a kilometre-scale sill-dominated clastic injectite network that steps towards the compaction hinge. The intraslope lobe complex records a stratigraphic evolution from dirty to cleaner lobes, with a decrease of intralobe bed-scale heterogeneity related to the distribution of hybrid event beds (HEBs). As the system prograded north-eastward, the compaction hinge acted as an oblique counterslope

which induced partial confinement and interacted with a range of sediment gravity flows. This resulted in the development of combined-flow and heterolithic bedforms, widespread erosion, scouring and HEB distribution in both axis and fringe sub-environments of dirty and cleaner lobes, with rapid lateral transitions of lobe sub-environments, and HEB-rich pinch-out style of the intraslope complex.

These results support the need to better constrain the effects of differential compaction across rift structures, which can be misinterpreted as originating from active tectonics, in order to estimate the timing of the syn-rift to post-rift transition at depocentre-scale. The documented intraslope lobe complex shows the risk for reservoir deterioration (i.e. HEB-induced lobe heterogeneity) and post-burial remobilization (i.e. injectite complex), which have implications for the prediction of reservoir distribution in combined stratigraphic and structural traps.

## ACKNOWLEDGEMENTS

This study is a collaboration between the University of Leeds (UK), Imperial College London (UK) and CIG-University of La Plata (Argentina). This research is part of the of the Lobe2 Joint Industry Project funded by Equinor, Maersk Oil, Woodside, Total, Neptune Energy, Petrobras, Shell, Anadarko, BP, Chevron, Bayern Gas, VNG Norge, BHP Billiton, DONG Energy, Marathon Oil and Premier Oil. The authors warmly thank Louis Thoreau and Andy Emery for their precious field assistance in the Chachil area and efforts to collect the best data, even under the worst Patagonian weather conditions or the pressure of serious circumstances. The authors thank Munoz Anibal for land access, Dania Pascua (Geological Service and Provincial Mining of Zapala) for providing logistical support, field information, SRTM files and access to document consultation. Gabriel Rouret our lawyer from the official public defence of Zapala and Jérôme Sassiati from the Consul General of France in Argentina are thanked for their help and support. We are very grateful to Marcos and Carlos Retamal, Valeria Zilberman and Patricia Alvarez for their continuous help and invaluable support during the field seasons. We thank Ander Martinez-Doñate for advice on an early version of the

paper, which helped to improve Fig. 10. Associate Editor Jim Hendry, Telm Bover Arnal and an anonymous reviewer are thanked for their detailed and constructive reviews that significantly improved the paper. We also thank Editor Peir Pufahl.

## CONFLICT OF INTEREST

The authors declare no conflict of interest for this previously unpublished work.

## DATA AVAILABILITY STATEMENT

The data that support the findings of this study are available from the corresponding author.

## REFERENCES

- Aller, R.C. (1982) Carbonate dissolution in nearshore terrigenous muds: the role of physical and biological reworking. *J. Geol.*, **90**, 79–95.
- Al Ja'Aidi, O.S., McCaffrey, W.D. and Kneller, B.C. (2004) Factors influencing the deposit geometry of experimental turbidity currents: implications for sand-body architecture in confined basins. In: *Confined Turbidite Systems* (Eds Lomas, S.A. and Joseph, P.), *Geological Society, London, Special Publications*, **222**, 45–58.
- Al-Suwaidi, A.H., Hesselbo, S.P., Damborenea, S.E., Manceñido, M.O., Jenkyns, H.C., Riccardi, A.C., Angelozzi, G.N. and Baudin, F. (2016) The Toarcian Oceanic Anoxic Event (Early Jurassic) in the Neuquén Basin, Argentina: A reassessment of age and carbon isotope stratigraphy. *J. Geol.*, **124**, 171–193.
- Amy, L.A., McCaffrey, W.D. and Kneller, B.C. (2004) The influence of a lateral basin-slope on the depositional patterns of natural and experimental turbidity currents. In: *Deep-Water Sedimentation in the Alpine Basin of SE France. New perspectives on the Grès d'Annot and related systems* (Eds Joseph, P. and Lomas, S.A.), *Geological Society, London, Special Publications*, **221**, 311–330.
- Amy, L.A., Peakall, J. and Talling, P.J. (2005) Density- and viscosity-stratified gravity currents: Insight from laboratory experiments and implications for submarine flow deposits. *Sedimentary Geology*, **179**, 5–29.
- Angelozzi, G.N. and Pérez Panera, J.P. (2016) Calcareous nanofossils from Los Molles Formation (Pliensbachian-Aalenian), Neuquén Basin, Argentina. In: *Jurassic Calcareous Nanofossil Workshop, Lyon*, 6–11.
- Argent, J.D., Stewart, S.A. and Underhill, J.R. (2000) Controls on the Lower Cretaceous Punt Sandstone Member, a massive deep-water clastic deposystem, Inner Moray Firth, UK North Sea. *Petroleum Geoscience*, **6**, 275–285.
- Armella, C., Leanza, H.A. and Corfu, F. (2016) Synsedimentary ash rains and paleoenvironmental conditions during the deposition of the Chachil Formation (Pliensbachian) at its type locality, Neuquén Basin, Argentina. *Journal of South American Earth Sciences*, **71**, 82–95.
- Baas, J.H., Best, J.L., Peakall, J. and Wang, M. (2009) A phase diagram for turbulent, transitional, and laminar clay suspension flows. *Journal of Sedimentary Research*, **79**, 162–183.
- Baas, J.H., Best, J.L. and Peakall, J. (2011) Depositional processes, bedform development and hybrid flows in rapidly decelerated cohesive (mud-sand) sediment flows. *Sedimentology*, **58**, 1953–1987.
- Baas, J.H., Best, J.L. and Peakall, J. (2016) Predicting bedforms and primary current stratification in cohesive mixtures of mud and sand. *Journal of the Geological Society*, **173**, 12–45.
- Baker, M.L. and Baas, J.H. (2020) Mixed sand-mud bedforms produced by transient turbulent flows in the fringe of submarine fans: Indicators of flow transformation. *Sedimentology*, **67**, 2645–2671. <https://doi.org/10.1111/sed.12714>.
- Balázs, A., Granjeon, D., Matenco, L., Sztanó, O. and Cloetingh, S. (2017) Tectonic and climatic controls on asymmetric half-graben sedimentation: Inferences from 3-D numerical modeling. *Tectonics*, **36**, 2123–2141.
- Ballent, S., Concheyro, A., Nández, C., Pujana, I., Lescano, M., Carignano, A.P., Caramés, A., Angelozzi, G. and Ronchi, D. (2011) Microfósiles Mesozoicos Y Cenozoicos. In: *Geología y Recursos Naturales de la Provincia del Neuquén, XVIII Congreso Geológico Argentino, Buenos Aires* (Eds Leanza, H.A., Arregui, C., Carbone, O., Danieli, J.C. and Vallés, J.M.), *Asociación Geológica Argentina*, 489–528.
- Barr, D. (1991) Subsidence and sedimentation in semi-starved half-graben: a model based on North Sea data. In: *The Geometry of Normal Faults* (Eds Roberts, A.M., Yielding, G. and Freeman, B.), *Geological Society, London, Special Publications*, **56**, 17–28.
- Best, J. and Bridge, J. (1992) The morphology and dynamics of low amplitude bedwaves upon upper stage plane beds and the preservation of planar laminae. *Sedimentology*, **39**, 737–752.
- Betzler, C., Brachert, T.C. and Nebelsick, J. (1997) The warm temperate carbonate province – a review of the facies, zonations, and delimitations. *Cour. Forsch. Inst. Senckenberg.*, **201**, 83–99.
- Birgenheier, L.P. and Moore, S.A. (2018) Carbonate mud deposited below storm wave base: a critical review. *Sed. Rec.*, **16**, 4–10.
- Boehm, A. and Moore, J.C. (2002) Fluidized sandstone intrusions as an indicator of paleostress orientation, Santa Cruz, California. *Geofluids*, **2**, 147–161.
- Bosence, D. (2005) A genetic classification of carbonate platforms based on their basinal and tectonic settings in the Cenozoic. *Sed. Geol.*, **175**, 49–72.
- Bouma, A.H. (1962) *Sedimentology of Some Flysch Deposits: A Graphic Approach to Facies Interpretation*. Elsevier, Amsterdam/New York, 168 pp.
- Braga, J.C., Martin, J.M. and Wood, J.L. (2001) Submarine lobes and feeder channels of redeposited, temperate carbonate and mixed siliciclastic-carbonate platform deposits (Vera Basin, Almería, southern Spain). *Sedimentology*, **48**, 99–116.
- Burgess, P.M., Flint, S. and Johnson, S. (2000) Sequence stratigraphic interpretation of turbiditic strata: An example from Jurassic strata of the Neuquén basin, Argentina. *Geol. Soc. Am. Bull.*, **112**, 1650–1666.

- Carminati, E.** and **Santantonio, M.** (2005) Control of differential compaction on the geometry of sediments onlapping paleoescarpments: insights from field geology (Central Apennines, Italy) and numerical modeling. *Geology*, **33**, 353–356.
- Cartwright, J.** (1991) The kinematic evolution of the Coffee Soil Fault. In: *The Geometry of Normal Faults* (Eds Roberts, A.M., Yielding, G. and Freeman, B.), *Geological Society, London, Special Publications*, **56**, 29–40.
- Cobain, S.L., Peakall, J.** and **Hodgson, D.M.** (2015) Indicators of propagation direction and relative depth in clastic injectites: implications for laminar versus turbulent flow processes. *Geological Society of America Bulletin*, **127**, 1816–1830.
- Cobain, S.L., Hodgson, D.M., Peakall, J.** and **Shiers, M.N.** (2017) An integrated model of clastic injectites and basin floor lobe complexes: implications for stratigraphic trap plays. *Basin Research*, **29**, 816–835.
- Crabough, J.P.** and **Steel, R.J.** (2004) Basin-floor fans of the Central Tertiary Basin, Spitsbergen: relationship of basin-floor sand-bodies to prograding clinoforms in a structurally active basin. In: *Confined Turbidite Systems* (Eds Lomas, S.A. and Joseph, P.), *Geological Society, London, Special Publications*, **222**, 187–208.
- Cristallini, E.O., Bottesi, G., Gavarrino, A., Rodríguez, L., Tomezzoli, R.** and **Cameron, R.** (2006) Synrift geometry of the Neuquén Basin in northeastern Neuquén Province, Argentina. In: *Evolution of the Andean margin: a tectonic and magmatic view from the Andes to the Neuquén Basin (35°–39°S lat)* (Eds Kay, S.M. and Ramos, V.A.), *Geological Society of America Special Paper*, **407**, 147–161.
- Cristallini, E., Tomezzoli, R., Pando, G., Gazzera, C., Martínez, J.M., Quiroga, J., Buhler, M., Bechis, F., Barredo, S.** and **Zambrano, O.** (2009) Controles precuianos en la estructura de la Cuenca Neuquina. *Rev. Asoc. Geol. Argentina*, **65**, 248–264.
- Cross, N.E.** and **Bosence, D.W.J.** (2008) Tectono-sedimentary models for rift-basin carbonate systems. In: *Controls on Carbonate Platform and Reef Development* (Eds Lukasik, J. and Simo, J.A.T.), *SEPM (Society for Sedimentary Geology)*, **89**, 83–105.
- Dakin, N., Pickering, K.T., Mohrig, D.** and **Bayliss, N.J.** (2013) Channel-like features created by erosive submarine debris flows: field evidence from the Middle Eocene Ainsa Basin, Spanish Pyrenees. *Mar. Petrol. Geol.*, **41**, 62–71.
- Damborenea, S.E.** and **Manceñido, M.O.** (1979) On the palaeogeographical distribution of the pectinid genus *Weyla* (Bivalvia, Lower Jurassic). *Palaeogeogr. Palaeoclimatol. Palaeoecol.*, **27**, 85–102.
- Damborenea, S.E.** and **Manceñido, M.O.** (1992) A comparison of Jurassic marine benthonic faunas from South America and New Zealand. *J. Roy. Soc. NZ*, **22**, 131–152.
- Damborenea, S.E., Echevarría, J.** and **Ros-Franch, S.** (2013) *Southern Hemisphere Palaeobiogeography of Triassic–Jurassic Marine Bivalves*. Springer, Netherlands, 139 pp.
- D’Atri, A., Dela Pierre, F., Lanza, R.** and **Ruffini, R.** (1999) Distinguishing primary and re-sedimented vitric volcanoclastic layers in the Burdigalian carbonate shelf deposits in Monferrato (NW Italy). *Sed. Geol.*, **129**, 143–163.
- D’Elia, L., Bilmes, A., Franzese, J.R., Veiga, G.D., Hernández, M.** and **Muravchik, M.** (2015) Early evolution of the southern margin of the Neuquén Basin, Argentina: Tectono-stratigraphic implications for rift evolution and exploration of hydrocarbon plays. *Journal of South American Earth Sciences*, **64**, 42–57.
- Dera, G.** and **Donnadieu, Y.** (2012) Modeling evidences for global warming, Arctic seawater freshening, and sluggish oceanic circulation during the Early Toarcian anoxic event. *Paleoceanography*, **27**, PA2211.
- Dodd, T.J.H., McCarthy, D.J.** and **Richards, P.C.** (2019) A depositional model for deep-lacustrine, partially confined, turbidite fans: Early Cretaceous, North Falkland Basin. *Sedimentology*, **66**, 53–80.
- Dorobek, S.L.** (2008) Tectonic and depositional controls on syn-rift carbonate platform sedimentation. In: *Controls on Carbonate Platform and Reef Development* (Eds Lukasik, J. and Simo, J.A.T.), *SEPM Special Publication*, **89**, 57–81.
- Drzewiecki, P.A.** and **Simó, J.A.** (2002) Depositional processes, triggering mechanisms and sediment composition of carbonate gravity flow deposits: examples from the Late Cretaceous of the south-central Pyrenees, Spain. *Sed. Geol.*, **146**, 155–189.
- Ekdale, A.A.** and **Mason, T.R.** (1988) Characteristic trace-fossil associations in oxygen-poor sedimentary environments. *Geology*, **16**, 720–723.
- Ekdale, A.A.** and **Harding, S.C.** (2015) *Cylindrichnus concentricus* Toots in Howard, 1966 (trace fossil) in its type locality, Upper Cretaceous, Wyoming. *Ann. Soc. Geol. Pol.*, **85**, 427–432.
- Etienne, S., Mulder, T., Bez, M., Desaubiaux, G., Kwasiński, A., Parize, O., Dujoncquoy, E.** and **Salles, T.** (2012) Multiple scale characterization of sand-rich distal lobe deposit variability: examples from the Annot Sandstones Formation, Eocene-Oligocene, SE France. *Sed. Geol.*, **273–274**, 1–18.
- Fantasia, A., Föllmi, K.B., Adatte, T., Bernárdez, E., Spangenberg, J.E.** and **Mattioli, E.** (2018) The Toarcian Oceanic Anoxic Event in southwestern Gondwana: an example from the Andean Basin, northern Chile. *J. Geol. Soc.*, **175**, 883–902.
- Felix, M., Leszczyński, S., Ślaczka, A., Uchman, A., Amy, L.** and **Peakall, J.** (2009) Field expressions of the transformation of debris flows into turbidity currents, with examples from the Polish Carpathians and the French Maritime Alps. *Mar. Petrol. Geol.*, **26**, 2011–2020.
- Flügel, E.** (2004) *Microfacies of Carbonate Rocks, Analysis, Interpretation and Application*. Springer, Berlin, 976 pp.
- Franzese, J.R.** (1995) El Complejo Piedra Santa (Neuquén, Argentina): parte de un cinturón metamórfico neopaleozoico del Gondwana suroccidental. *Rev. Geol. Chile*, **22**, 193–202.
- Franzese, J.R.** and **Spalletti, L.A.** (2001) Late Triassic–early Jurassic continental extension in southwestern Gondwana: tectonic segmentation and pre-break-up rifting. *J. S. Am. Earth Sci.*, **14**, 257–270.
- Franzese, J.R., Veiga, G.D., Schwarz, E.** and **Gómez-Pérez, I.** (2006) Tectonostratigraphic evolution of a Mesozoic graben border system: the Chachil depocentre, southern Neuquén Basin, Argentina. *J. Geol. Soc. London*, **163**, 707–721.
- García Morabito, E., Götze, H.-J.** and **Ramos, V.A.** (2011) Tertiary tectonics of the Patagonian Andes retro-arc area between 38°15′ and 40°S latitude. *Tectonophysics*, **499**, 1–21.
- Gómez Omil, R., Schmithalter, J., Cangini, A., Albariño, L.** and **Corsi, A.** (2002) El Grupo Cuyo en la Dorsal de Huincul, consideraciones estratigráficas, tectónicas y petroleras. Cuenca Neuquina. In: *Rocas Reservorio de las Cuencas Productivas de la Argentina, V Congreso de Exploración y Desarrollo de Hidrocarburos, Mar del Plata* (Eds Schiuma,

- M., Hinterwimmer, G. and Vergani, G.), IAPG (Instituto Argentino de Petróleo y Gas), Actas-CD-ROM, 22 pp.
- Gómez-Pérez, I.** (2003) An Early Jurassic deep-water stromatolitic bioherm related to possible methane seepage (Los Molles Formation, Neuquén, Argentina). *Palaeogeogr. Palaeoclimatol. Palaeoecol.*, **201**, 21–49.
- Gulisano, C.A. and Gutiérrez Pleimling, A.R.** (1995) Field Guide. The Jurassic of the Neuquén Basin. a) Neuquén Province. *Secretaría de Minería de la Nación y Asociación Geológica Argentina*, Serie E, **2**, 111 pp.
- Gulisano, C.A., Gutiérrez Pleimling, A.R. and Digregorio, J.H.** (1984) Esquema estratigráfico de la secuencia jurásica del oeste de la provincia del Neuquén. In: *IX Congreso Geológico Argentino, San Carlos de Bariloche* (Eds Ramos, V.A.), Asociación Geológica Argentina, 236–259.
- Hadlari, T., Midwinter, D., Galloway, J.M., Dewing, K. and Durbano, A.M.** (2016) Mesozoic rift to post-rift tectonostratigraphy of the Sverdrup Basin, Canadian Arctic. *Mar. Petrol. Geol.*, **76**, 148–158.
- Halfar, J., Ingle, J.C.J. and Godinez-Orta, L.** (2004) Modern non-tropical mixed carbonate-siliciclastic sediments and environments of the southwestern Gulf of California, Mexico. *Sed. Geol.*, **165**, 93–115.
- Haq, B.U.** (2018) Jurassic sea-level variations: a reappraisal. *GSA Today*, **28**, 4–10.
- Houghton, P.D.W., Barker, S.P. and McCaffrey, W.D.** (2003) ‘Linked’ debrites in sand-rich turbidite systems – origin and significance. *Sedimentology*, **50**, 459–482.
- Houghton, P., Davis, C., McCaffrey, W. and Barker, S.** (2009) Hybrid sediment gravity flow deposits – Classification, origin and significance. *Mar. Petrol. Geol.*, **26**, 1900–1918.
- Henstra, G.A., Grundvåg, S.-A., Johannessen, E.P., Kristensen, T.B., Midtkandal, I., Nystuen, J.P., Rotevatn, A., Surlyk, F., Sæther, T. and Windelstad, J.** (2016) Depositional processes and stratigraphic architecture within a coarse-grained rift-margin turbidite system: The Wollaston Forland Group, east Greenland. *Mar. Petrol. Geol.*, **76**, 187–209.
- Hodgson, D.M.** (2009) Distribution and origin of hybrid beds in sand-rich submarine fans of the Tanqua depocentre, Karoo Basin, South Africa. *Mar. Petrol. Geol.*, **26**, 1940–1956.
- Hofstra, M., Peakall, J., Hodgson, D.M. and Stevenson, C.J.** (2018) Architecture and morphodynamics of subcritical sediment waves in an ancient channel-lobe transition zone. *Sedimentology*, **65**, 2339–2367.
- Howell, J.A., Schwarz, E., Spalletti, L.A. and Veiga, G.D.** (2005) The Neuquén Basin: an overview. In: *The Neuquén Basin, Argentina: A Case Study in Sequence Stratigraphy and Basin Dynamics* (Eds Veiga, G.D., Spalletti, L.A., Howell, J.A. and Schwarz, E.), Geological Society, London, *Special Publications*, **252**, 1–14.
- Hurst, A., Scott, A. and Vigorito, M.** (2011) Physical characteristics of sand injectites. *Earth-Sci. Rev.*, **106**, 215–246.
- Jarsve, E.M., Faleide, J.I., Gabrielsen, R.H. and Nystuen, J.P.** (2014) Mesozoic and Cenozoic basin configurations in the North Sea. In: *From Depositional Systems to Sedimentary Successions on the Norwegian Continental Margin* (Eds Martinius, A.W., Ravnås, R., Howell, J.A., Steel, R.J. and Wonham, J.P.), **46**, pp. 417–452. John Wiley & Sons, Ltd, Chichester.
- Jobe, Z.R., Sylvester, Z., Howes, N., Pirmez, C., Parker, A., Cantelli, A., Smith, R., Wolinsky, M.A., O’Byrne, C., Slowey, N. and Prather, B.** (2017) High-resolution, millennial-scale patterns of bed compensation on a sand-rich intraslope submarine fan, western Niger Delta slope. *Geol. Soc. Am. Bull.*, **129**, 23–37.
- Kane, I.A.** (2010) Development and flow structures of sand injectites: The Hind Sandstone Member injectite complex, Carboniferous, UK. *Mar. Petrol. Geol.*, **27**, 1200–1215.
- Kane, I.A., Pontén, A.S.M., Vangdal, B., Eggenhuisen, J.T., Hodgson, D.M. and Spychala, Y.T.** (2017) The stratigraphic record and processes of turbidity current transformation across deep-marine lobes. *Sedimentology*, **64**, 1236–1273.
- Kenter, J.A.M.** (1990) Carbonate platform flanks: slope angle and sediment fabric. *Sedimentology*, **37**, 777–794.
- Kneller, B.C. and Branney, M.J.** (1995) Sustained high-density turbidity currents and the deposition of thick massive sands. *Sedimentology*, **42**, 607–616.
- Kneller, B., Edwards, D., McCaffrey, W. and Moore, R.** (1991) Oblique reflection of turbidity currents. *Geology*, **19**, 250–252.
- Kyrkjebø, R., Gabrielsen, R.H. and Faleide, J.I.** (2004) Unconformities related to the Jurassic-Cretaceous synrift-post-rift transition of the northern North Sea. *J. Geol. Soc. London*, **161**, 1–17.
- Leanza, H.A.** (1990) Estratigrafía del Paleozoico y Mesozoico anterior a los movimientos intermalcóicos en la comarca del cerro Chachil, provincia del Neuquén. *Rev. Asoc. Geol. Argentina*, **45**, 272–299.
- Leanza, H.A., Mazzini, A., Corfu, F., Llambías, E.J., Svensen, H., Planke, S. and Galland, O.** (2013) The Chachil Limestone (Pliensbachian–earliest Toarcian) Neuquén Basin, Argentina: U-Pb age calibration and its significance on the Early Jurassic evolution of southwestern Gondwana. *J. S. Am. Earth Sci.*, **42**, 171–185.
- Leeder, M.R., Harris, T. and Kirkby, M.J.** (1998) Sediment supply and climate change: implications for basin stratigraphy. *Basin Research*, **10**, 7–18.
- Legarreta, L. and Uliana, M.A.** (1996) The Jurassic succession in west-central Argentina: stratal patterns, sequences and paleogeographic evolution. *Palaeogeogr., Palaeoclimatol., Palaeoecol.*, **120**, 303–330.
- Lien, T.** (2005) From rifting to drifting: effects on the development of deep-water hydrocarbon reservoirs in a passive margin setting, Norwegian Sea. *Norw. J. Geol.*, **85**, 319–332.
- Llambías, E.J., Quenardelle, S. and Montenegro, T.** (2003) The Choiyoi Group from central Argentina: a subalkaline transitional to alkaline association in the craton adjacent to the active margin of the Gondwana continent. *J. S. Am. Earth Sci.*, **16**, 243–257.
- Lohr, T. and Underhill, J.R.** (2015) Role of rift transection and punctuated subsidence in the development of the North Falkland Basin. *Petrol. Geosci.*, **21**, 85–110.
- López-Gamundi, O. and Barragan, R.** (2012) Structural framework of Lower Cretaceous half grabens in the presalt section of the southeastern continental margin of Brazil. In: *Tectonics and Sedimentation: Implications for Petroleum Systems* (Ed. Gao, D.), American Association of Petroleum Geologists Memoir, **100**, 143–158.
- Lowe, D.R.** (1982) Sediment gravity flows; II, Depositional models with special reference to the deposits of high-density turbidity currents. *J. Sed. Petrol.*, **52**, 279–297.
- Macdonald, H.A., Peakall, J., Wignall, P.B. and Best, J.** (2011) Sedimentation in deep-sea lobe-elements: implications for the origin of thickening-upward sequences. *J. Geol. Soc.*, **168**, 319–332.

- Marr, J.G., Harff, P.A., Shanmugam, G. and Parker, G. (2001) Experiments on subaqueous sandy gravity flows: the role of clay and water content in flow dynamics and depositional structures. *Geol. Soc. Am. Bull.*, **113**, 1377–1386.
- Martinsen, O.J., Lien, T. and Jackson, C. (2005) Cretaceous and Palaeogene turbidite systems in the North Sea and Norwegian Sea Basins: source, staging area and basin physiography controls on reservoir development. *Geol. Soc. London Petrol. Geol. Conference Ser.*, **6**, 1147–1164.
- McArthur, A.D., Hartley, A.J. and Jolley, D.W. (2013) Stratigraphic development of an Upper Jurassic deep marine syn-rift succession, Inner Moray Firth Basin, Scotland. *Basin Research*, **25**, 285–309.
- McKenzie, D.P. (1978) Some remarks on the development of sedimentary basins. *Earth Planet. Sci. Lett.*, **40**, 25–32.
- Migeon, S., Ducassou, E., Le Gonidec, Y., Rouillard, P., Mascle, J. and Revel-Rolland, M. (2010) Lobe construction and sand/mud segregation by turbidity currents and debris flows on the western Nile deep-sea fan (Eastern Mediterranean). *Sed. Geol.*, **229**, 124–143.
- Milton-Worsell, R.J., Stoker, S.J. and Cavill, J.E. (2006) Lower Cretaceous deep-water sandstone plays in the UK Central Graben. In: *The Deliberate Search for the Stratigraphic Trap* (Eds Allen, M.R., Goffrey, G.P., Morgan, R.K. and Walker, I.M.), *Geological Society, London, Special Publications*, **254**, 169–186.
- Mohrig, D. and Marr, J.G. (2003) Constraining the efficiency of turbidity current generation from submarine debris flows and slides using laboratory experiments. *Mar. Petrol. Geol.*, **20**, 883–899.
- Monaldi, C.R., Salfity, J.A. and Kley, J. (2008) Preserved extensional structures in an inverted Cretaceous rift basin, northwestern Argentina: outcrop examples and implications for fault reactivation. *Tectonics*, **27**, TC1011.
- Morse, J.W., Arvidson, R.S. and Lutge, A. (2007) Calcium carbonate formation and dissolution. *Chemical Reviews*, **107**, 342–381.
- Moscaredelli, L., Ramnarine, S.K., Wood, L. and Dunlap, D.B. (2013) Seismic geomorphological analysis and hydrocarbon potential of the Lower Cretaceous Cromer Knoll Group, Heidrun field, Norway. *AAPG Bull.*, **97**, 1227–1248.
- Mpodozis, C. and Ramos, V. (2008) Tectónica Jurásica en Argentina y Chile: extensión, subducción oblicua, rifting, deriva y colisiones? *Rev. Asoc. Geol. Argentina*, **63**, 481–497.
- Mulder, T. and Alexander, J. (2001) The physical character of subaqueous sedimentary density flows and their deposits. *Sedimentology*, **48**, 269–299.
- Muravchik, M., D'Elia, L., Bilmes, A. and Franzese, J.R. (2011) Syn-eruptive/inter-eruptive relations in the syn-rift deposits of the Precuyano Cycle, Sierra de Chacaico, Neuquén Basin, Argentina. *Sed. Geol.*, **238**, 132–144.
- Muravchik, M., Bilmes, A., D'Elia, L. and Franzese, J.R. (2014) Alluvial fan deposition along a rift depocentre border from the Neuquén Basin, Argentina. *Sed. Geol.*, **301**, 70–89.
- Mutti, E. (1977) Distinctive thin-bedded turbidite facies and related depositional environments in the Eocene Hecho Group (South-central Pyrenees, Spain). *Sedimentology*, **24**, 107–131.
- Navarro, V., Ruiz-Ortiz, P.A. and Molina, J.M. (2012) Birth and demise of a Middle Jurassic isolated shallow-marine carbonate platform on a tilted fault block: example from the Southern Iberian continental palaeomargin. *Sed. Geol.*, **269–270**, 37–57.
- Ogg, J.G., Ogg, G. and Gradstein, F.M. (2016) Jurassic. In: *A concise Geologic Time Scale* (Eds Ogg, J.G., Ogg, G. and Gradstein, F.M.), pp. 151–166. Elsevier, Amsterdam.
- Pángaro, F., Pereira, M., Raggio, F., Pioli, O., Silvestro, J.L., Zubiri, M. and Gozálvez, G. (2006) Tectonic inversion of the Huincul High, Neuquén Basin, Argentina: An endangered species. Stratigraphic evidences of its disappearance. 9th Simposio Bolivariano Exploración Petrolera en las Cuenclas Subandinas, cp-111-00042.
- Pángaro, F., Pereira, D.M. and Micucci, E. (2009) El sinrift de la dorsal de Huincul, Cuenca Neuquina: evolución y control sobre la estratigrafía y estructura del área. *Rev. Asoc. Geol. Argentina*, **65**, 265–277.
- Patacci, M., Haughton, P.D.W. and McCaffrey, W.D. (2014) Rheological complexity in sediment gravity flows forced to decelerate against a confining slope, Braux, SE France. *J. Sed. Res.*, **84**, 270–277.
- Payros, A. and Pujalte, V. (2008) Calciclastic submarine fans: an integrated overview. *Earth-Sci. Rev.*, **86**, 203–246.
- Peakall, J., Best, J.L., Baas, J., Hodgson, D.M., Clare, M.A., Talling, P.J., Dorrell, R.M. and Lee, D.R. (2020) An integrated process-based model of flutes and tool marks in deep-water environments: Implications for palaeohydraulics, the Bouma sequence and hybrid event beds. *Sedimentology*, **67**, 1601–1666.
- Pérez-López, A. and Pérez-Valera, F. (2012) Tempestite facies models for the epicontinental Triassic carbonates of the Betic Cordillera (southern Spain). *Sedimentology*, **59**, 646–678.
- Prélat, A. and Hodgson, D.M. (2013) The full range of turbidite bed thickness patterns in submarine lobes: controls and implications. *J. Geol. Soc. London*, **170**, 209–214.
- Prélat, A., Hodgson, D.M. and Flint, S.S. (2009) Evolution, architecture and hierarchy of distributary deep-water deposits: a high-resolution outcrop investigation from the Permian Karoo Basin, South Africa. *Sedimentology*, **56**, 2132–2154.
- Privat, A.M.-L.J. (2019) Sedimentology and tectono-stratigraphic development of the syn- to post-rift transition in Southern Neuquén Basin (Argentina) and controls on early post-rift submarine lobes of the Los Molles Formation. PhD thesis, University of Leeds, Leeds, 517 pp.
- Pyles, D.R. and Jennette, D.C. (2009) Geometry and architectural associations of co-genetic debrite-turbidite beds in basin-margin strata, Carboniferous Ross Sandstone (Ireland): Applications to reservoirs located on the margins of structurally confined submarine fans. *Mar. Petrol. Geol.*, **26**, 1974–1996.
- Ravnås, R. and Steel, R.J. (1998) Architecture of marine rift-basin successions. *AAPG Bull.*, **82**, 110–146.
- Riccardi, A.C. (2008) El Jurásico de la Argentina y sus amonites. *Rev. Asoc. Geol. Argentina*. Simposio Jurásico de América del Sur, **63**, 625–643.
- Riccardi, A.C., Damborenea, S.E., Manceñido, M.O. and Leanza, H.A. (2011) Megainvertebrados del jurásico y su importancia geobiológica. In: *Geología y Recursos Naturales de la Provincia del Neuquén, Relatorio del XVIII Congreso Geológico Argentino, Buenos Aires* (Eds Leanza, H.A., Arregui, C., Carbone, O., Danieli, J.C. and Vallés, J.M.), Asociación Geológica Argentina, 441–464.
- Ruiz-Ortiz, P.A., Bosence, D.W.J., Rey, J., Nieto, L.M., Castro, J.M. and Molina, J.M. (2004) Tectonic control of

- facies architecture, sequence stratigraphy and drowning of a Liassic carbonate platform (Betic Cordillera, Southern Spain). *Basin Res.*, **16**, 235–257.
- Santantonio, M.** (1994) Pelagic carbonate platforms in the geologic record: their classification, and sedimentary and paleotectonic evolution. *AAPG Bull.*, **78**, 122–141.
- Schieber, J.** (2016) Mud re-distribution in epicontinental basins – Exploring likely processes. *Mar. Petrol. Geol.*, **71**, 119–133.
- Schiuma, M.** and **Llambías, E.J.** (2008) New ages and chemical analysis on lower Jurassic volcanism close to the dorsal de Huincul, Neuquén. *Rev. Asoc. Geol. Argentina*, **63**, 644–652.
- Sclater, J.G.** and **Christie, P.A.F.** (1980) Continental stretching: an explanation of the post-Mid-Cretaceous subsidence of the Central North Sea Basin. *J. Geophys. Res.*, **85**(B7), 3711–3739.
- Shinn, E.A.** and **Robbin, D.M.** (1983) Mechanical and chemical compaction of fine-grained shallow-water limestones. *J. Sed. Petrol.*, **53**, 595–618.
- Skuce, A.G.** (1996) Forward modelling of compaction above normal faults: an example from the Sirte Basin, Libya. In: *Modern Developments in Structural Interpretation, Validation and Modelling* (Eds Buchanan, P.G. and Nieuwland, D.A.), *Geological Society, London, Special Publications*, **99**, 135–146.
- Soares, D.M., Alves, T.M.** and **Terrinha, P.** (2012) The breakup sequence and associated lithospheric breakup surface: Their significance in the context of rifted continental margins (West Iberia and Newfoundland margins, North Atlantic). *Earth Planet. Sci. Lett.*, **355–356**, 311–326.
- Southern, S.J., Kane, I.A., Warchol, M.J., Porten, K.W.** and **McCaffrey, W.D.** (2017) Hybrid event beds dominated by transitional-flow facies: character, distribution and significance in the Maastrichtian Springar Formation, north-west Vøring Basin, Norwegian Sea. *Sedimentology*, **64**, 747–776.
- Spikings, A.L., Hodgson, D.M., Paton, D.A.** and **Spychala, Y.T.** (2015) Palinspastic restoration of an exhumed deep-water system: a workflow to improve paleogeographic reconstructions. *Interpretation*, **3**, SAA71–SAA87.
- Spychala, Y.T., Hodgson, D.M., Flint, S.S.** and **Mountney, N.P.** (2015) Constraining the sedimentology and stratigraphy of submarine intraslope lobe deposits using exhumed examples from the Karoo Basin, South Africa. *Sed. Geol.*, **322**, 67–81.
- Spychala, Y.T., Hodgson, D.M., Prélat, A., Kane, I.A., Flint, S.S.** and **Mountney, N.P.** (2017) Frontal and lateral submarine lobe fringes: Comparing sedimentary facies, architecture and flow processes. *J. Sed. Res.*, **87**, 75–96.
- Stevenson, C.J., Peakall, J., Hodgson, D.M., Bell, D.** and **Privat, A.** (2020)  $T_b$  or not  $T_b$ : Banding in turbidite sandstones. *J. Sed. Res.*, **90**, 821–842.
- Stow, D.** and **Bowen, A.** (1980) A physical model for the transport and sorting of fine-grained sediment by turbidity currents. *Sedimentology*, **27**, 31–46.
- Sumner, E.J., Amy, L.A.** and **Talling, P.J.** (2008) Deposit structure and processes of sand deposition from decelerating sediment suspensions. *J. Sed. Res.*, **78**, 529–547.
- Surlyk, F.** and **Korstgård, J.** (2013) Crestal unconformities on an exposed Jurassic tilted fault block, Wollaston Forland, East Greenland as an analogue for buried hydrocarbon traps. *Mar. Petrol. Geol.*, **44**, 82–95.
- Talling, P.J.** (2013) Hybrid submarine flows comprising turbidity current and cohesive debris flow: deposits, theoretical and experimental analyses, and generalized models. *Geosphere*, **9**, 460–488.
- Talling, P.J., Peakall, J., Sparks, R.S.J., Ó Cofaigh, C.S., Dowdeswell, J.A., Felix, M., Wynn, R.B., Baas, J.H., Hogg, A.J., Masson, D.G., Taylor, J.** and **Weaver, P.P.E.** (2002) Experimental constraints on shear mixing rates and processes: implications for the dilution of submarine debris flows. In: *Glacier-influenced Sedimentation on High-Latitude Continental Margins* (Eds Dowdeswell, J.A. and Ó Cofaigh, C.S.), *Geological Society of London Special Publication*, **203**, 89–103.
- Talling, P.J., Amy, L.A., Wynn, R.B., Peakall, J.** and **Robinson, M.** (2004) Beds comprising debrite sandwiched within co-genetic turbidite: origin and widespread occurrence in distal depositional environments. *Sedimentology*, **51**, 163–194.
- Talling, P.J., Wynn, R.B., Schmitt, D.N., Rixon, R., Sumner, E.** and **Amy, L.** (2010) How did thin submarine debris flows carry boulder-sized intraclasts for remarkable distances across low gradients to the far reaches of the Mississippi Fan? *J. Sed. Res.*, **80**, 829–851.
- Talling, P.J., Masson, D.G., Sumner, E.J.** and **Malgesini, G.** (2012) Subaqueous sediment density flows: depositional processes and deposit types. *Sedimentology*, **59**, 1937–2003.
- Taylor, K.G., Gawthorpe, R.L.** and **Van Wagoner, J.C.** (1995) Stratigraphic control on laterally persistent cementation, Book Cliffs, Utah. *J. Geol. Soc.*, **152**, 225–228.
- Tinterri, R.** (2011) Combined flow sedimentary structures and the genetic link between sigmoidal-and hummocky-cross stratification. *GeoActa*, **10**, 1–43.
- Veiga, G.D., Schwarz, E., Spalletti, L.A.** and **Massaferro, J.L.** (2013) Anatomy and sequence architecture of the early post-rift in the Neuquén Basin (Argentina): a response to physiography and relative sea-level changes. *J. Sed. Res.*, **83**, 746–765.
- Vergani, G.D., Tankard, A.J., Belotti, H.J.** and **Welsink, H.J.** (1995) Tectonic evolution and paleogeography of the Neuquén Basin, Argentina. In: *Petroleum Basins of South America* (Eds Tankard, A.J., Suárez, R. and Welsink, H.J.), *AAPG Memoir*, **62**, 383–402.
- Volkheimer, W., Rauhut, O.W.M., Quattrocchio, M.E.** and **Martínez, M.A.** (2008) Jurassic paleoclimates in Argentina, a review. *Rev. Asoc. Geol. Argentina*, **63**, 549–556.
- Weaver, C.** (1931) *Paleontology of the Jurassic and Cretaceous of West Central Argentina. Memoir University of Washington 1*, University of Washington, Seattle, 469 pp.
- Weaver, C.** (1942) A general summary of the Mesozoic of South and Central America. In: *8th American Science Congress (1940)* (Eds Oehser, P.H.), Department of States, Washington, DC, **4**, pp. 149–193.
- Yu, N.-T., Teng, L.S., Chen, W.-S., Yue, L.-F.** and **Chen, M.-M.** (2013) Early post-rift sequence stratigraphy of a Mid-Tertiary rift basin in Taiwan: insights into a siliciclastic fill-up wedge. *Sed. Geol.*, **286–287**, 39–57.
- Zachariah, A.-J., Gawthorpe, R., Dreyer, T.** and **Corfield, S.** (2009) Controls on early post-rift physiography and stratigraphy, lower to mid-Cretaceous, North Viking Graben, Norwegian North Sea. *Basin Res.*, **21**, 189–208.
- Ziegler, P.A.** and **Cloetingh, S.** (2004) Dynamic processes controlling evolution of rifted basins. *Earth-Sci. Rev.*, **64**, 1–50.

Manuscript received 29 October 2018; revision 15 January 2021; revision accepted 4 March 2021